

A NOVEL CANCER TREATMENT PLATFORM UTILIZING HER2-  
IMMUNOLIPOSOMES AND ULTRASOUND

by

Saniha Aysha Ajith

A Thesis Presented to the Faculty of the  
American University of Sharjah  
College of Engineering  
in Partial Fulfillment  
of the Requirements  
for the Degree of

Master of Science in  
Chemical Engineering

Sharjah, United Arab Emirates

May 2020

## **Declaration of Authorship**

I declare that this thesis is my own work and, to the best of my knowledge and belief, it does not contain material published or written by a third party, except where permission has been obtained and/or appropriately cited through full and accurate referencing.

Signature: Saniha Aysha Ajith

Date: May 15<sup>th</sup>, 2020

The Author controls copyright for this report.

Material should not be reused without the consent of the author. Due acknowledgement should be made where appropriate.

© 2020

Saniha Aysha Ajith

**ALL RIGHTS RESERVED**

## Approval Signatures

We, the undersigned, approve the Master's Thesis of

Title:

Date of Defense:

**Name, Title and Affiliation**

**Signature**

---

---

---

---

---

Dr. Lotfi Romdhane  
Associate Dean for Graduate Studies and Research  
College of Engineering

---

Dr. Sirin Tekinay  
Dean  
College of Engineering

---

Dr. Mohamed El-Tarhuni  
Vice Provost for Graduate Studies  
Office of Graduate Studies

## **Acknowledgements**

First and foremost, I would like to express my deepest gratitude to my thesis advisor, Dr. Ghaleb Husseini, for his continuous support and guidance throughout my thesis journey. His passion for research and positive outlook has motivated me to develop my research skills. Similarly, my heartfelt gratitude goes out to Mr. Vinod Paul and Ms. Nour Sawaftah, who helped me immensely throughout the whole thesis course. This research would not have been possible without their sincerest help, especially through the difficult times of the COVID-19 pandemic. Their assistance in acquiring experimental data and supporting me throughout the unforeseen lockdown circumstances is highly appreciated.

I would like to thank my good friend, Mr. Paul Kawak, for his continuous encouragement and patience to explain whenever I had a doubt. A huge thanks to all my friends and colleagues who constantly helped and supported me in completing my lab work. I am thankful to all the former and past members and researchers of the Ultrasound in Drug Delivery group for their efforts and continuous assistance.

In addition, I am thankful to my thesis committee examiner, Dr. Karnail Singh, and Dr. Nahid Awad whose valuable comments, feedback, and suggestions have helped me to improve my thesis.

I would like to extend my gratitude to the Chemical Engineering department at the American University of Sharjah, who gave me this opportunity to pursue my dreams. I am also thankful for the opportunity to have worked as a Graduate teaching assistant for two years in the department. More specifically, I am thankful to the head of the department, Dr. Sameer al-Asheh, for his constant support to all the graduate students throughout their study.

Lastly, my heartfelt gratitude to my parents and sister who supported me and continued to motivate me through all the ups and downs in my thesis and Masters journey.

## Abstract

Cancer is defined as the uncontrolled growth of cells in the body. It is one of the leading causes of death worldwide. One of the most common approaches to destroy cancer cells is via chemotherapy treatment, in which anti-cancer therapeutics are administered to the body. However, chemotherapy causes various adverse effects, including cardiotoxicity, nausea, anemia, and many more. To counteract these undesired effects, different smart drug delivery systems have been researched, in which nanocarriers can be used to exploit the enhanced permeability and retention (EPR) effect of cancerous tumors. Once the nanocarrier reaches the desired tumor site, external triggers can be applied to control the release of anti-neoplastic agents in that specific area. This study focuses on the use of liposomes conjugated with the monoclonal antibody, Trastuzumab, which is loaded with the chemotherapeutic drug, Doxorubicin, to target the overexpressed HER2 receptors on the surface of many breast cancer cells. Dynamic light scattering (DLS) was used to determine the liposome size, which was found to be  $94.9 \pm 1.29$  nm for the immunoliposomes and  $91.2 \pm 1.47$  nm for the NH<sub>2</sub>-terminated control liposomes. The concentration of lipids in the liposomes was determined using the Stewart Assay and the protein content using the BCA Assay. The external trigger used for the controlled release of the drug was low-frequency ultrasound. The release profiles of the control liposomes and immunoliposomes were studied at three different power densities, namely 7.46, 9.85, and 17.31 mW/cm<sup>2</sup>. Results showed that the immunoliposomes were slightly more sensitive to ultrasound and released a higher amount of drug in comparison to the control liposomes. Finally, drug release was modeled using nine kinetic models, namely: Zero-order, First-order, Higuchi, Hixon-Crowell, Korsmeyer-Peppas, Baker-Lonsdale, Weibull, Hopfenberg, and Gompertz. After linearizing the release data, the Baker-Lonsdale model provided the best fit. The future scope of this thesis involves using high-frequency ultrasound (HFUS) to release the drug, as well as *in vitro* and *in vivo* studies to determine the feasibility of using this drug delivery platform in hospitals and clinics around the globe.

**Keywords:** *Drug delivery, liposomes, ultrasound, trastuzumab, chemotherapy, Herceptin*

## Table of Contents

Abstract.....	5
Table of Contents.....	6
List of Figures.....	9
List of Tables.....	13
List of Abbreviations.....	14
Chapter 1. Introduction and Objectives.....	15
Chapter 2. Background and Literature Review.....	17
2.1 Introduction to Cancer.....	17
2.1.1 Cancer treatments.....	19
2.1.2 Chemotherapy and its limitations.....	19
2.1.3 Breast cancer and its receptors.....	20
2.2 Smart Drug Delivery Systems.....	22
2.2.1 Triggered targeting.....	22
2.2.2 Nanocarriers in cancer therapy.....	23
2.2.3 Passive targeting and the EPR effect.....	24
2.2.4 Active targeting.....	25
2.2.5 Monoclonal antibodies.....	25
2.3 Liposomes.....	28
2.3.1 Advantages and limitations of liposomal drug delivery.....	30
2.3.2 Methods of liposome preparation.....	30
2.3.3 Stealth liposomes.....	32
2.3.4 Immunoliposomes.....	32
2.3.5 Doxorubicin in liposomes.....	33
2.4 Ultrasound.....	34
2.4.1 Doppler effect.....	34
2.4.2 Generation of ultrasound.....	35
2.4.3 Characteristics of ultrasound.....	36
2.4.4 Ultrasound triggering in drug delivery.....	37
2.5 Previous Studies.....	38
Chapter 3. Materials and Methods.....	41
3.1 Materials.....	41

3.2 Preparation of Control and Targeted Liposomes .....	42
3.2.1 Synthesis of DSPE-PEG-NH2 control liposomes .....	42
3.2.2 Synthesis of trastuzumab conjugated immunoliposomes.....	42
3.3 Loading of DOX into DSPE-PEG2000- NH2 and Trastuzumab Conjugated Liposomes .....	44
3.4 Characterization of Liposomes.....	44
3.4.1 Determination of liposome size using Dynamic Light Scattering (DLS) ...	44
3.4.2 Lipid concentration quantification using Stewart’s assay .....	45
3.4.3 Confirmation of antibody conjugation using BCA assay .....	47
3.5 Low-Frequency Ultrasound Release Experiments.....	48
3.6 Mathematical Modeling of Drug Release .....	49
3.6.1 Zero-order model.....	50
3.6.2 First-order model .....	51
3.6.3 Higuchi model .....	51
3.6.4 Korsmeyer-Peppas model.....	51
3.6.5 Weibull model .....	52
3.6.6 Hixson-Crowell model .....	53
3.6.7 Baker-Lonsdale model.....	54
3.6.8 Hopfenberg model .....	55
3.6.9 Gompertz model .....	55
Chapter 4: Results and Discussion.....	57
4.1 Estimation of liposome size using Dynamic Light Scattering (DLS).....	57
4.2 Estimation of Lipid Concentration using Stewart’s Assay .....	58
4.3 Estimation of Protein Concentration using BCA Assay .....	59
4.4 Low-Frequency Ultrasound (LFUS) Release Studies.....	61
4.4.1 LFUS release results for control liposomes.....	61
4.4.2 LFUS release results for trastuzumab-conjugated immunoliposomes .....	64
4.4.3 Comparison in release profiles for control and immunoliposomes .....	65
4.5 Mechanical Index .....	71
4.6 Discussion and Further Insights .....	72
4.7 Kinetic Modeling.....	73
4.8 Statistical Analysis for Best Fit Model – Baker Lonsdale Model.....	80
Chapter 5. Conclusion and Future Work .....	83
References.....	85

Appendix.....	94
Appendix A: Release modeling plots for control liposomes (Batch 1) at a power density of 7.46 mW/cm <sup>2</sup> .....	94
Appendix B: Release modeling plots for control liposomes (Batch 1) at a power density of 9.85 mW/cm <sup>2</sup> .....	99
Appendix C: Release modeling plots for control liposomes (Batch 1) at a power density of 17.31 mW/cm <sup>2</sup> .....	104
Appendix D: Release modeling plots for immunoliposomes (Batch 1) at a power density of 9.85 mW/cm <sup>2</sup> .....	109
Appendix E: Release modeling plots for immunoliposomes (Batch 1) at a power density of 17.31 mW/cm <sup>2</sup> .....	114
Vita.....	119



## List of Figures

Figure 1: Transformation of a healthy cell into a cancer cell [4].....	17
Figure 2: Distribution of Breast Cancer subtypes in the US (2012-2016) [19].....	21
Figure 3: Stimuli used in Smart Drug Delivery Systems.....	23
Figure 4: Enhanced Permeability and Retention Effect at a tumor site [42] .....	25
Figure 5: Antibody Molecule Structure .....	26
Figure 6: Chemical structure of Trastuzumab [49].....	27
Figure 7: Mechanism of action for Herceptin [50] .....	28
Figure 8: Structure of liposome .....	29
Figure 9: Thin-film hydration technique.....	31
Figure 10: PEGylated liposome with encapsulated DOX [70].....	33
Figure 11: Expansion and contraction of piezoelectric crystals due to alternating current [76].....	35
Figure 12: High frequency and Low-Frequency Ultrasound Sine Wave [79].....	36
Figure 13: Difference between stable and transient cavitation .....	38
Figure 14: Conjugation of trastuzumab to liposome.....	43
Figure 15: Basic setup of DLS equipment.....	45
Figure 16: Calibration curve for Stewart Assay .....	58
Figure 17: Difference in lipid content for control liposomes and immunoliposomes ..	59
Figure 18: BCA calibration curve.....	60
Figure 19: Difference in protein concentration between control liposomes and immunoliposomes .....	61
Figure 20: Normalized release profiles for control liposomes at three different power densities.....	62
Figure 21: CFR vs. power density for 4 pulses and maximum release for control liposomes .....	63
Figure 22: Pulse wise fraction release for the first four pulses of control liposomes ..	63
Figure 23: Normalized release profiles for immunoliposomes at three different power densities.....	64
Figure 24: CFR vs. power density for 4 pulses and maximum release for immunoliposomes .....	65

Figure 25: Pulse wise fraction release for first four pulses for immunoliposomes .....	65
Figure 26: Comparison of normalized release profiles for control liposomes and immunoliposomes .....	66
Figure 27: Comparison of % drug release between control liposome and immunoliposomes at 1rst pulse.....	67
Figure 28: Comparison of % drug release between control liposome and immunoliposomes after the 2nd pulse .....	67
Figure 29: Comparison of % drug release between control liposome and immunoliposomes after the 3rd pulse .....	68
Figure 30: Comparison of % drug release between control liposome and immunoliposomes after the 4th pulse .....	68
Figure 31: Zero-order model (CFR vs time) for immunoliposomes at 7.46 mW/cm <sup>2</sup> (Batch 1).....	76
Figure 32: First order model (ln CFR vs time) for immunoliposomes at 7.46 mW/cm <sup>2</sup> (Batch 1).....	76
Figure 33: Higuchi model (CFR vs <i>t</i> ) for immunoliposomes at 7.46 mW/cm <sup>2</sup> (Batch 1) .....	77
Figure 34: Baker Lonsdale model (1.5[1-(1-CFR) <sup>23</sup> ]-CFR vs time) for immunoliposomes at 7.46 mW/cm <sup>2</sup> (Batch 1).....	77
Figure 35: Hixson Crowell model ((1-CFR) <sup>13</sup> vs time) for immunoliposomes at 7.46 mW/cm <sup>2</sup> (Batch 1) .....	78
Figure 36: Korsmeyer Peppas (log CFR vs log time) model for immunoliposomes at 7.46 mW/cm <sup>2</sup> (Batch 1) .....	78
Figure 37: Hopfenberg model (1-(1-CFR) <sup>13</sup> vs time) for immunoliposomes at 7.46 mW/cm <sup>2</sup> (Batch 1) .....	79
Figure 38: Weibull model (log[-ln(1-CFR)] vs time) for immunoliposomes at 7.46 mW/cm <sup>2</sup> (Batch 1) .....	79
Figure 39: Gompertz model (ln[-ln(CFR)] vs time) for immunoliposomes at 7.46 mW/cm <sup>2</sup> (Batch 1) .....	80
Figure 40: Zero-order model for control liposomes at 7.46 mW/cm <sup>2</sup> .....	94
Figure 41: First-order model for control liposomes at 7.46 mW/cm <sup>2</sup> .....	94
Figure 42: Korsmeyer- Peppas model for control liposomes at 7.46 mW/cm <sup>2</sup> .....	95

Figure 43: Hopfenberg model for control liposomes at 7.46 mW/cm <sup>2</sup> .....	95
Figure 44: Higuchi model for control liposomes at 7.46 mW/cm <sup>2</sup> .....	96
Figure 45: Weibull model for control liposomes at 7.46 mW/cm <sup>2</sup> .....	96
Figure 46: Baker Lonsdale model for control liposomes at 7.46 mW/cm <sup>2</sup> .....	97
Figure 47: Gompertz model for control liposomes at 7.46 mW/cm <sup>2</sup> .....	97
Figure 48: Hixson-Crowell model for control liposomes at 7.46 mW/cm <sup>2</sup> .....	98
Figure 49: Zero order model for control liposomes at 9.85 mW/cm <sup>2</sup> .....	99
Figure 50: First order model for control liposomes at 9.85 mW/cm <sup>2</sup> .....	99
Figure 51: Korsmeyer Peppas model for control liposomes at 9.85 mW/cm <sup>2</sup> .....	100
Figure 52: Hopfenberg model for control liposomes at 9.85 mW/cm <sup>2</sup> .....	100
Figure 53: Higuchi model for control liposomes at 9.85 mW/cm <sup>2</sup> .....	101
Figure 54: Weinull model for control liposomes at 9.85 mW/cm <sup>2</sup> .....	101
Figure 55: Baker Lonsdale model for control liposomes at 9.85 mW/cm <sup>2</sup> .....	102
Figure 56: Gompertz model for control liposomes at 9.85 mW/cm <sup>2</sup> .....	102
Figure 57: Hixson - Crowell model for control liposomes at 9.85 mW/cm <sup>2</sup> .....	103
Figure 58: Zero - order model for control liposomes at 17.31 mW/cm <sup>2</sup> .....	104
Figure 59: First oder model for control liposomes at 17.31 mW/cm <sup>2</sup> .....	104
Figure 60: Korsmeyer - Peppas model for control liposomes at 17.31 mW/cm <sup>2</sup> .....	105
Figure 61: Hopfenberg model for control liposomes at 17.31 mW/cm <sup>2</sup> .....	105
Figure 62: Higuchi model for control liposomes at 17.31 mW/cm <sup>2</sup> .....	106
Figure 63: Weibull model for control liposomes at 17.31 mW/cm <sup>2</sup> .....	106
Figure 64: Baker-Lonsdale model for control liposomes at 17.31 mW/cm <sup>2</sup> .....	107
Figure 65: Gompertz model for control liposomes at 17.31 mW/cm <sup>2</sup> .....	107
Figure 66: Hixson-Crowell model for control liposomes at 17.31 mW/cm <sup>2</sup> .....	108
Figure 67: Zero order model for immunoliposomes at 9.85 mW/cm <sup>2</sup> .....	109
Figure 68: First order model for immunoliposomes at 9.85 mW/cm <sup>2</sup> .....	109
Figure 69: Korsmeyer-Peppas model for immunoliposomes at 9.85 mW/cm <sup>2</sup> .....	110
Figure 70: Hopfenberg model for immunoliposomes at 9.85 mW/cm <sup>2</sup> .....	110
Figure 71: Higuchi model for immunoliposomes at 9.85 mW/cm <sup>2</sup> .....	111
Figure 72: Weibull model for immunoliposomes at 9.85 mW/cm <sup>2</sup> .....	111
Figure 73: Baker-Lonsdale model for immunoliposomes at 9.85 mW/cm <sup>2</sup> .....	112
Figure 74: Gompertz model for immunoliposomes at 9.85 mW/cm <sup>2</sup> .....	112

Figure 75: Hixson-Crowell model for immunoliposomes at 9.85 mW/cm <sup>2</sup> .....	113
Figure 76: Zero order model for immunoliposomes at 17.31 mW/cm <sup>2</sup> .....	114
Figure 77: First order model for immunoliposomes at 17.31 mW/cm <sup>2</sup> .....	114
Figure 78: Korsmeyer - Peppas model for immunoliposomes at 17.31 mW/cm <sup>2</sup> .....	115
Figure 79: Hopfenberg model for immunoliposomes at 17.31 mW/cm <sup>2</sup> .....	115
Figure 80: Higuchi model for immunoliposomes at 17.31 mW/cm <sup>2</sup> .....	116
Figure 81: Weibull model for immunoliposomes at 17.31 mW/cm <sup>2</sup> .....	116
Figure 82: Baker-Lonsdale model for immunoliposomes at 17.31 mW/cm <sup>2</sup> .....	117
Figure 83: Gompertz model for immunoliposomes at 17.31 mW/cm <sup>2</sup> .....	117
Figure 84: Hixson-Crowell model for immunoliposomes at 17.31 mW/cm <sup>2</sup> .....	118

## List of Tables

Table 1: Properties of main components for the synthesis of liposomes.....	41
Table 2: Sample preparation for Stewart Assay .....	46
Table 3: Sample preparation for BCA Assay .....	48
Table 4: Release values for Korsmeyer Peppas Model [101].....	52
Table 5: DLS results for the size of liposomes .....	57
Table 6: Lipid concentration results from Stewart Assay.....	58
Table 7: Protein concentration results using BCA Assay .....	60
Table 8: Heat map of p-test: Comparison between control liposomes and immunoliposomes after the first pulse .....	69
Table 9: Heat map of p-test: Comparison between control liposomes and immunoliposomes after the second pulse .....	70
Table 10: Heat map of p-test: Comparison between control liposomes and immunoliposomes at the third pulse .....	70
Table 11: Heat map of p-test: Comparison between control liposomes and immunoliposomes at the fourth pulse .....	71
Table 12: R <sup>2</sup> values for control liposomes .....	74
Table 13: R <sup>2</sup> values for immunoliposomes .....	75
Table 14: Release constants for Baker Lonsdale model for control liposomes and immunoliposomes at three different power densities .....	81
Table 15: Two factor ANOVA test for release constants .....	82

## **List of Abbreviations**

**ANOVA** - Analysis of Variance

**BCA** - Bicinchoninic Acid Assay

**DDS** - Drug Delivery System

**DLS** - Dynamic Light Scattering

**DOX** - Doxorubicin

**DPCC** - Dipalmitoylphosphatidylcholine

**EPR** - Enhanced Permeability and Retention Effect

**ER** - Estrogen receptor

**FDA** - Food and Drug Administration

**HER** - Herceptin

**HER2** - Human Epidermal Growth factor receptor 2

**HFUS** - High-Frequency Ultrasound

**LFUS** - Low-Frequency Ultrasound

**mAb** - Monoclonal Antibody

**MI** - Mechanical Index

**NP** - Nanoparticles

**PBS** - Phosphate Buffer Saline

**PEG** - Poly-ethylene Glycol

**PR** - Progesterone receptor

**RES** - Reticuloendothelial System

**SDDS** - Smart Drug Delivery System

**US** - Ultrasound

## Chapter 1. Introduction and Objectives

Cancer is defined as the uncontrolled growth of cells in the body. Approximately 1.8 million cancer cases were diagnosed in the United States alone in 2019 [1]. According to the World Health Organization's (WHO) International Agency for Research on Cancer (IARC), there were 4,707 new cases of cancer diagnosed in the UAE in 2018, and the highest incidence was recorded for breast cancer with 1,054 new breast cancer diagnoses [2]. A variety of treatment options exist to treat the disease. Chemotherapy is one of the most common treatment options in which anticancer drugs are administered into the bloodstream of the patient to destroy cancer cells. However, this mode of treatment causes severe side effects, including cardiotoxicity, anemia, nausea, hair loss, and damage to the oral and intestinal linings in the patient because of the systemic nature of this therapy. To mitigate these side effects, researchers are constantly researching new methods to control the spatial and temporal delivery of the chemotherapeutics, so that these cytotoxic chemicals only affect diseased tissues. A variety of novel drug delivery methods exist, which include stem cell transplants, hyperthermia, photodynamic therapy, and smart drug delivery systems (SDDS). SDDSs have the capability to deliver the therapeutic drug to the specific affected area and release its contents in response to an external trigger. In this study, immunoliposomes are chosen as the nanocarriers to encapsulate the chemotherapeutic drug doxorubicin. Trastuzumab (Herceptin®) ligands will be conjugated to the surface of the liposomes to actively target the overexpressed HER2 receptors on the surface of breast cancer cells.

This thesis is organized as follows. Chapter 1 gives a brief introduction about the study with an emphasis on current cancer statistics along with the experimental objectives. Chapter 2 provides a detailed literature review and background about cancer, liposomes, smart drug delivery systems, ultrasound and related studies. It further discusses concepts including receptor-mediated endocytosis, the enhanced permeability and retention effect, monoclonal antibodies, and the different uses of trastuzumab. Chapter 3 discusses the materials used in the experiments, the synthesis of the immunoliposomes, and the protocols followed pertaining to DLS, the Stewart Assay, the BCA Assay, and low-frequency ultrasound drug release. Additionally, nine different mathematical models used in drug delivery are explored in-depth, and their

advantages and shortcomings summarized. Chapter 4 presents and discusses the experimental results obtained and their findings are compared with literature studies. Lastly, Chapter 5 gives a brief conclusion, outlines future experiments, and recommends a way to optimize this immune-drug delivery project.

The objectives of this thesis are itemized below:

1. To synthesize control liposomes and trastuzumab-conjugated stealth liposomes encapsulating the chemotherapy drug doxorubicin.
2. To use dynamic light scattering (DLS) to calculate the mean size of the liposomes.
3. To determine/quantify the lipid concentration of both types of liposomes using the Stewart assay.
4. To verify the antibody conjugation and and quantify the protein content using BCA assay.
5. To study drug release using low-frequency ultrasound (at 20-kHz) ultrasound at three different power densities exhibited by both control liposomes and immunoliposomes.
6. To model drug release using different kinetic models and to determine which model provides the best fit for the release data.



## Chapter 2. Background and Literature Review

### 2.1 Introduction to Cancer

Cancer is a disease in which abnormal cells in the body grow uncontrollably. Healthy cells have the ability to repair if their DNA gets damaged. ‘Apoptosis’ is the programmed cell death of old cells and is characterized by biochemical mechanisms. It is considered necessary for various cell processes like the development, functioning of the immune system, embryonic development, and chemically-induced cell death [3]. However, cancer cells ignore these signals, hence stopping apoptosis and initiating the development of malignancies. Figure 1 shows how a healthy cell undergoes damage to its DNA to form a mutated cell, which eventually leads to the formation of cancerous cells [4]. Cancer cells also have the ability to prompt nearby healthy cells to form blood vessels that would supply the tumor with oxygen and other nutrients, as well as remove waste products from these fast-growing diseased cells[5]. The most commonly occurring types of cancers are those of the breast, lung, prostate, and colon. It is worth mentioning that cancer mortality rates are higher among men compared to women [6].

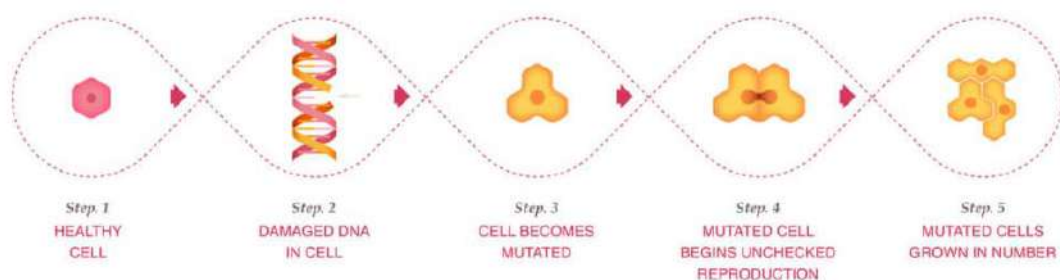


Figure 1: Transformation of a healthy cell into a cancer cell [4]

Cancer is a disease that could be inherited or may be caused by the DNA damage due to environmental factors, such as UV rays, tobacco smoke, radiation, etc. [7]. Other examples of known carcinogens include asbestos, arsenic, benzene, beryllium, formaldehyde, and vinyl chloride. Three types of carcinogens exist depending on how the chemical is metabolized inside the body. ‘Direct acting carcinogens’ are those which can directly cause cancer. ‘Procarcinogens’ are those which can give rise to

cancerous cells only if they change structure after metabolism. Finally, ‘cocarcinogens’ act with other chemicals to induce the growth of cancer cells in the body [8].

The main genetic drivers of cancer are proto-oncogenes, tumor suppressor genes, and DNA repair genes. Proto-oncogenes are the driving force for healthy cell growth and division. If these genes are altered or changed, they may give rise to oncogenes –genes that allow cells to grow and survive infinitely. Proto-oncogenes are activated in cancer cells to give rise to new characteristics such as hyperactive division and growth, the ability to become recognized in new tissues, or protection against apoptosis [7]. Tumor suppressor genes are involved in controlling the rate at which a cell grows and divides. Alterations in this type of gene will allow the formation of cancer cells. Cells with altered DNA repair genes will cause other mutations to develop, which can, in turn, lead to new cells becoming cancerous [4]. One of the commonly researched tumor suppressor genes is p53 due to its common occurrence in human cancer cells. Recent studies show that the p53 protein is actively involved in DNA synthesis, gene transcription, DNA repair, genomic plasticity, and programmed cell death [9].

Cancers can be categorized according to their cell type. Carcinomas are the most common kind of cancers which are formed by epithelial cells. Cancers that originate in the bone and soft tissues like muscle, fat, blood vessels, and lymph vessels are known as sarcomas. Leukemias are cancers which generate from the tissue responsible for forming blood cells present in the bone marrow. Any cancer which begins in the lymphatic system is a lymphoma [4]. Cancer cells can grow and travel away from the place they originated to other vital organs – a phenomenon known as ‘metastases’. This is the most common cause of death for patients with malign neoplasm [7]. Almost every type of cancer has the ability to metastasize. This process takes place when cancer cells gain access to the blood vessels and move to other parts where they proliferate in order to build new tumors. The beginning of the metastasis process includes activation of the epithelial-mesenchymal transition (EMT), which refers to the activation of the latent embryonic program by cancer cells [7].

**2.1.1 Cancer treatments.** There are many modalities to treat cancer. The method of treatment strongly depends on the type and stage of the tumor. Most people will undergo a combination of two or more treatments for the most effective destruction of the cancerous tumor. The most common types of treatments are surgery, chemotherapy, radiation therapy, and immunotherapy.

Surgery is one of the principal methods to get rid of a cancerous tumor in the body. It can either be applied to get rid of an entire tumor or ‘debulk’ a tumor. Modern methods of surgery include cryosurgery, lasers, hyperthermia, and photodynamic therapy. Chemotherapy is a method in which drugs are administered to the body to kill cancer cells. It is either used to stop or slow the growth of the diseased cells. In radiation therapy, high doses of radiation are utilized to kill cancer cells and shrink tumors. This is due to the fact that extremely high doses of radiation can cause permanent damage to the DNA of cancer cells. Two main types of radiation therapy are currently used to treat cancer– external beam and internal beam. External beam therapy is a localized treatment as it targets only the specific part of the body. In contrast, in internal beam therapy, a solid or liquid radiation emitting source is placed inside the body. In immunotherapy treatment, the immune system of the patient is employed to fight against the disease. It is a branch of biological therapy that uses living organisms to kill cancer cells. Cancerous cells have the ability to avoid the immune system, and hence, they continue to grow uncontrollably. In immunotherapy, cancer cells are made to be identified by the immune system so that they can attack the cells [10].

**2.1.2 Chemotherapy and its limitations.** Chemotherapy is the administration of drugs into the body to eliminate or slow down the growth of the tumor. In the 20th century, Paul Ehrlich discovered the term ‘chemotherapy’ during his search for a chemical that could potentially cure syphilis. The first successful drug for cancer was Heidelberger’s 5-fluorouracil (5-FU).<sup>3</sup> Phenylalanine mustard, designed for melanoma [11]. Since all healthy cells undergo cell multiplication, non - targeted chemotherapeutic drugs can affect healthy cells, especially cells of the bone marrow, and mucous membranes. In many cases, anti-neoplastic agents are often combined to maximize the chances of success of this treatment option[12].

Chemotherapy causes major side effects because it does not discriminate between healthy and diseased cells. The majority of the prescribed anti-cancer chemotherapeutic drugs, for the treatment of breast cancer, are anti-microtubule agents. These agents have proven toxicities of peripheral neuropathy and myelosuppression. Other side effects commonly caused by similar anti-cancer drugs are nausea, anemia, mucositis, and diarrhea. Chemotherapy enhances poor specificity and causes dose-limiting toxicities of cancer drugs at the tumor tissue. Research shows that cardiotoxicity is closely associated with certain antineoplastic agents used to treat cancer. According to the National Cancer Institute, cardiotoxicity is the ‘toxicity that affects the heart, since it causes dilated cardiomyopathy, rhythmic disturbances, and myocardial infarction [13]. In addition, chemotherapeutic drugs may also cause abnormal immune function [7].

**2.1.3 Breast cancer and its receptors.** Breast cancer is the most prevalent cancer in women, and it is also the second most common cancer among men and women. In 2018, over 2 million new cases of breast cancer were diagnosed globally [14]. The incidence of breast cancer increases with age, with over 80% of diagnoses occurring in women over the age of 50. Risk factors include late menopause, early menarche, obesity, lack of exercise, and alcohol consumption. Research shows that patients with BRCA-1/BRCA-2 genetic mutations have a 40 – 85% lifetime risk of developing breast cancer [15]. According to the American Joint Commission on Cancer, the stages of breast cancer can be categorized by the assessment of three principal factors: lymph node status, tumor size, and evidence of metastases. The evidence of metastasis is associated with weaker outcomes/prognosis for the patient. According to the classification by the World Health Organization, at least 15 different types of tumors related to breast cancer have been recognized based on their histological appearance. The majority of the tumors come under the classification of ‘invasive ductal carcinoma’ [16].

Molecular markers exist for the detection of the early onset of breast cancer. These include estrogen receptors (ER), progesterone receptors (PR), and human epidermal growth factor receptor 2 (HER2). However, only tumors that portray ER expression are more likely to benefit from anti-estrogenic therapy. The general method for assessment of PR and ER is immunohistochemistry (IHC) [16]. The overexpression of HER2

receptors has been confirmed in many human cancer cells such as breast, head, neck, gastric, ovarian, pancreatic, endometrial, bladder, and non-small cell lung cancer [17]. 20 to 25% of all diagnosed breast cancers overexpress the human epidermal growth factor receptor 2 (HER2). This particular receptor indicates that cancer is very aggressive and has a poor prognosis. However, tumors that do overexpress the HER2 receptors are very responsive to certain chemotherapeutic agents, as well as to targeted therapy. Trastuzumab was the first anti-HER2 monoclonal antibody [18]. Four principle molecular subtypes for breast cancer receptors have been classified as shown below. The distribution of the subtypes of breast cancer is portrayed in Figure 2. Hormone receptor-positive (HR+) cancers are those that test positive for ER or PR, or both [19].

- Luminal A (HR+/HER2-): This is the most common kind and is generally known to be the least aggressive.
- Luminal B (HR+/HER2+): This type is known for portraying highly positive levels of the protein Ki67, which indicates a large number of dividing cells.
- Basal-like (HR-/HER2-): Also known as ‘triple-negative’ due to being ER-negative, PR-negative, and HER2-negative.
- HER2-enriched (HR-/HER2+): In earlier times, this subtype was associated with the worst outcomes. However, with the development of targeted therapies, prognosis has drastically improved for patients with HER2+ cancers [19].

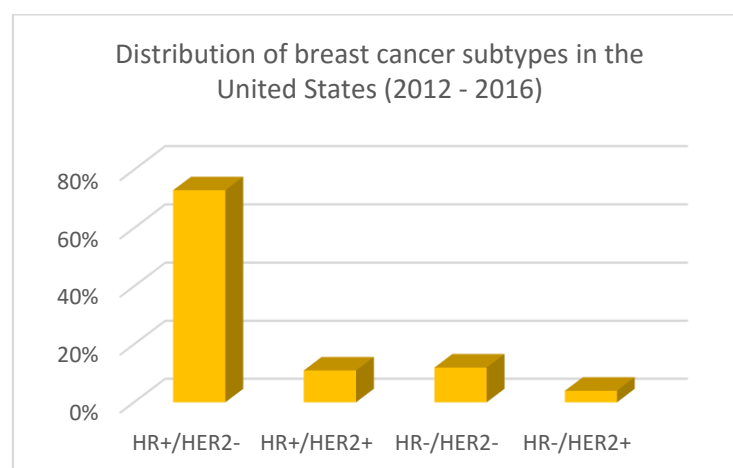


Figure 2: Distribution of Breast Cancer subtypes in the US (2012-2016) [19]

## 2.2 Smart Drug Delivery Systems

A drug delivery system (DDS) is a term that encompasses approaches, formulations, technologies, and devices used in the transportation of a pharmaceutical product needed by the body in order to safely achieve the desired therapeutic effect [20]. Various anatomical pathways can be utilized to deliver the drug to the diseased location. These include oral, transmucosal, topical, or inhalation. Recent research in drug delivery developed the mechanism of targeted delivery and controlled release of drugs. In order for such a system to be efficient, the DDS has to escape the host defense mechanisms and circulate to the designated site. Examples of such formulations include biodegradable microspheres, liposomes, micelles, dendrimers, microbubbles, and drug-polymer conjugates [20]. In recent years, conventional DDSs have evolved into smart DDS with stimuli-responsive characteristics. These nanocarrier DDS can respond to specific internal or external triggers and thus, increase the drug targeting efficiency while reducing side effects and toxicities [21]. The design of an effective nanocarrier depends on two properties: First, the ability of the drug to reach the desired tissue, and second, the interaction of the drug with the target tissue only and not with healthy cells. In order to achieve this, three strategies are used: Active, passive, and triggered targeting.

**2.2.1 Triggered targeting.** Frequently used stimuli in smart drug delivery systems are changes in pH, redox potential, enzyme activity, temperature, light, ultrasound, magnetism, and radiation [22], as shown in Figure 3. Temperature is an internal trigger and can be used when the temperature of the cancer cells varies with the temperature of the healthy cells, causing the formation of a gradient to release the contents. Thermosensitive nanocarriers have the ability to release the contents when the temperature is increased above body temperature, at around 40 °C to 45 °C [21]. Similarly, a pH gradient also exists between cancerous cells and healthy cells in the body, allowing pH triggering to release contents from a nanocarrier onto the tumor site [23]. Light irradiation has been extensively used in drug delivery fields for years. Certain light-sensitive carriers can release the drugs upon exposure to light, which can cause certain phenomena like photoisomerization, photocleavage, or photo dimerization to occur [24]. Ultrasound is also an external trigger used in drug delivery

systems. Using ultrasound can induce effects such as cavitation to release a drug. The process of cavitation is thoroughly explained in Section 2.4.4 of this thesis. Redox responsive carriers are highly sensitive to high levels of glutathione in the cells and rapidly release the cargo at the tumor site. In addition, redox responsive systems are known to improve drug concentration [25]. In magnetic drug targeting, an external magnetic field is applied to manipulate the magnetic drug carriers in the body. Two main fields of magnetic responsive systems exist static field and varying field magnets. This mode of targeting has been extensively used in treating ailments such as cancer, nervous system problems, sensorineural hearing loss, etc. [26].

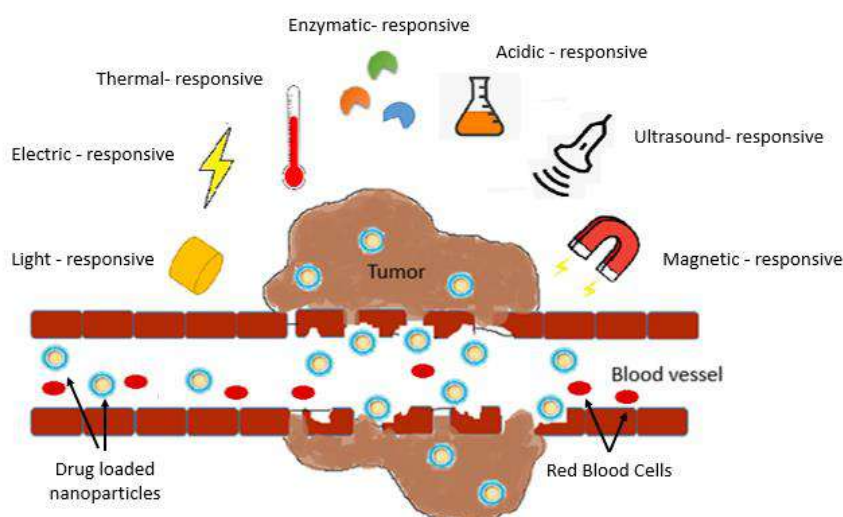


Figure 3: Stimuli used in Smart Drug Delivery Systems

**2.2.2 Nanocarriers in cancer therapy.** Recent advances in medicine witnessed the emergence of a new field that utilizes nanoparticles in cancer detection, diagnosis, and treatment. ‘Nano’ is a term derived from the Greek word ‘nanos’ which means small. These nanoparticles are usually in size ranges of 1 to 100 nm ( $10^{-9}$ m). Because of their uniquely small size, nanoparticles can interact with biomolecules on the surface, as well as the interior of the cells in order to revolutionize cancer diagnosis and treatment [27]. Nanocarriers can be differentiated based on three different categories: material/composition, shape, and medical application [20]. Furthermore, they are usually of two types: organic and inorganic. Organic nanocarriers include liposomes, micelles, dendrimers, glutamic acid derivatives, organogels, and synthetic organic

nanosystems. These are associated with high biocompatibility and biodegradation rates, but low drug loading capacity and low chemo/thermal stability. Inorganic nanocarriers such as  $\text{Fe}_3\text{O}_4$ , gold, silica, and carbonaceous nanoparticles possess high stabilities and multifunctionalities but poor biocompatibility. Certain properties that render nanoparticles useful in drug delivery are their negligible renal filtration, high surface-to-volume ratios, and the ability of the modification using various functional groups. Nanocarriers have the ability to deliver chemotherapeutic agents to tumor sites, as well as image-specific tumors in cancer patients [27]. Multifunctional nanocarriers have the ability to combine radiotherapy and chemotherapy, in addition to accelerating the diagnostic process [1]. The most frequently used nanoparticles for such treatment include micelles [28][29], quantum dots [30], carbon nanotubes [31], gold nanoparticles [32], silver nanoparticles [33], polymeric nanoparticles [34], liposomes [35][36], and more recently metal organic frameworks [37][38].

**2.2.3 Passive targeting and the EPR effect.** Passive targeting is the mechanism by which tumor cells allow the deposition of drugs in tumor tissues. The physiology of tumors enables molecules in the size range of 12.5 nm and 150 nm to reach the tumor site via a phenomenon known as enhanced permeability and retention (EPR) [20]. The EPR effect was first reported by Matsumura and Maeda in 1986. Their study showed that the majority of the tumors have defective blood vessels and thus exhibit enhanced vascular permeability [39]. One of the limitations of the active and passive delivery is the fact that these DDS are susceptible to opsonization and subsequent undesired reticuloendothelial system (RES) uptake, which results in lowered drug accumulation at the tumor site. To counteract this effect, the surface of these DDS is usually coated with polyethylene glycol (PEG) to improve the *in vivo* circulation time, and hence substantially reducing protein adsorption and opsonization. This further increases the accumulation of the encapsulated drug within tumor tissues. PEG is ideal for stealth purposes since it is water-soluble, biocompatible, and has low immunogenicity. This phenomenon, along with poor lymphatic drainage at the site of the tumor, results in the previously-mentioned EPR effect [40]. There are certain factors that affect the EPR, such as vascular endothelial growth factor, nitric oxide, bradykinin, and prostaglandins [41]. The EPR has become an essential factor in the design of anticancer treatment techniques, including gene delivery, molecular imaging, antibody therapy, liposomes,



and micelles [21]. Figure 4 illustrates the EPR effect at a tumor site [42]. In Figure 4, nanocarriers (represented by the black carriers) are loaded with the drug and delivered into the bloodstream. However, at the tumor site, these blood vessels become more damaged and are prone to increased entry by the nanocarriers directly to the tumor site. Using this technique, the drug will be delivered only to the cancerous cells, thus avoiding other healthy cells in the body.

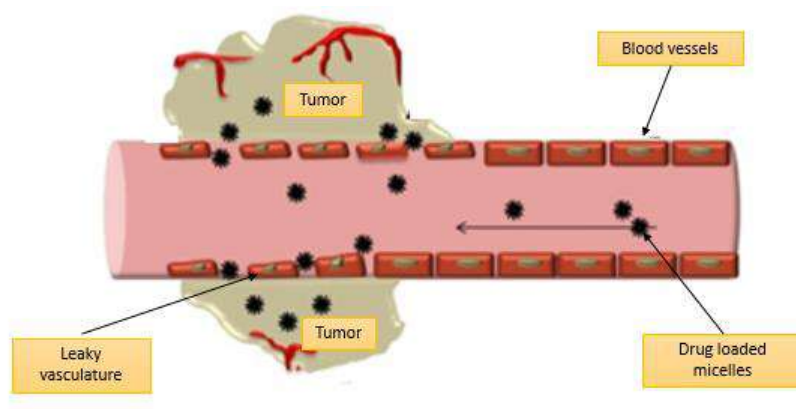


Figure 4: Enhanced Permeability and Retention Effect at a tumor site [42]

**2.2.4 Active targeting.** Active targeting utilizes specialized molecules and ligands such as peptides, antibodies, or small molecule that gives it the ability to bind to specific receptors on the cell surface. Principles of conjugation chemistry are used to link the nanocarriers to the surface of the liposomes. Such nanocarriers can recognize and bind to the targeted cells via ligand-receptor interaction. In order to achieve efficient drug delivery, the tumor cells must highly express (over-express) the specific receptors on their surface. Examples of receptors expressed on the surface of most cancerous tumors include EGFRs (Epidermal Growth Factor Receptors) [22], RGD receptors [43], transferrin receptors [44], folate receptors [45], and estrogen receptors [46]. In addition, to ensure efficient targeting, the most appropriate system must be chosen with the appropriate targeting molecules.

**2.2.5 Monoclonal antibodies.** Antibodies are protein molecules produced by plasma cells. They usually have a large Y-shape and carry out two essential functions. The first function is to recognize and bind antigens, while the second function is to get

rid of unnecessary antigens. Their structure is globular and hence are sometimes referred to as immunoglobulins [47]. Antibodies are usually released by the B-cell receptor. They consist of 2 heavy chains, and 2 light chains stabilized using disulfide bridges. Figure 5 shows the structure of an immunoglobulin antibody molecule.

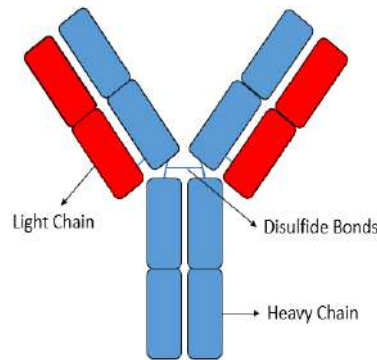


Figure 5: Antibody Molecule Structure

A monoclonal antibody (mAb) is formed from identical immune cells that are clones of a unique parent cell. They have the capability to selectively bind to an antigen. Monoclonal antibodies are effective in diagnostic techniques and novel therapies due to the fact they are homogenous and specific to antigens. Their potential application for clinical use was introduced by Kohler and Milstein in 1975. In recent times, monoclonal antibodies have been developed with variations in size and configurations using recombinant engineering techniques. This has paved the way for human monoclonal antibodies with high antigen specificity and a longer circulating half-life. Due to these characteristics, monoclonal antibodies have the potential to be used in delivering drugs to cancerous tumors or sites on inflammation. Specific diseases in which monoclonal antibodies have been used with success include rheumatoid arthritis, Crohn disease, graft-versus-host disease, chronic asthma, myocardial infarction, and lymphoma [48]. The clinical monoclonal antibodies can be recognized using the suffix in its name. For example, murine antibodies end with –omab, mouse-human antibodies with –ximab, humanized antibodies with –zumab, and human antibodies with –umab [47].

**2.2.5.1 Trastuzumab.** Trastuzumab is a monoclonal antibody (mAb) used in the treatment of breast cancer patients who overexpress the HER2 receptors. It is the first humanized mAb against HER2 receptors approved by the FDA in 1998 for breast

cancer patients [17]. When using this monoclonal antibody, along with chemotherapy, the recurrence is reduced by 50%, and the survival rate is prolonged by 30% [15]. However, the use of trastuzumab comes with certain limitations, the principle being cardiac failure. In addition, the use of trastuzumab with anthracyclines should be avoided. Some studies have reported 16-27% of cardiac dysfunction when Trastuzumab and anthracyclines were administered together [48]. In recent times, two other novel drugs that have demonstrated efficacy following Trastuzumab failure have been developed. These are ‘lapatinib’, an oral tyrosine kinase inhibitor, and ‘bevacizumab’, an anti-angiogenic drug [15]. An efficient strategy for the delivery of chemotherapeutic drug molecules to HER2-overexpressed cells could be the targeting of the extracellular domain of these receptors using Trastuzumab mAb. The Trastuzumab would then inhibit its dimerization after binding to the extracellular domain [17]. Trastuzumab is available in the pharmaceutical industry under the brand name Herceptin®. It is sterile, white to yellow in color, and is administered intravenously. Figure 6 shows the molecular structure of Trastuzumab [49].

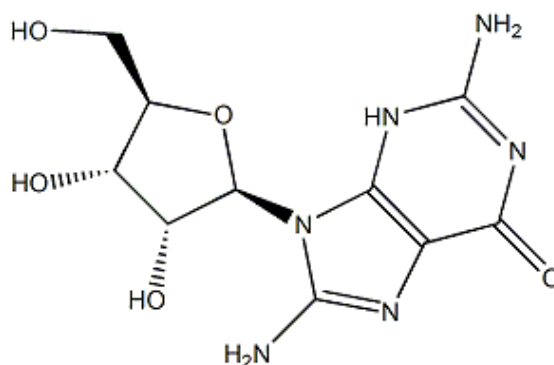


Figure 6: Chemical structure of Trastuzumab [49]

Figure 7 displays the proposed mechanism of action of Trastuzumab. HER2 receptors are transmembrane receptors that are present on both normal cells as well as HER2+ tumor cells. However, they are usually overexpressed in great numbers on certain type of breast cancer cells. This overexpression poses a great advantage for the Trastuzumab or Herceptin molecule to directly conjugate itself to the tumor site. Trastuzumab plays a significant role in the signaling network as well as blocking intracellular signaling pathways. It is capable of inducing apoptosis and blocking cell proliferation by attenuating the transduction signal. It also tags the cancer cells for

antibody-dependent cellular cytotoxicity (ADCC), which leads to their destruction by the immune system [50].

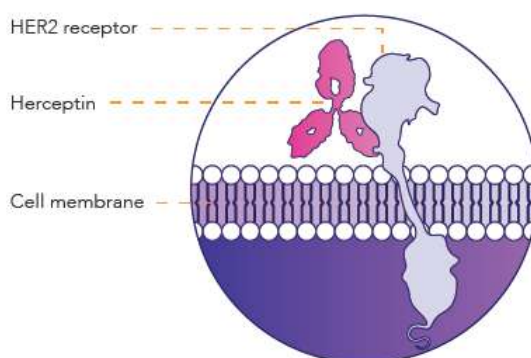


Figure 7: Mechanism of action for Herceptin [50]

### 2.3 Liposomes

Liposomal technology is a recent and dynamic approach to enhance drug delivery to tumors [51]. Liposomes were first discovered by Dr. Bingham, a British hematologist, in the year 1960. It was an accidental discovery when he added water to the phosphatidylcholine molecule and discovered that the molecule formed a closed bilayer structure with an aqueous phase surrounded by a lipid bilayer [52]. Liposomes are biodegradable and nontoxic vesicles that can be used to encapsulate hydrophilic and hydrophobic materials. Moreover, they have the ability to carry radioactive moieties like radiotracers, making them an ideal tool for molecular imaging applications [51].

Liposomes are defined as spherical vesicles containing a single or several continuous lipid bilayers which separate the external aqueous medium from the aqueous core. This unique structure gives liposomes the ability to carry numerous agents such as drugs, small interference RNA, plasmid DNA, peptides, proteins, organelles, viruses, and bacteria. The loaded molecules can either be hydrophobic, hydrophilic, or amphipathic. The physiochemical characteristics of the molecule play a role in deciding the exact position of the molecule within the liposome – being either in the membrane, on inside liposome aqueous phase [53]. In terms of size, liposomes can be classified as small unilamellar, medium unilamellar, large unilamellar, giant unilamellar, and multivesicular. On the basis of application, they can be categorized as fusogenic, pH-

sensitive, cationic, long circulatory, and immune liposomes [52]. Figure 8 shows the structure of a liposome [54].

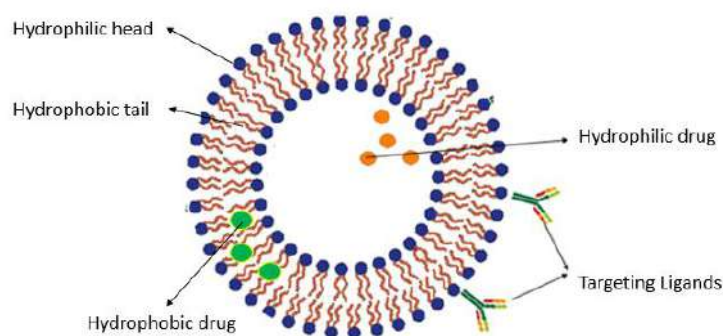


Figure 8: Structure of liposome

Lipids are usually classified as hydrophobic or hydrophilic. The latter nature of certain lipids causes them to develop into organized structures such as vesicles when immersed in an aqueous medium. Lipids can be formulated from plant- or animal-derived tissues using low-polarity solvents, e.g., chloroform. Phospholipids can be classified as natural or synthetic. Natural phospholipids are obtained from sources like soya bean or egg yolk. In general, phosphatidylcholine and phosphatidylethanolamine are the commonly used natural phosphatides to produce liposomes [55]. An important property of liposomes is the ‘phase transition temperature’ of the lipids that constitute its structure. The phase transition temperature is the temperature required to change the physical state of a lipid from an ordered gel phase to a disordered liquid phase. This, in turn, changes the hydrocarbon chains, which are fully extended and closely packed to chains (chains are usually randomly oriented). Several factors affect the transition temperature of a liposome, including the hydrocarbon length, unsaturation, charge, and head group [56].

The efficiency of the delivery of drugs to tumors via liposomes is affected by various factors related to the liposomal formulation, as well as tumor characteristics. In addition, a smaller vesicle size enhances the passage of liposome into the reticuloendothelial system (RES). Moreover, certain properties of the tumor, including blood flow, vascular permeability, and interstitial pressure, play a key role in effective liposomal drug delivery [57]. A total of 15 liposome-based drugs are currently used

clinically, and more are under development [53]. The first FDA approved liposomal formulation as a nano-drug delivery system is Doxil– liposomal Doxorubicin. The liposomes encapsulating Doxil are composed of a high phase transition temperature phospholipid, cholesterol, and MPEG-DSPE [58].

**2.3.1 Advantages and limitations of liposomal drug delivery.** The main benefit of using liposomes is that they can encapsulate both hydrophilic and hydrophobic therapeutics. The hydrophilic molecules are carried in the aqueous interior, while the hydrophobic drugs remain in the membrane. In addition, they are also able to maintain their structure at physiological temperatures. The size of liposomes can be controlled to be small enough to enter tumor sites, and large enough to avoid renal excretion. They can also be used for active targeting by binding molecules with site-specific ligands. In order to increase circulation time and avoid opsonization, their surfaces can be modified. Due to the composition of phospholipid and their similarity to cell membranes, liposomes are biodegradable and biocompatible [59]. Liposomes also reduce the toxicity of the encapsulated drug and increase the therapeutic index of the drug.

However, certain limitations also exist in the use of liposomal drug delivery systems. They are known to be less soluble in blood and have shorter half-lives. The phospholipid has an inclination to undergo hydrolysis and oxidation reactions. There is also a tendency for the drug to leak from these nano vehicles. The cost of production of drug encapsulated liposomes is usually very high.

**2.3.2 Methods of liposome preparation.** The key constituents to synthesize a liposome include cholesterol, phosphatidylcholine, and certain electrically charged lipids. The phospholipid itself can be modified to suit the need of the liposome. If a hydrocarbon chain has more than 14 carbon atoms and is saturated (no double bonds), it gives rise to rigid gel-like lipid membrane at physiological temperatures. These liposomes are less prone to drug leakage [60].

The synthesis of a liposome generally follows four steps:

1. Dissolving lipids in an organic solvent and evaporating the solvent via rotary evaporation
2. Dispersing the lipid in an aqueous media.

3. Controlling the size and composition of the liposome for its intended purpose.
4. Analyzing the vesicles in the final liposomal solution [61].

A variety of methods have been reported in the literature to prepare liposomes. The most commonly used methods include thin-film hydration, reverse-phase evaporation, solvent-injection techniques, and detergent dialysis. Additionally, techniques such as sonication, high- pressure extrusion, and microfluidization have been introduced to shear and reduce the size of the vesicles [62].

In the thin-film hydration technique, the liposomes are obtained by dissolving the lipid in an organic solvent such as chloroform. To obtain a dried thin film, vacuum is applied while the lipid solution is rotating in a rotary evaporator. This is followed by the hydration of the film using an aqueous solution containing the drug. Further sonication and extrusion can be done to reduce and shear the size of liposomes. This technique is portrayed in Figure 9. In the reverse-phase evaporation method, the lipid is initially dissolved in an organic solvent. The resulting solution is then mixed with an aqueous solution containing the drug at freezing temperatures in a sonication bath. This leads to the formation of a water-oil emulsion. Following this, the organic solvent is discarded under low pressure, eventually forming a viscous gel. Applying vigorous agitation to this gel causes the formation of large liposomes. In the ethanol injection technique, the phospholipids are dissolved in ethanol and then injected into an aqueous environment while stirring. The drug is then dissolved in an inorganic solution or a buffer solution. Once stirring is complete, the ethanol is removed by a rotary evaporator under vacuum. In the dehydration technique, the lipids are dissolved in an organic solvent and then evaporated to form a lipid film. This is then hydrated with the drug solution and freeze-dried with sodium chloride to maintain the osmolarity [63].

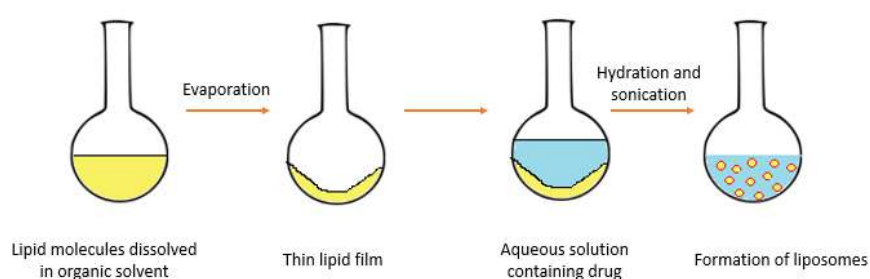


Figure 9: Thin-film hydration technique

**2.3.3 Stealth liposomes.** Sterically stabilized ‘stealth’ liposomes are those obtained by incorporating a synthetic polyethylene glycol on the surface of their phospholipid. The benefit is to enhance the circulation time and improve drug accumulation in tumor sites. However, if stealth liposomes circulate for longer periods of time, it could lead to slower drug release, which could potentially affect the efficiency of the treatment [64]. A single hydroxyl group exists on the methoxy form of PEG and can be conjugated with drug molecules, lipids, polymers, and proteins. A dense barrier of hydrophilic PEG chains is formed on the surface of the liposome to create the stealth effect and hide it from the reticuloendothelial system. Pegylation also leads to an increase in liposomal size, hence reducing the chance of its clearance from the system. However, some studies have reported that PEGylated liposomes could potentially activate the complement system and lead to pseudo-allergic reactions [65]. Recent studies show that PEGylated stealth liposomes get covered with a protein corona when exposed to blood in the body. Several assumptions have been made that such liposomes may develop their stealth properties due to specific blood proteins binding to the PEG chains and therefore hiding the nanocarrier from the host immune system [66]. Certain studies have shown that PEG hinders the conjugation of antibodies to the liposome. In order to maintain steric stabilization and antibody recognition, it is sufficient to use polyethylene glycol – 200 as compared to shorter or longer PEG chain lengths [67].

**2.3.4 Immunoliposomes.** An immunoliposome is defined as a liposome with antibody or antibody fragments non-covalently conjugated to its surface. These nanovehicles were first introduced in the 1980s. There are two main techniques to prepare immunoliposomes. The first involves the conjugation of the antibodies to the liposome, while in the second technique, dialysis is used to incorporate the antibody conjugates to the liposome. The first method is more widely used and results in antibodies being attached exclusively to the outside of the liposome [67].

Most of the immunoliposome preparation techniques involve conjugating the antibodies to the distal ends of a PEG chain in a PEGylated liposome. In this case, the methoxy group at the end of the PEG chain is replaced with other groups to allow antibody conjugation. In order to achieve this, covalent and non-covalent approaches are employed. Covalent conjugation can be used when the antibody contains functional



groups like amines and carboxylates. Additionally, the sulfhydryl group plays a significant role as a targeting group. Thiolated antibodies that contain sulfhydryl groups react with antibodies to form a thioether linkage [47]. A potential problem of immunoliposome preparation is immunogenicity. If a liposome causes an immune reaction, it could potentially decrease its half-life in the body [67].

**2.3.5 Doxorubicin in liposomes.** Doxorubicin is an anthracycline antibiotic facilitated by the inhibition of DNA, RNA, and protein synthesis between the adjacent pairs of the DNA. When doxorubicin is encapsulated within liposomes by making use of pegylation, it is known as pegylated liposomal doxorubicin (trade name Doxil®) [68]. It was the first approved nano-drug by the FDA in 1995 [69].

The formulation of Doxil® is based on three principles:

1. The use of PEGylated liposomes to avoid the reticuloendothelial system and to prolong the circulation time in the body.
2. Loading of the doxorubicin using a transmembrane ammonium sulfate gradient, which also aids in the release of the drug at the specified tumor site.
3. Lipid bilayer consisting of ‘liquid-ordered’ phase composed of phosphatidylcholine and cholesterol [69].

Figure 10 shows a schematic of the PEGylated liposomal structure. Doxorubicin (DOX) is loaded within the liposome and protected by methoxypolyethylene glycol [70].

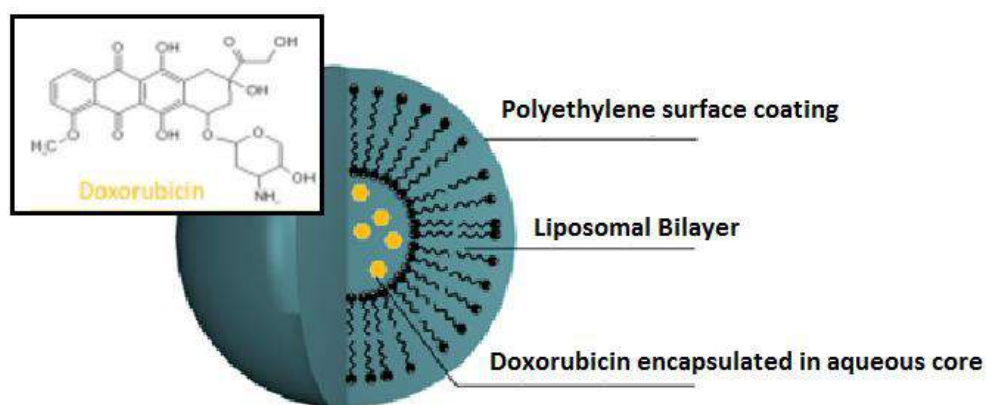


Figure 10: PEGylated liposome with encapsulated DOX [70]

Studies have shown that doxorubicin can be ionized at low pH. The release of the drug from the liposomes goes through three main stages: The dissolution of the solid drug crystal, the protonation or deprotonation of the soluble doxorubicin, and the passive transport of neutral doxorubicin across the lipid bilayer. Doxil liposomes are around 100 nm in diameter and are known to encapsulate approximately 10,000–15,000 doxorubicin molecules [71].

This liposomal doxorubicin is associated with lesser instances of cardiomyopathy, neutropenia, and alopecia. In addition, it has an improved pharmacokinetic profile and allows for over 1 hour of intravenous delivery. Studies have also shown that the usage of pegylated liposomal doxorubicin greatly inhibits tumor growth and increases the chances of survival in comparison to conventional (free) doxorubicin [68].

## **2.4 Ultrasound**

Ultrasonic waves are sound waves with frequencies above 20 kHz and are transmitted above the human hearing level. They are mechanical waves and require a physical medium in order to be transmitted. They are classified into four different categories: longitudinal/compressional waves, transverse/shear waves, surface/Rayleigh waves, and plate/Lamb waves based on the mode of particle vibration in the medium [72]. Presently, ultrasonic waves have various uses. Low-frequency ultrasound (US) (20-100 kHz) is usually used when chemical and physical changes are desired, e.g., cavitation. In contrast, ultrasound in the range of 1 to 10 MHz is mostly used for animal navigation and communication, detection of cracks in solids, diagnostic purpose, and underwater echolocation. US is widely used in medicine and can be categorized as either low- or high-intensity for different therapeutic purposes. Low-intensity US can be used for imaging and flow studies, while high-intensity US is utilized in kidney stone shattering and tumor ablation [53].

**2.4.1 Doppler effect.** The Doppler Effect is defined as changes in the frequency of transmitted waves when relative motion exists between the source of the wave and the observer. The frequency and distance between the source and observer are directly proportional [53]. In the late 1950s, medical applications of the Doppler effect were

initiated. A research team made the first pulse wave Doppler device in Seattle in 1966. It is currently used extensively to analyze blood flow and tissue motion [73]. If the source and observer are in motion in the same line, the observer in motion will receive a wave whose apparent frequency is given by [74]:

$$f_{os} = f \frac{v - v_o}{v - v_s} \quad (1)$$

where  $f$  = the actual frequency of the wave emitted by the source through the medium

$v$  = the velocity of the wave propagating through the medium at rest

$v_o$  = the velocity of the observer with respect to the medium

$v_s$  = the velocity of the source with respect to the medium

Currently, three different types of Doppler US exist in the medical field:

- Color Doppler – a computer converts Doppler measurements into an array of colors. It gives an indication of the speed and blood flow direction in vessels.
- Power Doppler- This is more sensitive than color Doppler and is capable of providing greater detail of blood flow. It is used in areas where the blood flow is minimal
- Spectral Doppler – This displays blood flow measurements graphically. It is also used to convert blood flow information into a distinctive sound [75].

**2.4.2 Generation of ultrasound.** US waves are generated by applying an alternating current to piezoelectric crystals in a transducer. These crystals will undergo alternating expansions and contractions to create mechanical longitudinal waves as shown in Figure 11 [76].

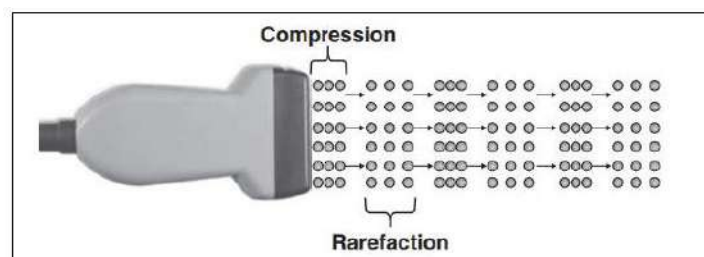


Figure 11: Expansion and contraction of piezoelectric crystals due to alternating current [76]

Another method to generate low-frequency US is the Galton's whistle. A moveable reflector and its position can be varied using a screw at one end of the pipe. This causes a change in the length of the air column in the pipe and causes a change in the pitch of the note. Adjusting the distance of air and pressure of the air blast, the pipe can be set into resonant vibration at a particular frequency corresponding to its length and diameter [77].

Finally, in the magnetostriction method, a magnetic field is applied along the axis of a ferromagnetic material like iron, cobalt, and nickel in the form of a box. This causes the length of the bar to change. The change is negligible in the case of a direct field. However, the field becomes oscillating when the effect is more pronounced since the elastic forces can no longer resist the change. The general range of a magnetostriction ultrasonic oscillator is from 5,000 c/s to 60,000 c/s [77].

**2.4.3 Characteristics of ultrasound.** The compression and rarefaction of the molecules can be graphically represented as a sine wave, as shown in Figure 12 . Wavelength is defined as the distance between one peak of the wave and the next wave. It is an important parameter in diagnostic US as it determines the imaging resolution of the equipment [78].

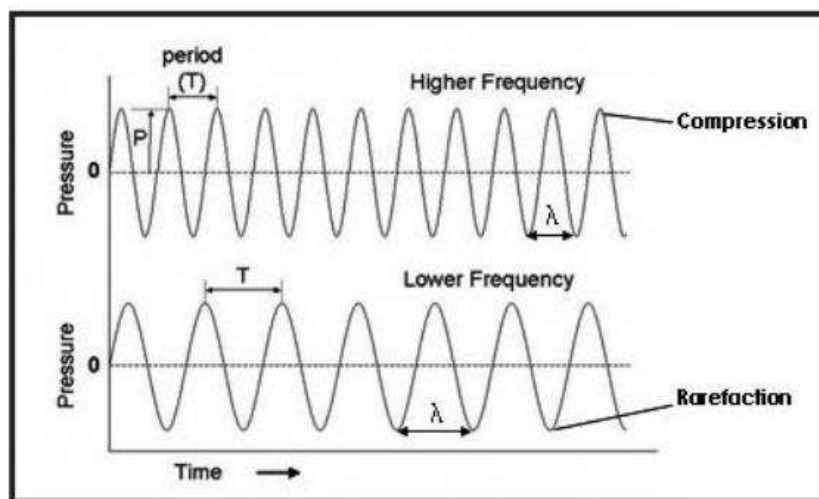


Figure 12: High frequency and Low-Frequency Ultrasound Sine Wave [79]

Within a phase, the rate of propagation of sound waves is a function of elasticity, and is known as sound wave velocity. Another important property in medical

applications is the acoustic impedance, defined as the product of tissue density with the velocity in the tissue. As ultrasonic waves travel from one medium to another, some energy gets reflected while the rest travels to the second medium. This amount of reflected energy can be determined by calculating the difference in acoustic impedance in the two media [78].

Attenuation is used to describe the loss of energy once an ultrasonic wave propagates through a tissue. This phenomenon can be divided into absorption, which involves energy transfer from the mechanical to the heat forms, and scattering, which involves the dispersion of energy from its main direction of propagation. Power density, also known as US intensity, is the power per cross-sectional area measured in  $\text{W}/\text{cm}^2$  [78].

A cycle is defined as the complete path traveled by a wave. Frequency is the number of cycles completed in one second, and has the units of Hertz (Hz). The amplitude of the wave is defined as the maximum excursion either in the positive or negative direction from the baseline [44]. If two sinusoidal waves with different frequencies are superimposed, their amplitudes can be added and subtracted to make the overall wave an amplitude of the sum of the individual waves, and frequency is the difference between the individual frequencies [53].

**2.4.4 Ultrasound triggering in drug delivery.** In the past, therapeutic ultrasound was mainly used for its thermal or mechanical effects. However, novel technology of using non-thermal ultrasound in conjunction with drugs has broadened the outlook of therapeutic ultrasound. This non-thermal phenomenon includes cavitation, acoustic streaming, microjets, and radiation forces. Drug delivery systems for cancer therapy have developed tumor site-specific drugs that are employed nowadays [80]. Various triggers have been identified and studied for drug release purposes such as pH [81], temperature [82], light, and enzymes [83]. Ultrasound can induce mechanical or thermal effects to drug delivery carriers, which are designed to respond to such an increase in temperature or mechanical effects [53].

In the case of liposomes loaded with therapeutic drugs used for drug delivery, a gas bubble gets formed in the hydrophobic region of the lipid bilayer of a liposome when exposed to an oscillating ultrasonic wave. This gas nucleus will continue to grow

in size until they permeate through the membrane to form a transient pore to act as a gateway for drug release. Once the acoustic field is turned off, the membrane reseals and goes back to its initial state. These formed transient pores can either be hydrophilic or hydrophobic in nature. This principle is known as cavitation [53].

The cavitation process consists of three distinct steps: nucleation or formation, rapid growth or expansions during cycles, and the violent collapse in the medium [84]. Two different cavitation phenomena exist in liquid bubbles: stable and transient as shown in Figure 13. In stable cavitation, the bubble wall, along with the acoustic field, oscillates for several cycles. This happens only at lower acoustic intensities since the size of the bubble oscillates in phase with the expansion and compression cycles. Since only a very small variation in bubble size exists, the significance of the chemical effect is small. In contrast, transient cavitation occurs at high acoustic intensities. This will cause the bubble to become unstable and collapse during the compression phase of the acoustic wave. In this mechanism, the size of the bubble increases exponentially from tens to hundreds of times the equilibrium radius before it collapses violently. Stable cavitation can lead to transient cavitation; alternatively, transient cavitation could produce very small bubbles that may undergo stable cavitation [72].

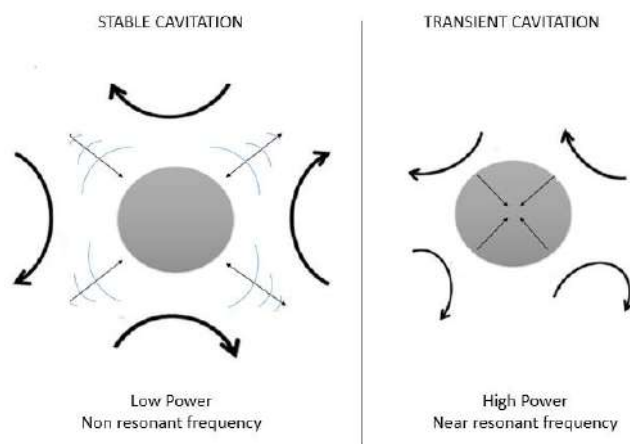


Figure 13: Difference between stable and transient cavitation

## 2.5 Previous Studies

A few *in vitro* as well as *in vivo* studies have been carried out to investigate the delivery of doxorubicin encapsulated Trastuzumab conjugated immunoliposomes to

cancer cells. A study was conducted to understand the safety profile and efficiency of a combination of liposome-encapsulated doxorubicin, trastuzumab, and paclitaxel as a novel drug combination. The study included thirty patients with breast cancer overexpressing various receptors. The neoadjuvant treatment was delivered to all patients, and results showed that the combination was well tolerated by all. There was no incidence of heart failure in any of them except one who developed 10% asymptomatic reduction in the left ventricular fraction. The study concluded that the treatment could be potentially effective as a therapeutic option for patients with HER2-positive breast cancer [18].

Shin et al. conducted an *in vitro* study where gemcitabine (GCT)-encapsulated immunoliposomes with conjugated Herceptin were produced to determine its therapeutic effect in SK-BR-3 breast cancer cells. Experiments showed that the final liposome (HerPEG-TSL-GCT) had the capability to deliver the drug to a hyperthermic environment. The encapsulation efficiency was calculated and found to be  $54.6 \pm 3.5$ . Additionally, around 19 antibody molecules were attached to a single liposome. Results of *in vitro* experiments showed an increased cytotoxicity using HerPEG-TSL-GCT compared to conventional liposomes, which further improved the delivery of the drug to breast cancer cells [85].

Another study by Colbern et al. investigated the difference in therapeutic effect between the free chemotherapy drug Cisplatin and PEGylated-liposomal cisplatin (PL) with a combination of Herceptin. Results showed that PL-cisplatin was more efficient to non-liposomal cisplatin as an antitumor agent at tolerable levels. When Herceptin was conjugated to both delivery routes, both PL-cisplatin and free cisplatin were statistically similar in their antitumor activity. The conclusion formed was that combining Herceptin along with PL-cisplatin has an excellent potential to decrease agent's toxicity in patients who are diagnosed with metastatic breast cancer [86].

Amin et al. lead an *in vitro* research study where the aim was to target the breast cancer cell line, SK-BR-3 using idarubicin loaded immunoliposomes. These liposomes were prepared and loaded with the chemotherapeutic drug, idarubicin, using analytical methods. The initial HER2 overexpression in the breast cancer cell line was confirmed using western blotting. The cell lines were then treated using varying concentrations of

free idarubicin, idarubicin loaded liposome, and idarubicin loaded trastuzumab conjugated liposomes. The viability of the cells was analyzed using the MTT assay. Results showed that loading idarubicin in trastuzumab-conjugated immunoliposomes improved the efficiency of the agent. Additionally, idarubicin-encapsulated immunoliposomes were found to be more potent in the ablation of HER2 overexpressing cells [17].

The Drug Delivery lab at the American University of Sharjah has successfully synthesized targeted liposomes using estrone [87][88], albumin [89], transferrin [90], and linear RGD [91] as moieties. Ultrasound was then used to release the contents of these carriers upon demand. This is the first report of using immunoliposomes encapsulating an active chemotherapy drug and releasing its contents using acoustic waves.



## Chapter 3. Materials and Methods

### 3.1 Materials

The chemicals and materials used in this study are dipalmitoylphosphatidyl choline (DPPC) and 1,2-distearoyl-sn-glycero-3-phosphoethanolamine-N-[amino(polyethylene glycol)-2000] (DSPE-PEG2000-NH<sub>2</sub>) which were obtained from Avanti Polar Lipids Inc. (Alabaster, AL, USA). 2,4,6 trichloro-1,3,5 triazine (cyanuric chloride – ((NCCl)<sub>3</sub>) and doxorubicin (DOX) were obtained from Sigma-Aldrich (St.Louis, MO, USA). Chloroform was purchased from Panreac Quimica S.A. (Spain) and cholesterol from AlfaAesar (Ward Hill, MA, USA). The bicinchoninic acid (BCA) kit was obtained from Sigma50 Aldrich Chemie GmbH (Munich, Germany). Sephacryl S200 HR was purchased from Sigma-Aldrich (Sweden). Sephadex® G-25, Phosphate buffered saline (PBS) tablets, Ammonium sulfate, and Triton X-100 were acquired from LABC0, which is the official Sigma-Aldrich distributor in the United Arab Emirates. Trastuzumab (Herceptin®) was obtained from a local pharmacy. HEPES (4-(2-hydroxyethyl)-1-piperazineethanesulfonic acid)) solution was prepared using sucrose, L-ascorbic acid, and HEPES sodium salt (purchased from LABC0). Additionally, ammonium ferrocyanate was prepared using ammonium thiocyanate and Iron (III) chloride hexahydrate (FeCl<sub>3</sub>.6H<sub>2</sub>O) (Uni-Chem from Beograd, Serbia, and VWR International Ltd., USA). The properties of the main chemicals are listed in Table 1.

Table 1: Properties of main components for the synthesis of liposomes

Material	Molecular Weight (g/mol)	Molecular Formula
DPPC	734.039 [92]	C <sub>40</sub> H <sub>80</sub> NO <sub>8</sub> P [92]
DSPE-PEG (2000)-NH <sub>2</sub>	2790.521 [93]	C <sub>132</sub> H <sub>266</sub> N <sub>3</sub> O <sub>54</sub> P [93]
Cholesterol	386.7 [94]	C <sub>27</sub> H <sub>46</sub> O [94]
Doxorubicin	543.5 [95]	C <sub>27</sub> H <sub>29</sub> NO <sub>11</sub> [95]
Trastuzumab	298.255 [49]	C <sub>10</sub> H <sub>14</sub> N <sub>6</sub> O <sub>5</sub> [49]

## 3.2 Preparation of Control and Targeted Liposomes

**3.2.1 Synthesis of DSPE-PEG-NH<sub>2</sub> control liposomes.** Liposomes were prepared using the lipid film hydration technique. 5.6 mg, 4.7 mg, and 19.2 mg of DSPE-PEG2000-NH<sub>2</sub>, cholesterol, and DPPC, respectively, were dissolved in 4 ml of an organic solvent (chloroform) in a 250 mL round bottom flask. A bigger round bottom flask helps in the formation of a thinner and more uniform lipid film. The chloroform was then evaporated in a rotary evaporator in the presence of vacuum at 50 °C for 15 minutes. At the end of this step, the formation of a thin lipid layer in the interior of the flask is observed. It is important to make sure that no traces of chloroform is present since this can adversely affect the stability of liposomes in addition to the known toxicity of the solvent in *in vitro* and *in vivo* applications. This step is followed by the addition of the hydration solution to the film. The hydration solution is prepared by thoroughly dissolving 29 mg of ammonium sulfate in 2 mL of distilled water. This ensures the presence of a pH gradient for the encapsulation of DOX in the liposomes. After the addition of this solution, the round bottom flask is left to rotate in the rotary evaporator at 60 °C without vacuum for 50 minutes. This is followed by the sonication of the solution in a 40-kHz sonication water bath (Elma D-78224, Melrose Park, IL, USA) at half-wave output at 60 °C for 2 minutes. This step is essential in order to ‘shear’ the liposomes and to reduce the multilamellar vesicles to unilamellar. The liposomes were then extruded at 60 °C using an Avanti® Mini-extruder from Avanti Polar Lipids, Inc. using a 0.2 µm Whatman polycarbonate filter for 31 times. The liposomal solution was then purified by passing it through a Sephadex G-25 column, which was previously soaked in a PBS solution for 2 hours. The supernatant, which contains concentrated liposomes, was then collected and stored at 4 °C until further use.

**3.2.2 Synthesis of trastuzumab conjugated immunoliposomes.** In order to conjugate the Trastuzumab to control (-NH<sub>2</sub>-terminated) liposomes, two steps were followed: First, the liposome needs to be modified with cyanuric chloride, and second, the monoclonal antibody should be added at a pH of 8.5 as shown in Figure 14.

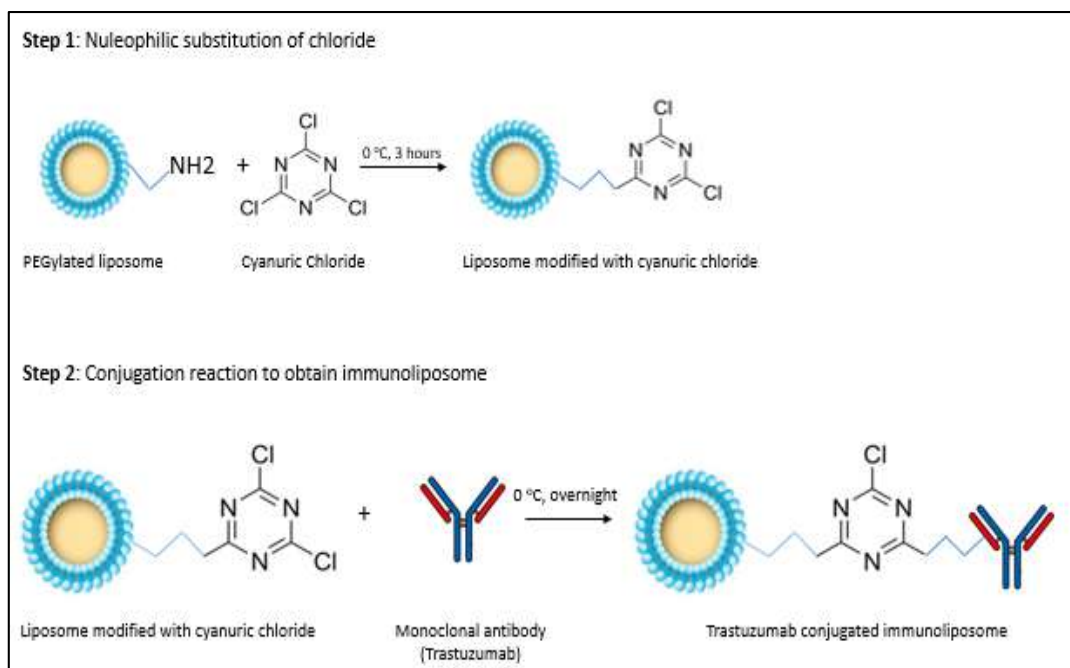


Figure 14: Conjugation of trastuzumab to liposome

Liposomes were synthesized as described in Section 3.2.1. It is necessary to carry out the above reactions at 0 °C in order to maintain stability. First, 10 mg of cyanuric chloride was dissolved in 1 mL of acetone to prepare a 10 mg/ml solution. 9.3  $\mu\text{L}$  of the- above-prepared solution was then diluted in 0.5 mL deionized water. In order to attain a 1:1 molar ratio of cyanuric chloride to DSPE-PEG-NH<sub>2</sub>, 1 mL of liposomes was added to the diluted acetone-cyanuric chloride mixture in a vial. The vial was then placed in an ice bath and stirred at 80 rpm for 3 hours. This allows for the nucleophilic substitution of chloride (in the cyanuric chloride) with the proton of the NH<sub>2</sub> group present on the surface of the liposomes. At the end of 3 hours, a solution of 1 mg Trastuzumab in 0.5 mL borate buffer at pH 8.5 was prepared and added to the liposomes. The solution was again placed in an ice bath and kept stirring at 80 rpm overnight to reach completion. In order to purify the liposomes, a Sephacryl S-200 HR triple column was prepared by equilibrating with PBS solution. The liposomal solution was passed through this column in order to collect any excess Trastuzumab. The collected liposomes were stored at 4 °C until use.

### **3.3 Loading of DOX into DSPE-PEG2000- NH<sub>2</sub> and Trastuzumab Conjugated Liposomes**

For loading the drug DOX into the liposome, the method of trans-membrane ammonium ion gradient was used. A base exchange of the weak amphipathic base of DOX with the ammonium ions took place. Using this loading method, more than 90% of the DOX got encapsulated. By means of various analysis techniques such as the X-ray diffraction, the study found that almost all of the encapsulated DOX is present in the intra-liposome aqueous phase in the form of crystalline DOX salt [69].

For loading DOX into the liposomes, the first step was to prepare the DOX solution by dissolving 16 mg DOX in 1 mL of HEPES solution. 250  $\mu$ L of the DOX solution was then added into the liposomal solution to obtain a drug-to-lipid ratio of 1:25 (w/w) and incubated in a water bath at 60 °C . The solution was gently stirred at 80 rpm for 45 minutes. It is important to cover all the samples with aluminum foil to prevent the photodegradation of DOX. A single gel filtration column was prepared using 1.5 g of Sephadex G-25 equilibrated with 10 mL of borate buffered saline. The liposomal solution was then passed through this column for the purification and removal of free DOX in the solution.

### **3.4 Characterization of Liposomes**

**3.4.1 Determination of liposome size using Dynamic Light Scattering (DLS).** The mean size of the liposomes was determined by Dynamic Light Scattering (DLS) using the DynaPro® NanoStar™ equipment by Wyatt Technology Corp, Santa Barbara, CA, USA. Dynamic light scattering is a well-researched and noninvasive technique used to measure the size and distribution of molecules and particles. It works on the principle of Brownian motion, which states that particles are constantly in random motion and cause collisions. These collisions induce energy transfer, which further starts particle movements. The smaller particles will begin to move at relatively higher speeds than the larger particles. Measuring the speed of the particles, the hydrodynamic diameter can be confirmed. The Stokes-Einstein equation is used to find the relationship between the speed and size of particles. Since temperature and viscosity affect the particle movement, those terms are included Equation 2.

$$D = \frac{k_B T}{6\pi\eta R_H} \quad (2)$$

where  $D$  = translational diffusion coefficient (speed of particles)

$k_B$  = Boltzmann constant ( $\text{m}^2\text{kg}/\text{K s}^2$ )

$T$  = temperature (K)

$\eta$  = viscosity (Pa.s)

$R_H$  = Hydrodynamic radius (m)

Figure 15 shows the basic setup of a DLS machine. A laser beam is directed towards the sample placed in a cuvette. Once the light hits the particles, it gets scattered in every direction. The angle with which the light gets scattered is converted into a signal; the latter is used to calculate the diffusion coefficient. A gray filter is usually placed between the laser and cuvette to attenuate the beam in cases of turbulent mixtures, where the photons will not be detected by the detector [96]. The hydrodynamic radii of the liposomes were determined at room temperature after the liposome samples were properly diluted in phosphate buffered saline (PBS). A test sample was prepared by diluting 15  $\mu\text{L}$  of liposome in 1 mL of PBS solution. The sample was then transferred to a cuvette before readings were recorded.

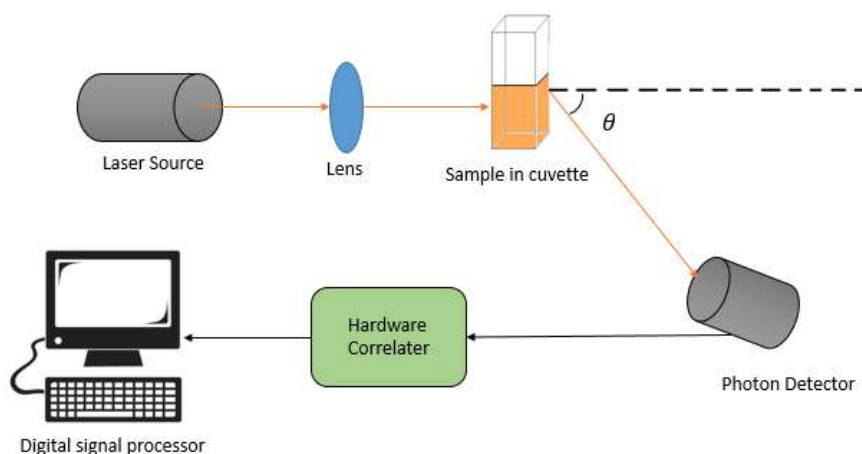


Figure 15: Basic setup of DLS equipment

**3.4.2 Lipid concentration quantification using Stewart's assay.** A method to quantify the phospholipids present is using the Stewart Assay, which was first reported in the Journal of Analytical Biochemistry by J.C.M Stewart in 1980. The assay utilizes

the ability of phospholipids to react with ammonium ferrothiocyanate (FTC) to form a complex. The primary advantage of using this assay over others is that the presence of inorganic phosphate does not interfere with the assay [97]. The first step in this assay is to prepare a calibration curve by dissolving DPPC in chloroform at varying concentrations and measuring the absorbance at 485 nm. One hundred  $\mu\text{L}$  of liposomes are then transferred into a 250 mL round bottom flask and evaporated under vacuum using a rotary evaporator for 15 minutes. This is then followed by the addition of 2 mL of chloroform and sonication in a water bath at a half-wave output for 10 minutes. This step is essential to ensure the lipid film is dissolved and no residue remains. Using ammonium ferrothiocyanate, chloroform, and the liposomes, samples are prepared according to the quantities shown in Table 2. Sample tubes 1, 1A, 2, 2A, 3, and 3A contain the control liposomes, while tubes 4, 4A, 5, 5A, 6, and 6A contain the trastuzumab conjugated immunoliposomes. It is necessary to prepare two blank samples without any liposomes to record the initial baseline.

Table 2: Sample preparation for Stewart Assay

Labeled Sample Tubes		Liposome + Chloroform ( $\mu\text{L}$ )	Chloroform ( $\mu\text{L}$ )	FTC ( $\mu\text{L}$ )
1	4	75	1925	2000
1A	4A	75	1925	2000
2	5	125	1875	2000
2A	5A	125	1875	2000
3	6	200	1800	2000
3A	6A	200	1800	2000
Blank 1		-	2000	2000
Blank 2		-	2000	2000

The samples are then vigorously mixed in a vortexer and centrifuged at 1000 rpm for 10 minutes each. After giving the samples a few minutes to settle, it is observed that a biphasic system was formed. Ammonium ferrothiocyanate (FTC) reacts and forms a complex with DPPC; however, it is immiscible in chloroform. Therefore, the top red layer in the tube contains FTC, which is discarded using a pipette, while the clear bottom layer consists of the DPPC-chloroform complex. In order to analyze the quantity of phospholipids, the bottom DPPC-chloroform mixture is transferred into a quartz cuvette. The absorbance for each sample is measured at 485 nm using the Evolution™ 60S UV-Visible Spectrophotometer (ThermoFisher Scientific, Madison, WI, USA) and the software VISIONlite.

**3.4.3 Confirmation of antibody conjugation using BCA assay.** The Bicinchoninic Acid (BCA) assay is a colorimetric technique used to estimate the concentration of proteins in a sample. This is achieved using a sensitive and selective colorimetric detection of the  $\text{Cu}^{1+}$  by bicinchoninic acid (BCA). The reaction takes place in two main steps. First, the biuret reaction takes place where copper is chelated with the protein to produce a light blue complex. This is due to peptides that contain three or more amino acid residues forming a colored chelate complex with cupric ions. In the second step, BCA reacts with the cation produced in step one. This results in the chelation of two BCA molecules with one cuprous ion and forms an intense purple-colored product. This BCA and copper complex is soluble in water and can exhibit intense linear absorbance at 562 nm [98].

The BCA assay kit used was the QuantiPro™ BCA assay kit, which was purchased from Sigma-Aldrich. It consisted of two reagents: BCA reagent A and BCA reagent B. BCA reagent A is a mixture of sodium carbonate, sodium bicarbonate, bicinchoninic acid and sodium tartrate in 0.1 M sodium hydroxide; while BCA reagent B contains 4% cupric sulfate. In order to run the assay, 3 mL of BCA reagent A and 3 mL of BCA reagent B are added to a test tube. To this, 100  $\mu\text{L}$  of copper (II) sulfate solution is added. The test tube is shaken gently until the liquids inside turned a light green color. The control liposomes, as well as Trastuzumab-conjugated immunoliposomes, are used to determine the protein concentration in both. Samples were prepared in 2-mL Eppendorf tubes according to the measurements given in Table

3. Tubes labeled N were assigned for control liposomes, while T to denote immunoliposomes.

Table 3: Sample preparation for BCA Assay

Sample Tube	BCA reagent ( $\mu\text{L}$ )	PBS solution ( $\mu\text{L}$ )	Liposomes ( $\mu\text{L}$ )
Blank	500	500	-
N1	500	450	50
N2	500	450	50
N3	500	400	100
N4	500	400	100
T1	500	450	50
T2	500	450	50
T3	500	400	100
T4	500	400	100

Each sample in the tube adds up to 1 mL. Once the samples are prepared, they are left in a water bath at 60 °C for the reaction to take place. The absorbance for each sample was measured using the Evolution™ 60S UV-Visible Spectrophotometer (ThermoFisher Scientific, Madison, WI, USA) with the software VISIONlite at 562 nm.

### 3.5 Low-Frequency Ultrasound Release Experiments

Release studies were carried out to understand the release of Doxorubicin from liposomes using low-frequency ultrasound (LFUS) at 20 kHz. The fluorescence was recorded using a QuantaMaster QM 30 Phosphorescence Spectrofluorometer (Photon Technology International, Edison NJ, USA). The emission wavelength of DOX is 595 nm, while its excitation wavelength is around 485 nm [99]. The sample is prepared by dilution 75  $\mu\text{L}$  of liposomes with 3 mL of PBS solution. It is then transferred to a fluorescence cuvette. Once the cuvette is placed into the spectrofluorometer chamber, the low-frequency ultrasonic probe was inserted into it. The baseline for the spectrofluorometer was recorded for the first 60 seconds in the absence of US. Pulsed sonication is then introduced with a 20-seconds on, 20-seconds off cycle for a total of



5 minutes. Once a fluorescence plateau was established, Ten  $\mu\text{L}$  of the surfactant Triton X-100 were added to the sample to lyse the liposomes and achieve maximum release. The same protocol was carried out three times at each power density. Settings of 20%, 25%, and 30% on the Vibra display correspond to power densities of 7.46, 9.85, and 17.31  $\text{mW}/\text{cm}^2$ . The percent of DOX released could be determined using equation 3:

$$\%Release = \frac{f_{US} - f_i}{f_{full} - f_i} \times 100\% \quad (3)$$

where  $f_i$  is the initial fluorescence before any release took place,

$f_{US}$  is the fluorescent signal after sonication

and  $f_{full}$  is fluorescence after complete DOX release using Triton X-100

### 3.6 Mathematical Modeling of Drug Release

In drug delivery systems, controlled release is an important parameter for an effective outcome. Various mathematical models can be used for this purpose to understand the kinetics of drug release. It also allows the measurement of certain physical parameters like the drug diffusion coefficient [100]. Noyes and Whitney offered the fundamental principle for drug release kinetics through the given equation:

$$\frac{dM}{dt} = KS(C_s - C_t) \quad (4)$$

where  $M$  is the mass transferred with respect to time,  $t$ ,  $S$  is the instantaneous surface,  $C_t$  is the concentration at time  $t$  and  $C_s$  is the equilibrium solubility of the solute at the experimental temperature. Professor Takeru Higuchi is commonly known as the ‘father’ of mathematical modeling of drug delivery. In 1961, he formulated an equation for the drug release from an ointment base containing an excess amount of insoluble drug. Numerous models have since then been proposed to model drug release and shed light on the mechanism(s) at play. These models can be divided into two main ones: empirical/semi-empirical and mechanistic ones. The empirical/semi-empirical model is not based on physical, chemical, or biological phenomena. Hence, they provide limited insight into the actual drug release mechanisms.

These models also exhibit low predictive powers except in the case of artificial neural networks (ANNs). In contrast, mechanistic models are derived using physical

phenomena such as dissolution, swelling, diffusion, erosion, and precipitation. These can help in the quantitative prediction of processing parameters such as the tablet height and radius. Consequently, it is easier to predict various factors, such as composition, size, shape, and preparation [101]. The following must be taken into account while developing mathematical models for drug release:

1. As the complexity of the model increases, so does the accuracy of the mathematical theory. This means that if more realistic phenomena are considered, the approach becomes more practical and predictive.
2. The theoretical predictions need to be benchmarked against experimental data. To ensure accuracy, different properties need to be calculated and compared, such as dry mass loss, drug release kinetics, wet weight changes, etc.
3. There is no universal mathematical model that can be applied to all drug delivery systems. Some theories can be applied to a broader range of systems, while many others are quite limited in terms of application.
4. In case of adverse evidence after the experiment, the theoretical hypothesis of the model must be discarded [101].

In this thesis, nine mathematical models will be used to predict the acoustic release of Dox from immunoliposomes mathematically. These models are explained in depth in the following sections.

**3.6.1 Zero-order model.** The zero-order kinetic model is best suited for drug delivery systems where the surface area of the nanocarrier does not change, and equilibrium conditions cannot be measured. This equation can be applied to various pharmacological situations such as transdermal systems, osmotic systems, and matrix tablets [102]. It is represented by equation 5.

$$C_t = C_0 + k_0 t \quad (5)$$

where  $C_t$  = drug released at time t

$C_0$  = initial drug amount

$k_0$  = zero order release constant

**3.6.2 First-order model.** In 1967, Gibaldi and Feldman were the first to propose this theorem to model the dissolution of drugs. Other phenomena, such as absorption and elimination of drugs, have also been explained using this model [102]. The Noyes-Whitney equation was established for the dissolution of solid particles in a liquid medium and is given by equation 6.

$$\frac{dC}{dt} = k(C_s - C) \quad (6)$$

where  $C$  is the solute concentration at time  $t$

$C_s$  = solubility at equilibrium

$k$  = first order proportionality constant

**3.6.3 Higuchi model.** The Higuchi model was developed to investigate the release of water-soluble drugs in solid matrices. The following homogenous matrix equation was obtained as shown in equation 7.

$$f = Q = \sqrt{D(2C - C_s)C_s t} \quad (7)$$

where  $Q$  = drug release per unit area at time  $t$

$C$  = initial drug concentration

$C_s$  = drug solubility in matrix media

$D$  = diffusion constant

The equation was first developed by Higuchi to explain the dissolution of drugs in an ointment base. [102].

**3.6.4 Korsmeyer-Peppas model.** The Korsmeyer-Peppas equation, known as the power-law model, is an easy-to-apply equation, as shown below in equation 8:

$$\frac{M_t}{M_\infty} = kt^n \quad (8)$$

where  $M_t$  = cumulative absolute amount of drug released at a specific time  $t$

$M_\infty$  = cumulative absolute amount of drug released at infinite time

$k$  = constant including structural and geometric features

$n$  = release exponent

Nicholas Peppas was the first to introduce this equation to the world of drug delivery in 1985. A release exponent of 0.5 indicates the drug is released via diffusion. Different release values have been calculated for other geometries, as shown in Table 4. In the case of the overlapping of different types of transport mechanisms such as drug diffusion and polymer swelling, release exponents between these values are used [101].

Table 4: Release values for Korsmeyer Peppas Model [101]

Thin Film	Exponent, n		Drug release mechanisms
	Cylinder	Sphere	
0.5	0.45	0.43	Fickian diffusion
$0.5 < n < 1.0$	$0.45 < n < 0.89$	$0.43 < n < 0.85$	Anomalous transport
1.0	0.89	0.85	Polymer swelling

**3.6.5 Weibull model.** The Weibull model is an empirical model that was first introduced by Weibull in 1951 for the dissolution and release of drug systems. This equation can be used in almost all dissolution studies without other modifications [102]. Equation 9 shows how the model can be applied to pharmaceutical drug dosage.

$$m = 1 - \exp\left[\frac{-(t - T_i)^b}{a}\right] \quad (9)$$

where  $m$  = Accumulated fraction of drug at time  $t$

$a$  = scale parameter defining the time scale of the process

$T_i$  = location parameter representing time-lag before release

$b$  = a shape parameter which has three different cases:

- Case 1 if  $b > 1$ : sigmoid or S-shaped with an upward curve
- Case 2 if  $b = 1$ : exponential curve
- Case 3 if  $b < 1$ : parabolic with a higher initial slope

The equation can be rearranged as:

$$\log[-\ln(1 - m)] = b \log(t - T_i) - \log a \quad (10)$$

However, since the Weibull model is empirical, it has several limitations. First, it does not properly characterize the kinetic dissolution properties of the drug. Second, no single parameter exists for the intrinsic dissolution of the drug. And lastly, it cannot be used adequately in *in vivo* and *in vitro* applications [102].

**3.6.6 Hixson-Crowell model.** Hixson and Crowell proved that the area of a regular particle is directly proportional to the cubic root of its volume and is established the following the equation:

$$W_o^{1/3} - W_t^{1/3} = K_s t \quad (11)$$

where  $W_o$  = initial drug concentration

$W_t$  = remaining drug at time t

$K_s$  = constant for surface – volume relation

This model is widely applied to tablets where the dissolution takes place in a plane parallel to the surface of the tablet. In cases where the dimensions of the tablet diminish, the equation can be modified as follows:

$$W_o^{1/3} - W_t^{1/3} = \frac{KN^{1/3}DC_s t}{\delta} \quad (12)$$

where  $N$  = number of particles

$K$  = a constant related to shape, surface and particle density

$D$  = a diffusion constant

$C_s$  = solubility concentration at equilibrium

$\delta$  = diffusion layer thickness

There are certain assumptions used to keep in mind when applying this model. First, it is assumed that the rate of release is limited by the dissolution rate and not by

diffusion. Second, the model has been developed by considering the diminishing surface of the drug particles during dissolution [102].

**3.6.7 Baker-Lonsdale model.** Baker and Lonsdale developed this model from the Higuchi's equation, and they described the release of drug from a spherical matrix [102]. It is defined in equation 13.

$$\frac{3}{2} \left[ 1 - \left( 1 - \frac{M_t}{M_\infty} \right)^{2/3} \right] - \frac{M_t}{M_\infty} = \frac{3D_m C_{ms}}{r_0^2 C_0} t \quad (13)$$

where  $M_t$  = drug released at time  $t$

$M_\infty$  = drug released at infinite time

$D_m$  = diffusion coefficient

$C_{ms}$  = drug solubility in matrix

$r_0$  = radius of the spherical matrix

$C_0$  = initial drug concentration

In cases where the matrix is not homogenous, and fractions or capillaries may be present, equation 14 is used.

$$\frac{3}{2} \left[ 1 - \left( 1 - \frac{M_t}{M_\infty} \right)^{2/3} \right] - \frac{M_t}{M_\infty} = \frac{3D_f C_{fs} \varepsilon}{r_0^2 C_0 \tau} t \quad (14)$$

where  $D_f$  = diffusion coefficient

$C_{fs}$  = solubility of the drug in the surrounding matrix

$\tau$  = tortuosity factor of the capillary system

$\varepsilon$  = porosity of the matrix

In the case of linearization of release data from liposomes, the following equation 15 can be used with release constant  $k$ .

$$\frac{3}{2} \left[ 1 - \left( 1 - \frac{M_t}{M_\infty} \right)^{2/3} \right] - \frac{M_t}{M_\infty} = kt \quad (15)$$

**3.6.8 Hopfenberg model.** The Hopfenberg Model is a semi-empirical model that allows quantifying drug release from degradable drug delivery systems. It states that the rate of release is proportional to the surface area of the device. It is assumed that all mass transfer processes add up to a single zero-order process with the rate constant  $k_0$ . This might be a result of either a single physical or chemical phenomenon or a superimposition of various phenomena such as swelling, dissolution, and polymer chain breakage. It can be noted that this model ignores edge end effects [101]. The model for this model is given below in equation 16.

$$M_t = M_\infty \left[ 1 - \left( 1 - \frac{k_0 t}{c_0 a} \right)^n \right] \quad (16)$$

where  $M_t$  = cumulative absolute amount of drug released at a specific time  $t$

$M_\infty$  = cumulative absolute amount of drug released at infinite time

$c_0$  = initial drug concentration

$a$  = radius of cylinder

$n$  = shape factor ( $n=2$  for cylindrical,  $n=1$  for slab and  $n=3$  for spherical).

$k_0$  = corrosion rate constant

**3.6.9 Gompertz model.** This is an exponential model in which there is an initial steep release of drug followed by a converging reduction to optimal release [103]. It is useful in comparing release profiles for drugs with intermediate release rates. It is portrayed by equation 17.

$$X(t) = X_{max} e^{[-e^{(-\alpha(t-\beta))}]} \quad (17)$$

where  $X(t)$  = percent of drug dissolved at time  $t$

$X_{max}$  = maximum dissolution

$\alpha$  = coefficient describing drug release over time

$\beta$  = time at maximum growth rate curve

Both mechanistic and stochastic models have been employed to model the acoustic release of agents from liposomes [104][105] and micelles

[106][107][108][109]. More recently, artificial neural networks were utilized in conjunction with model predictive control to design a feedback controller capable of maintaining a constant and therapeutic concentration of the drug at the tumor site [110]. The utilization of the above models will improve the previous ultrasound-induced drug release predictions, and thus aid in optimizing this drug delivery modality.



## Chapter 4: Results and Discussion

### 4.1 Estimation of liposome size using Dynamic Light Scattering (DLS)

The dynamic light scattering technique was employed to find the radius of the synthesized liposomes. It was also important to measure the poly disparity index to ensure all the liposomes in a given sample are of a uniform size. In this thesis, an upper limit of 20% for the poly disparity was maintained as the criteria. Liposome size is important, and radius must be maintained below 100 nm in order to ensure the EPR effect can take place. The radius of the control liposomes was determined to be  $91.2 \pm 1.47$  nm, while the immunoliposomes are  $94.9 \pm 1.29$  nm. The difference in size is statistically significant, as is evident from the p-value of 0.0316. This trend is predicted as the conjugation of the trastuzumab to the liposomal surface is expected to increase the size of these targeted nanovehicles. Molecules in the range of 100 kDa, such as of Trastuzumab, is expected to increase the liposomal size by at least 2.5 nm. Using electron microscopy techniques such as cryogenic transmission electron microscopy (cryo-TEM) could aid in visualizing the liposome and determining the size and proper differentiation of the control and immunoliposomes. Table 5 gives a summary of the size of the synthesized nanocarriers.

Table 5: DLS results for the size of liposomes

Batches	Control Liposomes		Immunoliposomes	
	Radius (nm)	Poly disparity Index (Pd %)	Radius (nm)	Poly disparity Index (Pd %)
Batch 1	91.5	12	94.5	10.6
Batch 2	92.5	15.4	96.3	11.7
Batch 3	89.6	9.4	93.8	11.2
Average	<b>91.2</b>	<b>12.3</b>	<b>94.9</b>	<b>11.2</b>
Standard Deviation	<b>1.47</b>	<b>3.01</b>	<b>1.29</b>	<b>0.55</b>

## 4.2 Estimation of Lipid Concentration using Stewart's Assay

In this thesis, liposomes were synthesized using DPPC lipid, which is known to absorb light at a wavelength of 485 nm. The amount of lipids used to make liposomes was calculated in mg/mL using the method mentioned in Section 3.4.2. In order to find the exact concentration of lipids, a calibration curve was first generated. This was constructed using known concentrations of DPPC in mg/ml versus the absorbed wavelength. Least squares regression analysis was performed, and a linear plot was obtained, as shown in Figure 16. The almost unity  $R^2$  value (0.9994) and the small intercept value (0.0205) confirm the linearity of the calibration plot.

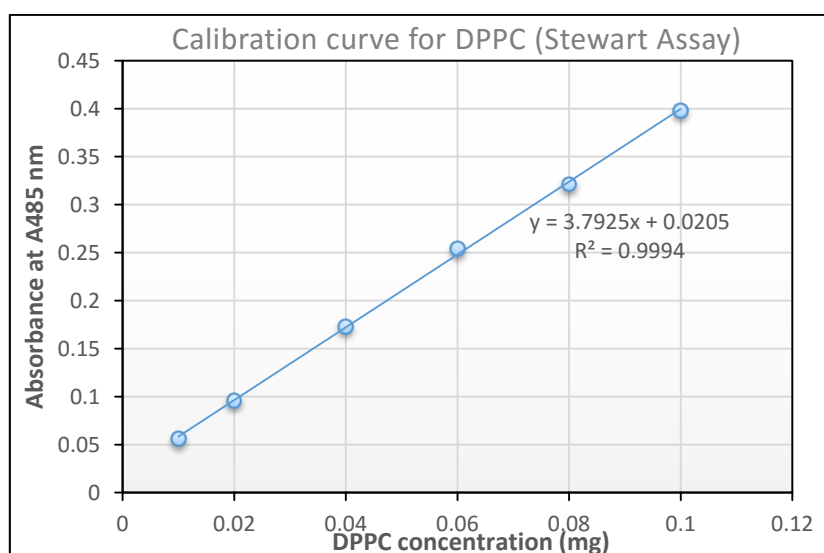


Figure 16: Calibration curve for Stewart Assay

Table 6: Lipid concentration results from Stewart Assay

Batch	Lipid concentration (mg/mL)		NH2 to Trastuzumab ratio
	Control Liposomes	Immunoliposomes	
Batch 1	4.13	1.48	2.79
Batch 2	12.81	4.79	2.67
Batch 3	2.69	1.02	2.64

From Table 5, it can be noted that in every batch of liposomes synthesized, the concentration of lipids in NH<sub>2</sub>-terminated control liposomes was almost 3 folds higher compared to immunoliposomes. This means that there are more lipids present in the control liposomes. This trend is expected since the immunoliposomes are passed through a triple column for purification after the conjugation of trastuzumab process. Passing through the column can also entrap some lipids in its beads, thus reducing the final lipid concentration present in the immunoliposomes. Figure 17 shows the difference in lipid content between the control liposomes and immunoliposomes.

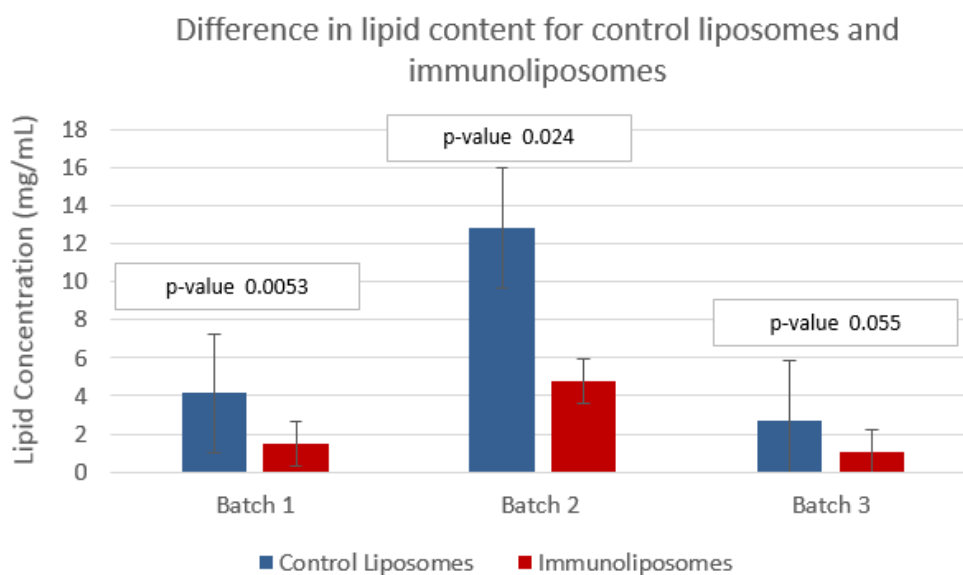


Figure 17: Difference in lipid content for control liposomes and immunoliposomes

#### 4.3 Estimation of Protein Concentration using BCA Assay

The BCA assay was used to determine the protein content in the control and immunoliposomes. The procedure to conduct BCA Assay is explained in detail in Section. 3.4.3. Similar to the Stewart assay, a linear calibration plot was first constructed, as shown in Figure 18. Using this calibration plot and measuring the UV absorbance at 562 nm of various samples using a spectrophotometer, the following values in Table 7 were obtained. Table 7 shows a comparison between the protein content present in the immunoliposomes and control liposomes. It is measured in the unit of  $\mu\text{g/mL}$ .

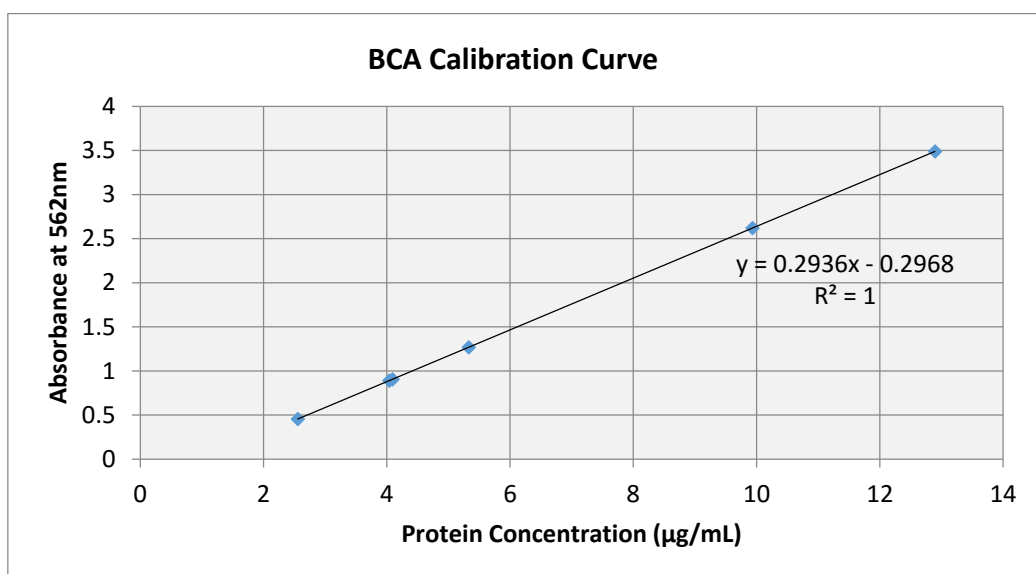


Figure 18: BCA calibration curve

Table 7: Protein concentration results using BCA Assay

Batch	Protein concentration ( $\mu\text{g/mL}$ )	
	Control Liposomes	Immunoliposomes
Batch 1	49.80	80.31
Batch 2	31.26	46.96
Batch 3	43.97	65.07

From the results shown in Table 7, it is evident that the immunoliposomes exhibit a 1.5-time increase in the amount of protein concentration compared to control liposomes and a p-value of 0.113. This follows the expected trend since Trastuzumab is inherently a protein, and hence the immunoliposomes which have conjugated Trastuzumab will show a higher concentration of protein. The control liposomes which do not have any Trastuzumab attached to them also show a significant amount of

protein due to the presence of amine groups in the DSPE-PEG-NH<sub>2</sub> compound. Figure 19 has been constructed to easily understand the difference in protein content between the control and immunoliposomes.

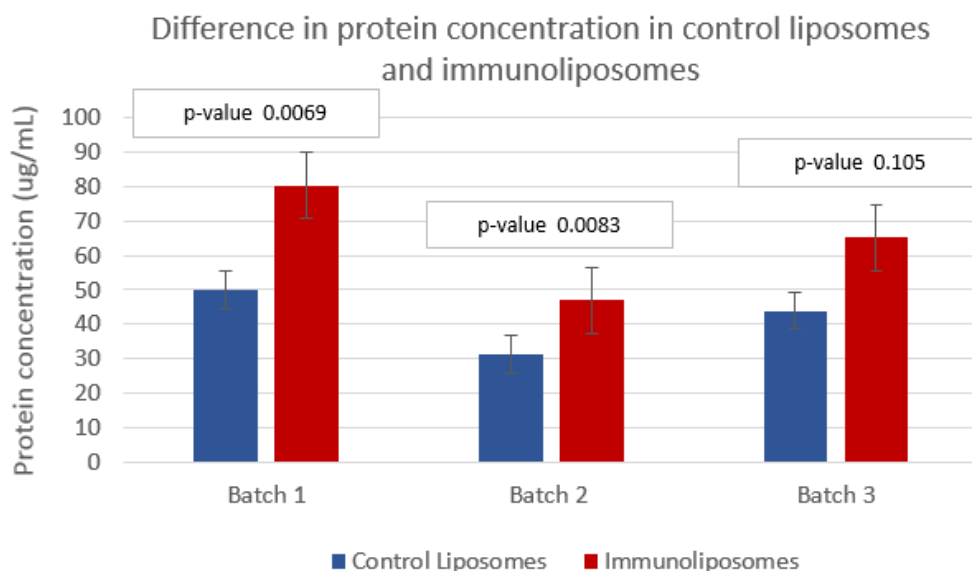


Figure 19: Difference in protein concentration between control liposomes and immunoliposomes

#### 4.4 Low-Frequency Ultrasound (LFUS) Release Studies

Three batches of control liposomes and three batches of trastuzumab conjugated immunoliposomes were prepared and loaded with the chemotherapeutic drug Doxorubicin. LFUS was applied to trigger release, as detailed in Section 3.5. Initially, a fluorescence baseline of 60 seconds was established where no release of the drug took place. This was followed by introducing sonication pulses using a 20-kHz transducer at intervals of 20 seconds. Once the release reached a plateau at around 300 seconds, the surfactant Triton-X was added to lyse the liposomes and achieve maximum release. This was repeated at the three different power densities of 7.46, 9.85, and 17.31 mW/cm<sup>2</sup>. Sections 4.4.1 and 4.4.2 display and discuss the results of release profiles obtained by applying LFUS to control and immunoliposomes.

**4.4.1 LFUS release results for control liposomes.** Figure 20 represents the normalized release profile of control liposomes at the three different power densities.

The first 60 seconds represent the baseline recorded in the absence of ultrasound. Since the encapsulated DOX is at self-quenched concentrations, it does not emit very little fluorescence, and hence the baseline is approximately 0. Once ultrasound is applied for a pulse of 20 seconds, the cumulative frequency release (CFR) increases, indicating the release of the drug. At the 20 seconds OFF pulses in the absence of ultrasound, the liposomes reassemble and do not release any drug. This trend is observed for 300 seconds where, at that point, Triton-X is added. This surfactant lowers the surface tension of the fluids, causing the total rupture of the liposomes, indicating maximum release of the drug. It can also be observed that the release rate is lowest at  $7.46 \text{ mW/cm}^2$  and highest at  $17.31 \text{ mW/cm}^2$ . This indicates that the release rate increases as the power density increases.

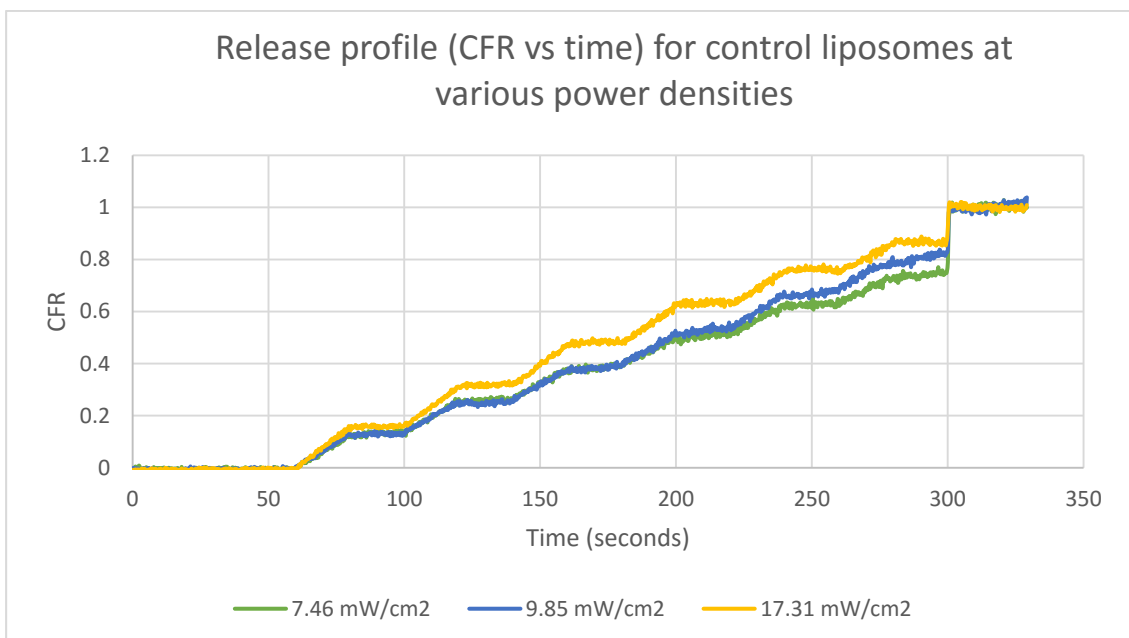


Figure 20: Normalized release profiles for control liposomes at three different power densities

In order to understand the release rate per ON pulse of ultrasound, Figure 21 was constructed. This represents the average CFR for the first four pulses and maximum release as a function of power densities. It is interesting to note that the CFR increases with an increase in power density as well as an increase in pulse. It is also observed that the release for the first, second, third, and fourth pulses are almost equal for  $7.46$  and  $9.85 \text{ mW/cm}^2$  power densities. However, at the maximum release, the power density

does not play a crucial factor since almost 100% release is achieved for all 3 trials, irrespective of power density.

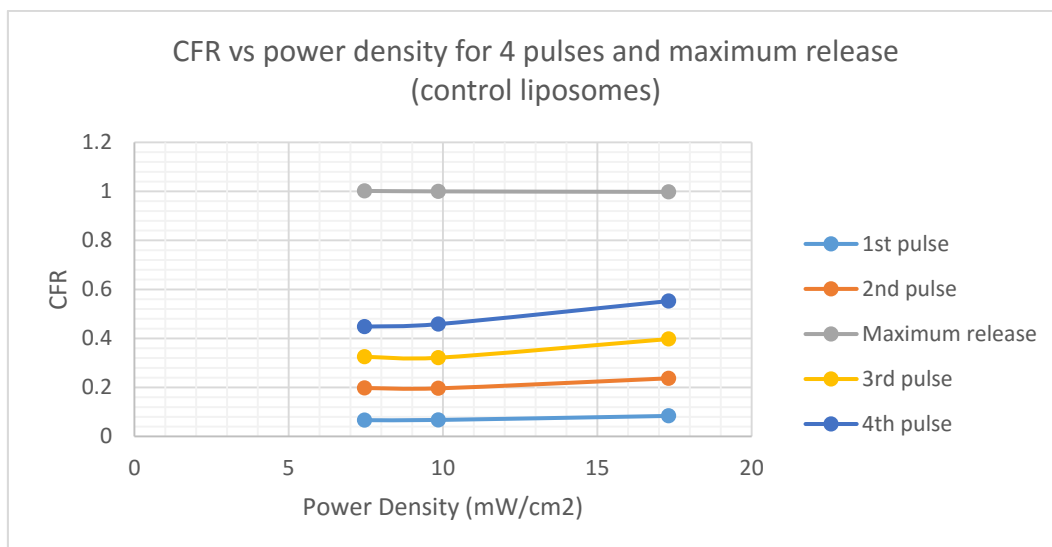


Figure 21: CFR vs. power density for 4 pulses and maximum release for control liposomes

Another plot was constructed to understand and compare the release for the first four pulses at each power density, as illustrated in Figure 22. This follows the expected trend that the amount of drug released increases in each pulse for every power density. However, for the second pulse, the rate of release is almost equal at 7.46 and 9.85 mW/cm<sup>2</sup>.

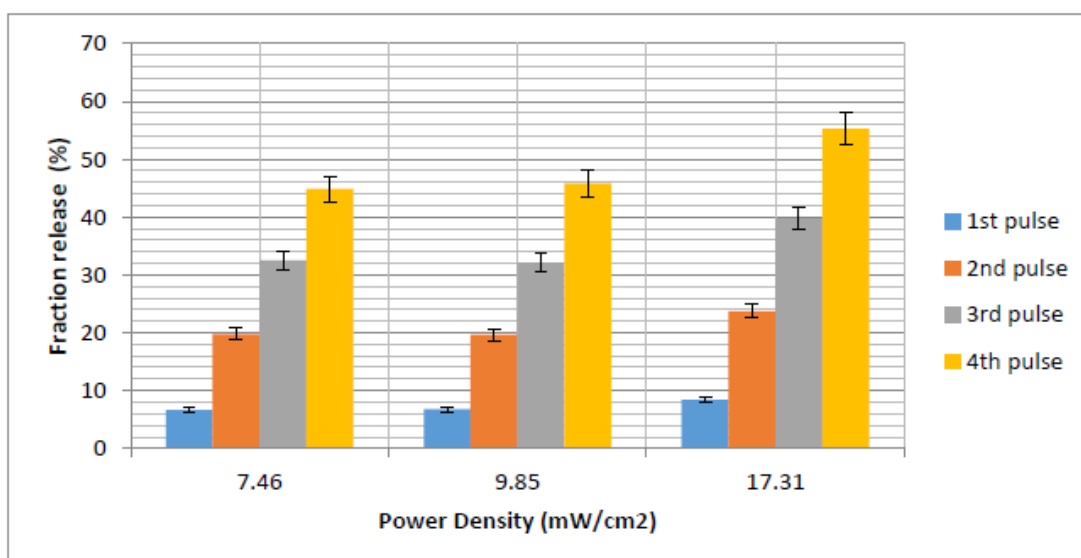


Figure 22: Pulse wise fraction release for the first four pulses of control liposomes

#### 4.4.2 LFUS release results for trastuzumab-conjugated immunoliposomes.

The same release studies were conducted using immunoliposomes. Figure 23 is the normalized release profile for trastuzumab conjugated immunoliposomes at the three power densities using the same protocol as that followed for the control liposomes. Triton-X was added at 300 seconds in order to lyse the liposomes and achieve maximum release. However, the release profile is quite different from the control liposome release profile. There is only a very slight difference between the release rates for the three different power densities. In addition, the release profiles for 7.46 mW/cm<sup>2</sup> and 9.85 mW/cm<sup>2</sup> appear to be almost identical. They do, however, follow the expected trend that as power density increases, the release also increases.

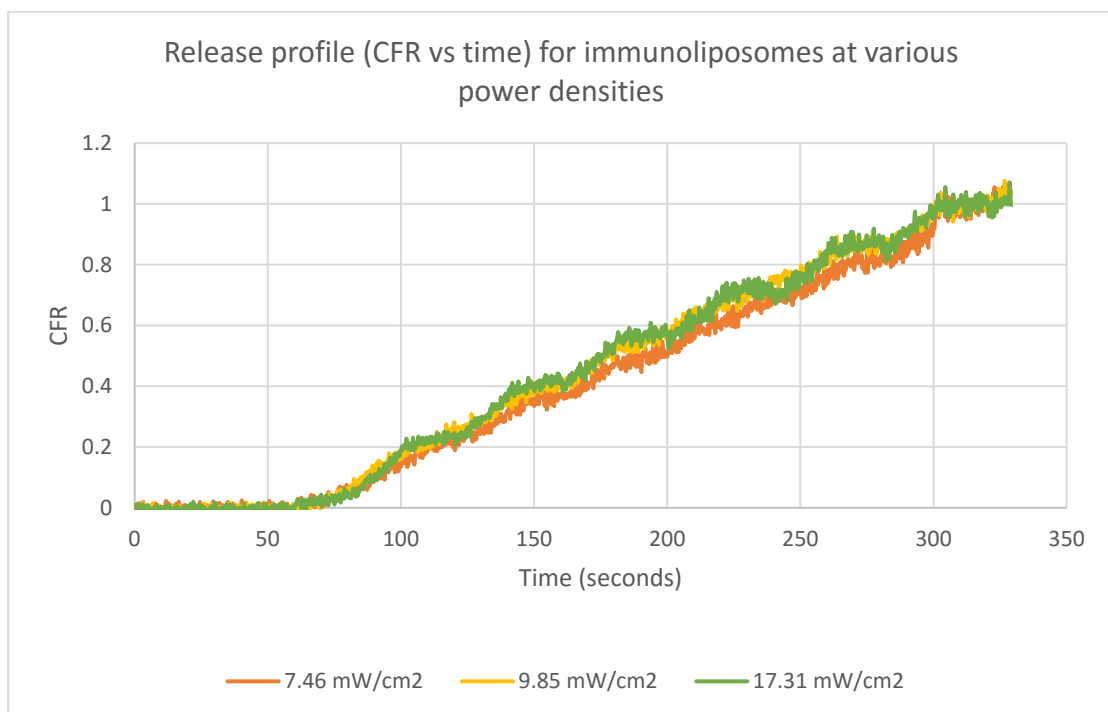


Figure 23: Normalized release profiles for immunoliposomes at three different power densities

Figure 24 portrays a comparison in CFR for the first four pulses and maximum release at the three different power densities. Again, it is evident that the release rates for 9.85 mW/cm<sup>2</sup> and 17.31 mW/cm<sup>2</sup> are very similar for the first four pulses. The maximum release is also almost 100% for all three power densities.



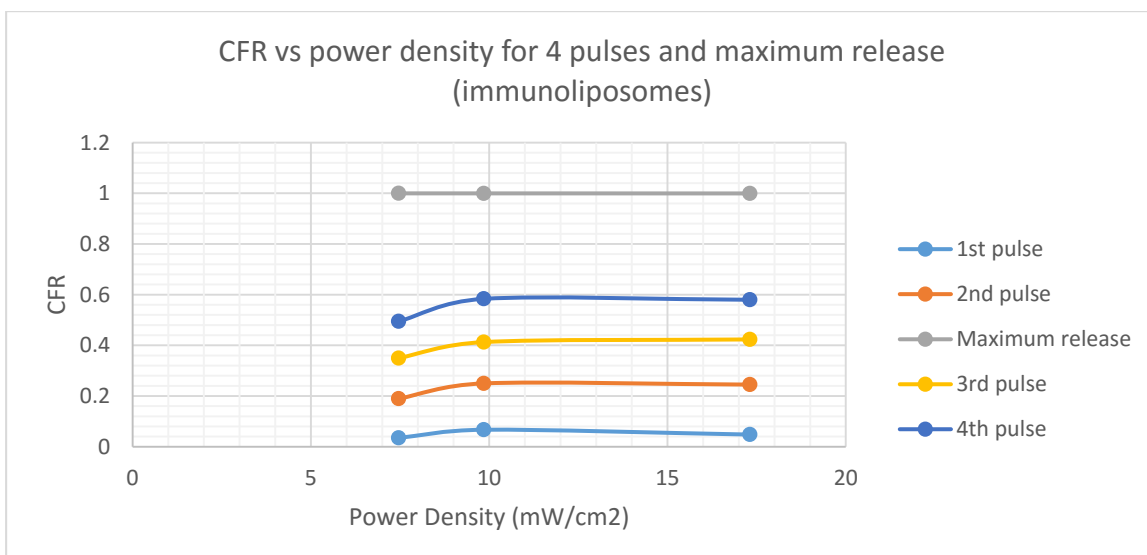


Figure 24: CFR vs. power density for 4 pulses and maximum release for immunoliposomes

Finally, a plot was constructed to compare the differences in the fractions released in the first four pulses for the three power densities investigated, as shown in Figure 25. For the first pulse, a power density of 9.85 mW/cm<sup>2</sup> releases the most amount of drugs. For the second, third, and fourth pulses, the release rates using 9.85 and 17.31 mW/cm<sup>2</sup> are very similar, while release using 7.46 mW/cm<sup>2</sup> was the lowest.

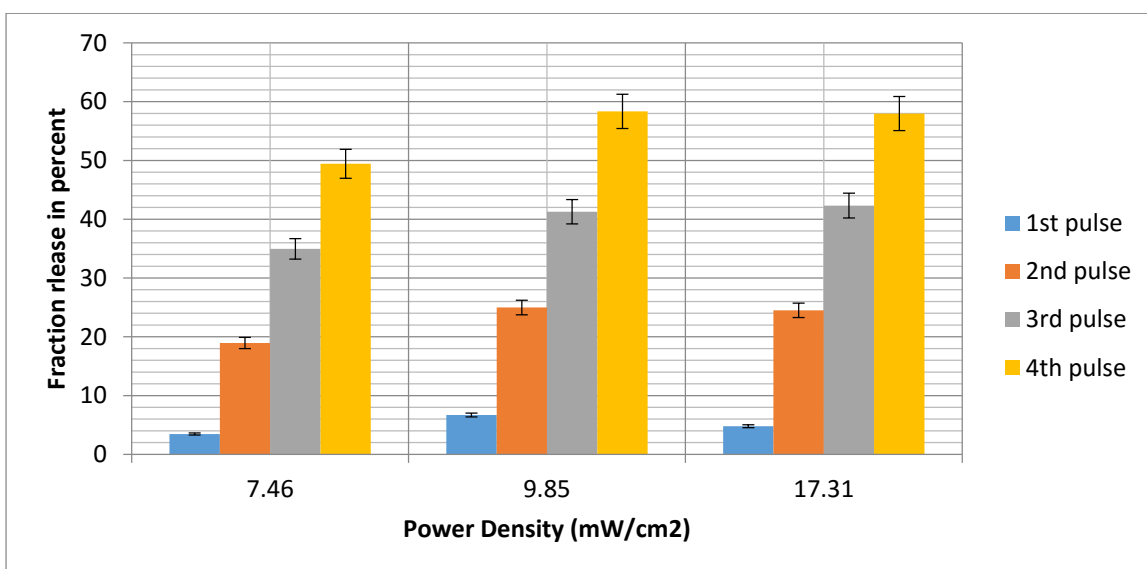


Figure 25: Pulse wise fraction release for first four pulses for immunoliposomes

#### 4.4.3 Comparison in release profiles for control and immunoliposomes.

This section summarizes the results presented in Sections 5.4.1 and 5.4.2 and compares

the pulsed release rates for control and immunoliposomes. Figure 26 shows the normalized release profiles of control liposomes and immunoliposomes at the three power densities. As mentioned before, the release rates increase with an increase in power density. It is also evident that the release of DOX from the immunoliposomes is slightly higher than the control liposomes, especially after the first few pulses. In both cases, a steep increase in CFR is observed at 300 seconds, after the addition of the surfactant to lyse the liposomes.

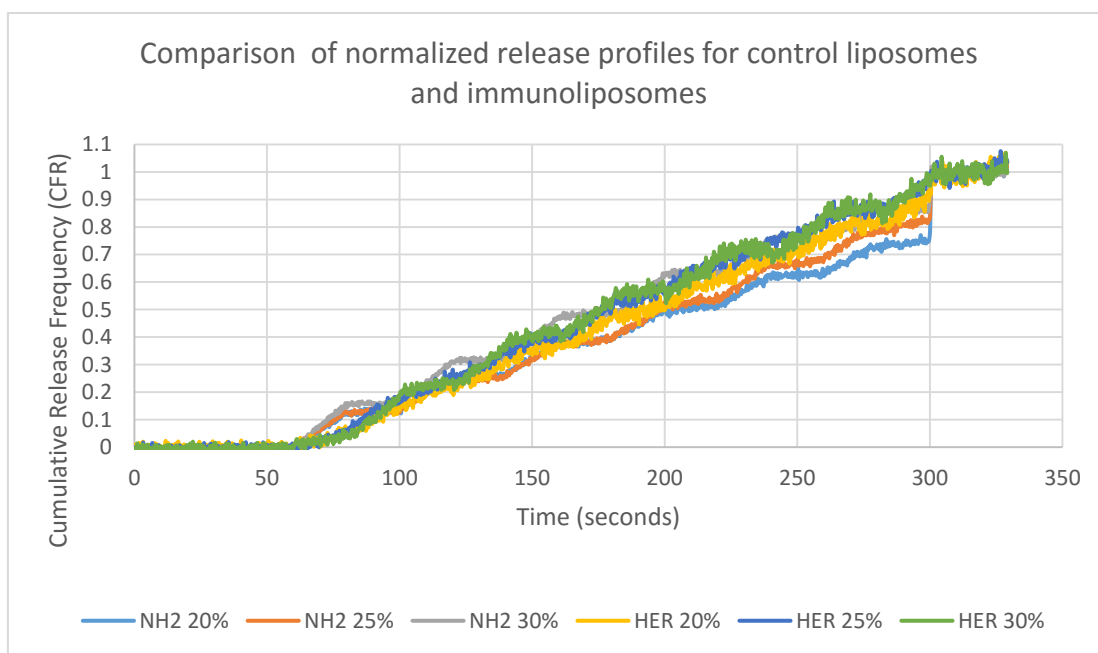


Figure 26: Comparison of normalized release profiles for control liposomes and immunoliposomes

Four different plots were constructed, displaying the difference in acoustic release rates of the anti-neoplastic agent from control and immunoliposomes at the first four pulses. Figure 27 shows that the control liposomes release significantly more drug at 7.46 and 17.31 mW/cm<sup>2</sup>, while at 9.85 mW/cm<sup>2</sup>, no statistically significant difference is observed (this is discussed in further details in the section below). This actually does not follow the expected trend. Literature shows that conjugated liposomes are more echogenic, i.e., sensitive to ultrasound. This means that ideally, the release rate should be higher for the immunoliposomes compared to the control liposomes. The trend seems to be changing for the second pulse, as displayed in Figure 28. In this case, a slightly higher release rate is observed at 9.85 and 17.31 mW/cm<sup>2</sup> power densities. For the third pulse, as seen in Figure 29, the release percent is higher for immunoliposomes

compared to control liposomes at all three power densities. Finally, the fourth pulse (Figure 30) also follows a similar pattern as that of the third pulse, where the immunoliposomes display greater release than the control liposomes.

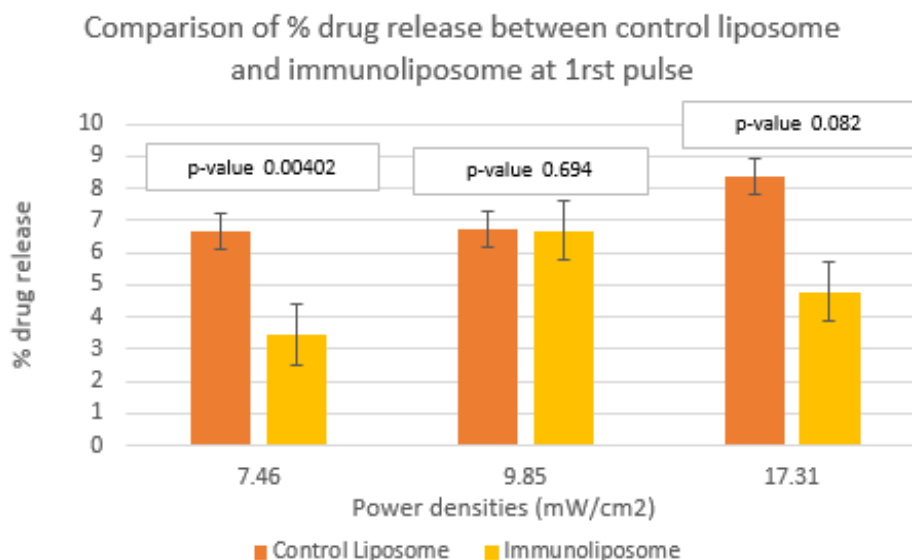


Figure 27: Comparison of % drug release between control liposome and immunoliposomes at 1st pulse

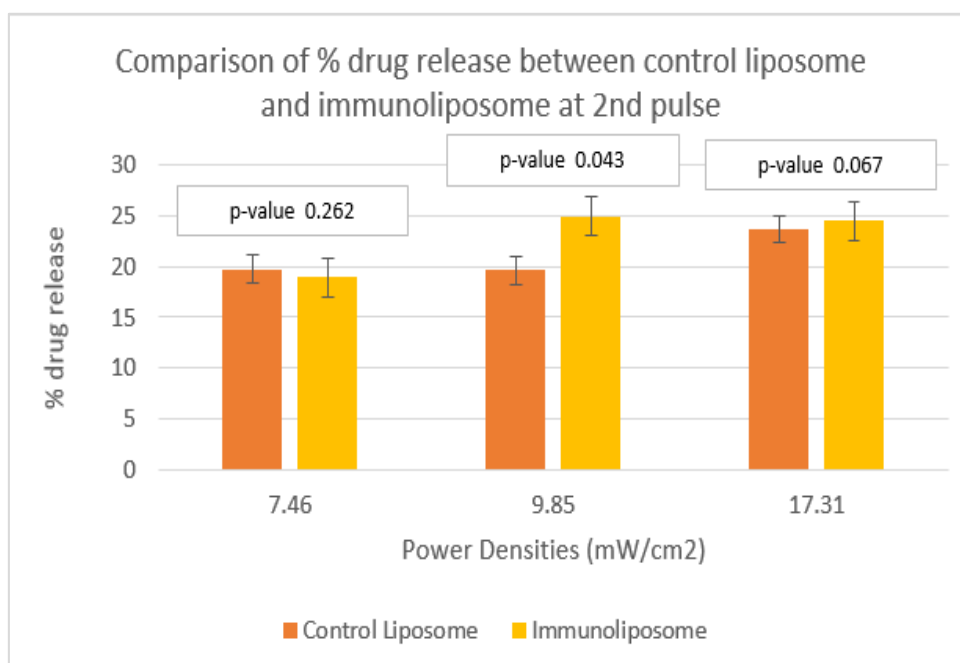


Figure 28: Comparison of % drug release between control liposome and immunoliposomes after the 2nd pulse

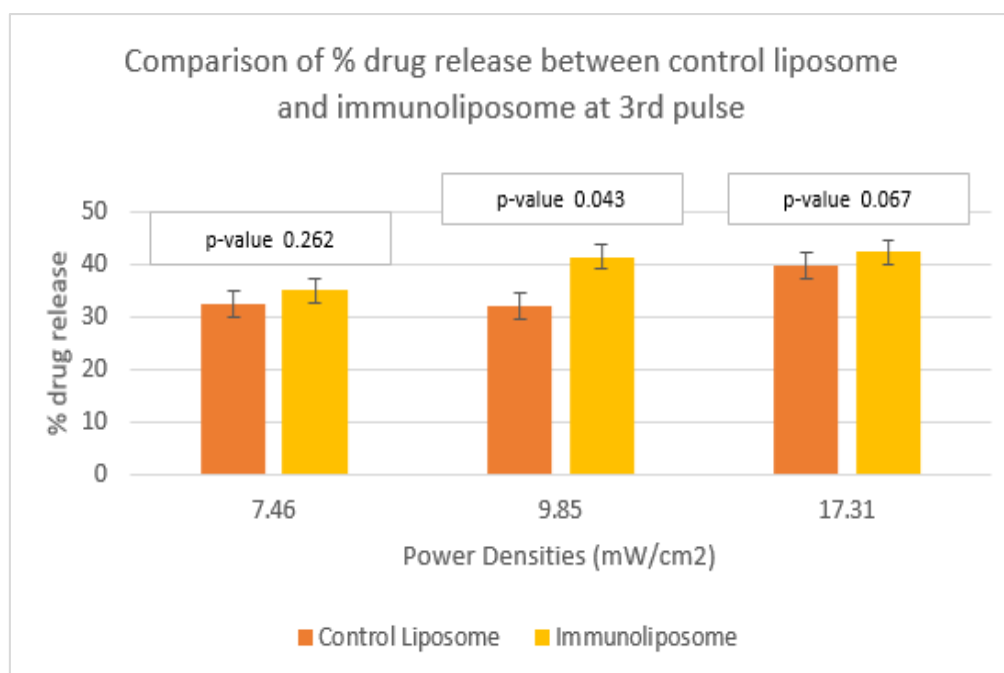


Figure 29: Comparison of % drug release between control liposome and immunoliposomes after the 3rd pulse

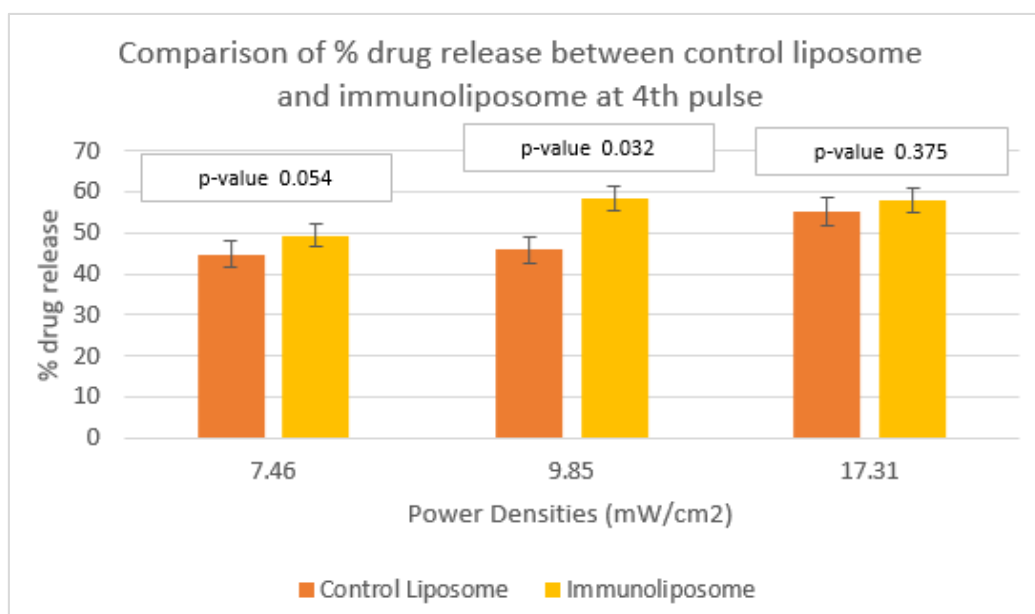


Figure 30: Comparison of % drug release between control liposome and immunoliposomes after the 4th pulse

To test the statistical significance, a two-tailed t-test was performed for all the four pulses at the three power densities for both control liposomes and immunoliposomes. A two-tailed t-test is done to understand if the mean is significantly higher than or significantly lower than the mean population. Tables 8, 9, 10, and 11 represent the heat map for p-values for the pulses one, two, three and four respectively. A p-value of less than 0.05 or conversely, a confidence level of 0.95 is assumed to be statistically significant throughout this thesis. It was observed that the p-values were not consistent throughout the pulsed releases at all power densities. Release at the fourth pulse at various power densities, when comparing control liposomes and immunoliposomes, was the most statistically significant with the lower p-values.

Table 8: Heat map of p-test: Comparison between control liposomes and immunoliposomes after the first pulse

1rst Pulse	Power Density (%)	Control Liposomes			Immunoliposomes		
		20%	25%	30%	20%	25%	30%
Control Liposomes	20%		0.01161	0.00067	0.00402	0.18187	0.01945
	25%	0.01161		0.00066	0.00111	0.69417	0.03491
	30%	0.00067	0.00066		0.00042	0.03512	0.08240
Immunoliposomes	20%	0.00402	0.00111	0.00042		0.03512	0.00477
	25%	0.18187	0.69417	0.03512	0.00394		0.03515
	30%	0.01945	0.03491	0.08240	0.00477	0.03515	

$p \geq 0.05$	$0.04 \leq p < 0.05$	$0.03 \leq p < 0.04$	$0.02 \leq p < 0.03$	$0.01 \leq p < 0.02$	$p < 0.01$
---------------	----------------------	----------------------	----------------------	----------------------	------------

Table 9: Heat map of p-test: Comparison between control liposomes and immunoliposomes after the second pulse

2 <sup>nd</sup> Pulse	Power Density (%)	Control Liposomes			Immunoliposomes		
		20%	25%	30%	20%	25%	30%
Control Liposomes	20%		0.01972	0.00433	0.262	0.01656	0.00229
	25%	0.01972		0.06033	0.02046	0.043	0.00823
	30%	0.00433	0.06033		0.00470	0.02294	0.067
Immunoliposomes	20%	0.262	0.02046	0.00470		0.01830	0.00234
	25%	0.01656	0.043	0.02294	0.01830		0.00555
	30%	0.00229	0.00823	0.067	0.00234	0.00555	

$p \geq 0.05$	$0.04 \leq p < 0.05$	$0.03 \leq p < 0.04$	$0.02 \leq p < 0.03$	$0.01 \leq p < 0.02$	$p < 0.01$
---------------	----------------------	----------------------	----------------------	----------------------	------------

Table 10: Heat map of p-test: Comparison between control liposomes and immunoliposomes at the third pulse

3 <sup>rd</sup> Pulse	Power Density (%)	Control Liposomes			Immunoliposomes		
		20%	25%	30%	20%	25%	30%
Control Liposomes	20%		0.01058	0.00051	0.26223	0.00038	0.00243
	25%	0.01058		0.10382	0.01193	0.04372	0.02909
	30%	0.00051	0.10382		0.00008	0.13754	0.06677
Immunoliposomes	20%	0.26223	0.01193	0.00008		0.00008	0.00255
	25%	0.00038	0.04372	0.13754	0.00008		0.12786
	30%	0.00243	0.02909	0.06677	0.00255	0.12786	

$p \geq 0.05$	$0.04 \leq p < 0.05$	$0.03 \leq p < 0.04$	$0.02 \leq p < 0.03$	$0.01 \leq p < 0.02$	$p < 0.01$
---------------	----------------------	----------------------	----------------------	----------------------	------------

Table 11: Heat map of p-test: Comparison between control liposomes and immunoliposomes at the fourth pulse

4th Pulse	Power Density (%)	Control Liposomes			Immunoliposomes		
		20%	25%	30%	20%	25%	30%
Control Liposomes	20%		0.0044	0.0015	0.0540	0.0021	0.0010
	25%	0.0044		0.1911	0.0088	0.032	0.0176
	30%	0.0015	0.1911		0.0010	0.5545	0.375
Immunoliposomes	20%	0.0540	0.0088	0.0010		0.0020	0.0012
	25%	0.0021	0.032	0.5545	0.0020		0.0252
	30%	0.0010	0.0176	0.375	0.0012	0.0252	

$p \geq 0.05$	$0.04 \leq p < 0.05$	$0.03 \leq p < 0.04$	$0.02 \leq p < 0.03$	$0.01 \leq p < 0.02$	$p < 0.01$
---------------	----------------------	----------------------	----------------------	----------------------	------------

#### 4.5 Mechanical Index

The mechanical index is a parameter used to determine whether cavitation can take place or not. It is represented by the following equation.

$$MI = \frac{P_{negative}}{\sqrt{f}} \quad (18)$$

where  $P_{negative}$  is the negative pressure in MPa

$f$  is the frequency in MHz.

The mechanical index is dependent on the intensity of the LFUS and the acoustic impedance of water to mimic the water content present in human tissues. In this thesis, three power densities were used: 7.46, 9.85, and 17.31 mW/cm [111]. Equation 18 was applied to find the mechanical indices at these power densities and were determined to be 0.11, 0.12, and 0.16, respectively. According to The British Medical Ultrasound Society, a mechanical index of 0.7 is chosen as the threshold of cavitation, and a mechanical index of more than 1.0 may cause detrimental effects to

the tissues [112]. Hence, the power densities used in this experiment are well within the safe range and can be used on human tissues. A mechanical index of 0.3 to 0.4 is considered the threshold between stable and collapse cavitation. Since all the mechanical indices in this work are below 0.3 (0.11, 0.12, and 0.16), it can be deduced that drug release from targeted and non-targeted liposomes is caused by stable cavitation.

#### **4.6 Discussion and Further Insights**

In this thesis, pulsed sonication was applied to release DOX from targeted and non-targeted liposomes, where ultrasound was ON for 20 seconds and OFF for 20 seconds. Pulsed sonication is advantageous over the use of continuous ultrasound because prolonged exposure to acoustic energy could lead to hyperthermia. Mild hyperthermia (37 °C to 43 °C) does not cause any permanent adverse effects to nearby healthy tissues. Additionally, mild hyperthermia aids in increasing the permeability of cells and liposomes. However, further prolonged periods of exposure to ultrasound could lead to severe hyperthermia (>43°C), which could cause permanent structural changes in the DNA of healthy cells. Hence, pulsed sonication is favored over continuous acoustic exposure because it minimizes the adverse effects of hyperthermia as well as helps to obtain optimal drug release.

From the results of the normalized release profiles (Figure 20 and Figure 23), it is observed that the release of the drug is similar at all three power densities for the initial few pulses. However, as time lapses, it is evident from the results that power density does play a role in the release profile of the drug. A power density of 17.31 mW/cm<sup>2</sup> releases more drug compared to a power density of 9.85 mW/cm<sup>2</sup>. Similarly, a power density of 9.85 mW/cm<sup>2</sup> releases more drug compared to a power density of 7.46 mW/cm<sup>2</sup>, notably towards the end of the release profile. This observation is useful and can be applied for potential clinical applications. An optimal drug release profile could be obtained by initially applying low-intensity ultrasound to the liposomes for a certain period of time, followed by the application of a higher intensity ultrasound. Hence, using lower acoustic power can produce maximum drug release, while maintaining the efficiency of the treatment.



Additionally, by comparing the release profiles of control liposomes and immunoliposomes at the first four pulses (Figures 27, 28, 29, and 30), it can be concluded in general that immunoliposomes are capable of releasing more drug than control liposomes. Thus, the addition of Trastuzumab; the monoclonal antibody, essentially serves two purposes. First, Trastuzumab can identify and bind to the overexpressed HER2 receptors on the surface of breast cancer cells. This facilitates the delivery of antineoplastic agents exclusively to cancer cells via receptor-mediated endocytosis, while avoiding healthy cells in the body. Second, as the results above showed, the addition of the monoclonal antibody makes the liposome more echogenic and sensitive to ultrasonic pulses. This results in a high DOX release from the immunoliposomes compared to a liposome without any moiety conjugated to its surface. Hence, the conjugation of moieties such as small molecules, polypeptide sequences, proteins, or antibodies to the surface of nanocarriers provides a dual benefit for this type of drug delivery system.

Various experimental errors exist which could have affected collected data reported in this thesis. Although DOX is a cancer drug (and hence was not synthesized for its fluorescent properties such as calcein), it is intrinsically fluorescent and hence proved useful for the online low-frequency ultrasound studies in this thesis. However, the noise exhibited by fluorescence studies utilizing DOX (when compared to calcein) was higher and might have masked differences in release kinetics at different power densities, when using the two carriers investigated nanocarriers. Additionally, the conjugation of the antibody, Trastuzumab, posed a variety of challenges. Trastuzumab is a large molecule with a molecular weight of 298.3 g/mol. Due to its large size and high molecular weight, a triple gel filtration chromatography column was used for the purification of the immunoliposomes. This led to the loss of lipid content in the final liposomal solution, as confirmed by results portrayed in Table 6. Since the lipid contents were lowered, the concentration of encapsulated DOX was also lowered, thus leading to inaccuracies during the release experiments.

#### **4.7 Kinetic Modeling**

The nine different drug release models (discussed in Section 3.7) were applied and plotted to the release data for all batches of liposomes at the three power densities

investigated. They were then linearized and the constant of determination ( $R^2$ ) values compared for each model. The model with an  $R^2$  value close to unity was taken to be the best fit model. For both control and immunoliposomes, the Baker-Lonsdale model was considered to be the best fit model. Table 12 provides all the  $R^2$  constants for all the plots of control liposomes, and Table 13 gives the  $R^2$  values for immunoliposomes. Figures 31 to 39 represent the nine models for one batch of Trastuzumab conjugated immunoliposomes at 7.46 mW/cm<sup>2</sup>. The remaining modeling figures for batch 1 of liposomes at all three power densities are archived in the Appendix.

Table 12:  $R^2$  values for control liposomes

$R^2$ values for control liposomes					
Power Density	Model	Batch 1	Batch 2	Batch 3	Average $R^2$
7.46 mW/cm <sup>2</sup>	Zero Order	0.989	0.995	0.988	0.991
	First Order	0.709	0.821	0.849	0.793
	Korsmeyer - Peppas	0.985	0.980	0.930	0.965
	Hixon-Crowell	0.987	0.997	0.935	0.973
	Higuchi	0.984	0.962	0.921	0.956
	Baker - Lonsdale	0.989	0.996	0.987	0.991
	Weibull	0.991	0.966	0.905	0.954
	Hopfenberg	0.997	0.987	0.935	0.973
	Gompertz	0.907	0.839	0.720	0.822
9.85 mW/cm <sup>2</sup>	Zero Order	0.991	0.991	0.974	0.985
	First Order	0.735	0.822	0.937	0.831
	Korsmeyer - Peppas	0.984	0.981	0.892	0.952
	Hixon-Crowell	0.997	0.980	0.882	0.953
	Higuchi	0.981	0.968	0.798	0.916
	Baker - Lonsdale	0.991	0.992	0.917	0.967
	Weibull	0.987	0.950	0.874	0.937
	Hopfenberg	0.997	0.980	0.882	0.953
	Gompertz	0.912	0.761	0.727	0.800
17.31 mW/cm <sup>2</sup>	Zero Order	0.987	0.959	0.986	0.977
	First Order	0.729	0.721	0.867	0.772
	Korsmeyer - Peppas	0.983	0.983	0.972	0.979
	Hixon-Crowell	0.995	0.989	0.908	0.964
	Higuchi	0.987	0.978	0.946	0.970
	Baker - Lonsdale	0.987	0.959	0.986	0.977
	Weibull	0.983	0.980	0.946	0.969
	Hopfenberg	0.882	0.989	0.946	0.939
	Gompertz	0.847	0.818	0.756	0.807

Table 13: R<sup>2</sup> values for immunoliposomes

R <sup>2</sup> values for control liposomes					
Power Density	Model	Batch 1	Batch 2	Batch 3	Average R <sup>2</sup>
7.46 mW/cm <sup>2</sup>	Zero Order	0.986	0.986	0.974	0.982
	First Order	0.819	0.779	0.893	0.830
	Korsmeyer - Peppas	0.956	0.944	0.927	0.942
	Hixon-Crowell	0.974	0.970	0.958	0.967
	Higuchi	0.952	0.949	0.936	0.946
	Baker - Lonsdale	0.986	0.986	0.974	0.982
	Weibull	0.944	0.940	0.893	0.926
	Hopfenberg	0.974	0.970	0.958	0.967
	Gompertz	0.829	0.836	0.763	0.809
9.85 mW/cm <sup>2</sup>	Zero Order	0.983	0.992	0.994	0.990
	First Order	0.795	0.836	0.791	0.807
	Korsmeyer - Peppas	0.981	0.960	0.985	0.975
	Hixon-Crowell	0.963	0.979	0.948	0.963
	Higuchi	0.960	0.958	0.967	0.962
	Baker - Lonsdale	0.983	0.992	0.994	0.990
	Weibull	0.954	0.943	0.952	0.950
	Hopfenberg	0.963	0.979	0.948	0.963
	Gompertz	0.750	0.819	0.692	0.754
17.31 mW/cm <sup>2</sup>	Zero Order	0.978	0.993	0.992	0.988
	First Order	0.893	0.827	0.832	0.850
	Korsmeyer - Peppas	0.898	0.966	0.964	0.943
	Hixon-Crowell	0.915	0.949	0.939	0.934
	Higuchi	0.932	0.964	0.958	0.951
	Baker - Lonsdale	0.978	0.993	0.992	0.988
	Weibull	0.843	0.929	0.926	0.899
	Hopfenberg	0.915	0.949	0.939	0.934
	Gompertz	0.633	0.706	0.701	0.680

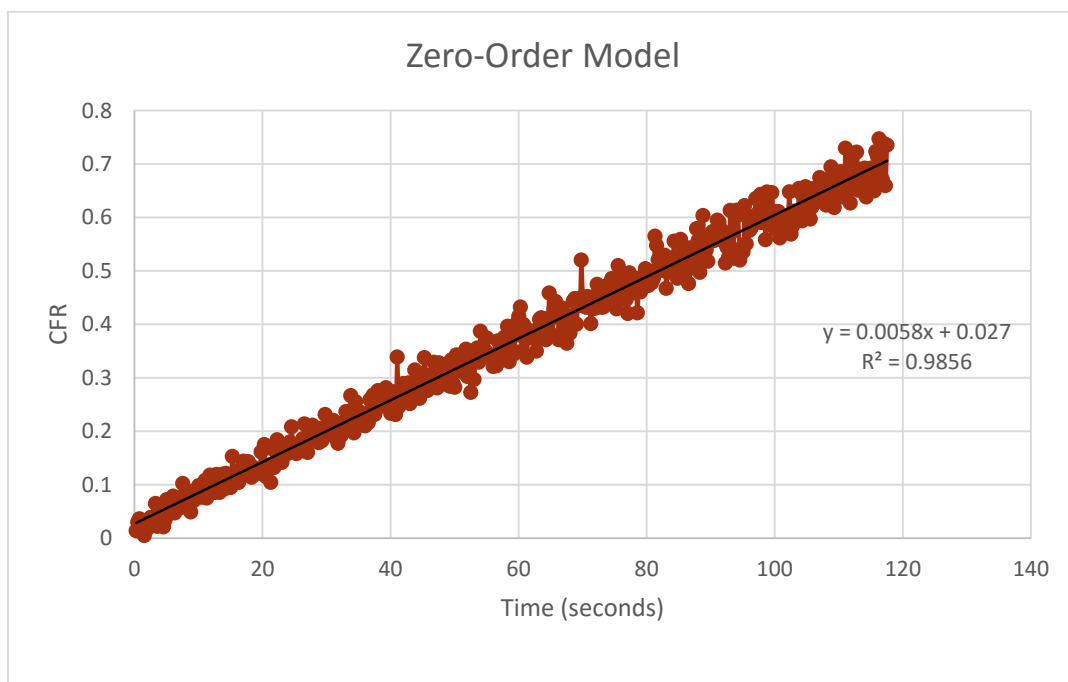


Figure 31: Zero-order model (CFR vs time) for immunoliposomes at 7.46 mW/cm<sup>2</sup> (Batch 1)

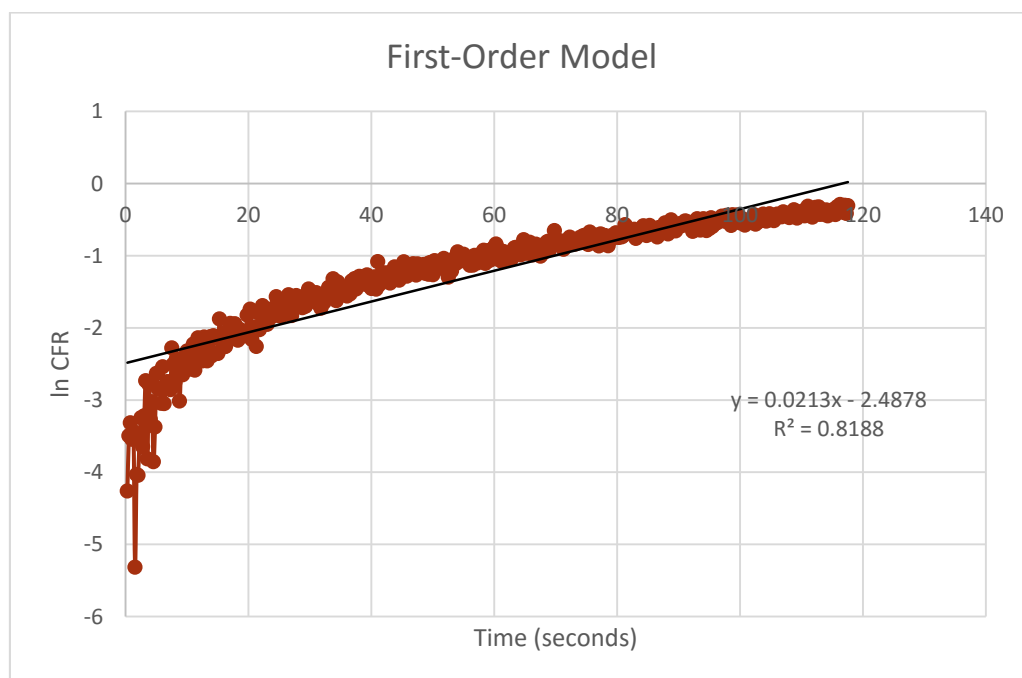


Figure 32: First order model (ln CFR vs time) for immunoliposomes at 7.46 mW/cm<sup>2</sup> (Batch 1)

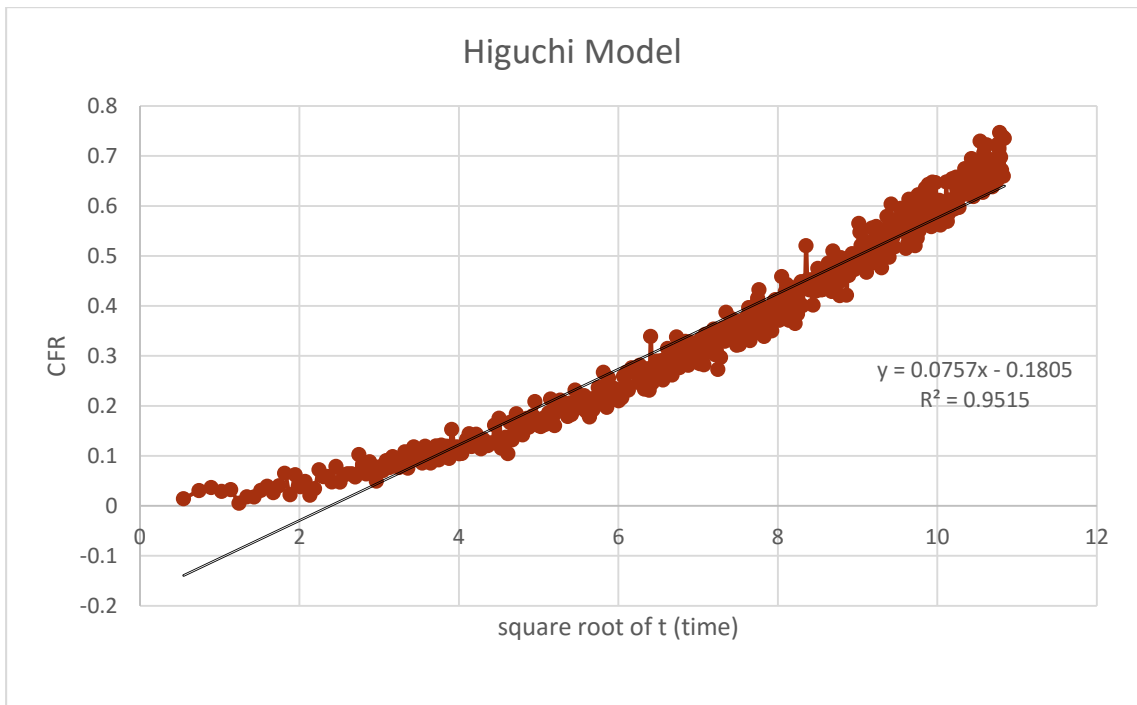


Figure 33: Higuchi model (CFR vs  $\sqrt{t}$ ) for immunoliposomes at 7.46 mW/cm<sup>2</sup> (Batch 1)

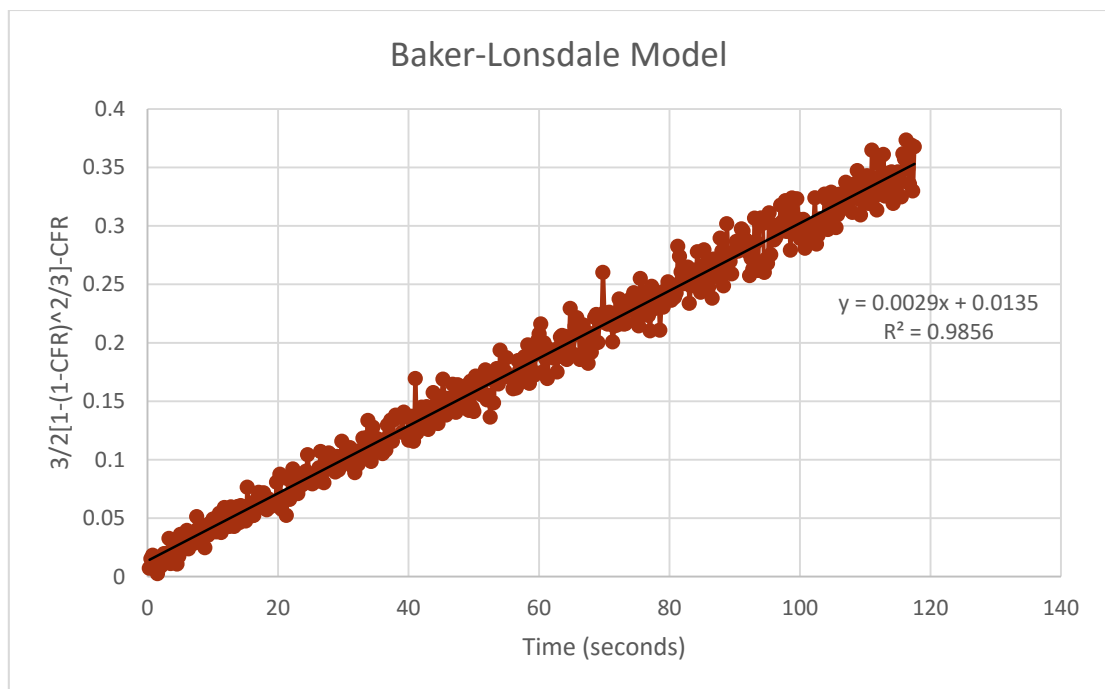


Figure 34: Baker Lonsdale model ( $\frac{3}{2}[1-(1-CFR)^2/3]-CFR$  vs time) for immunoliposomes at 7.46 mW/cm<sup>2</sup> (Batch 1)

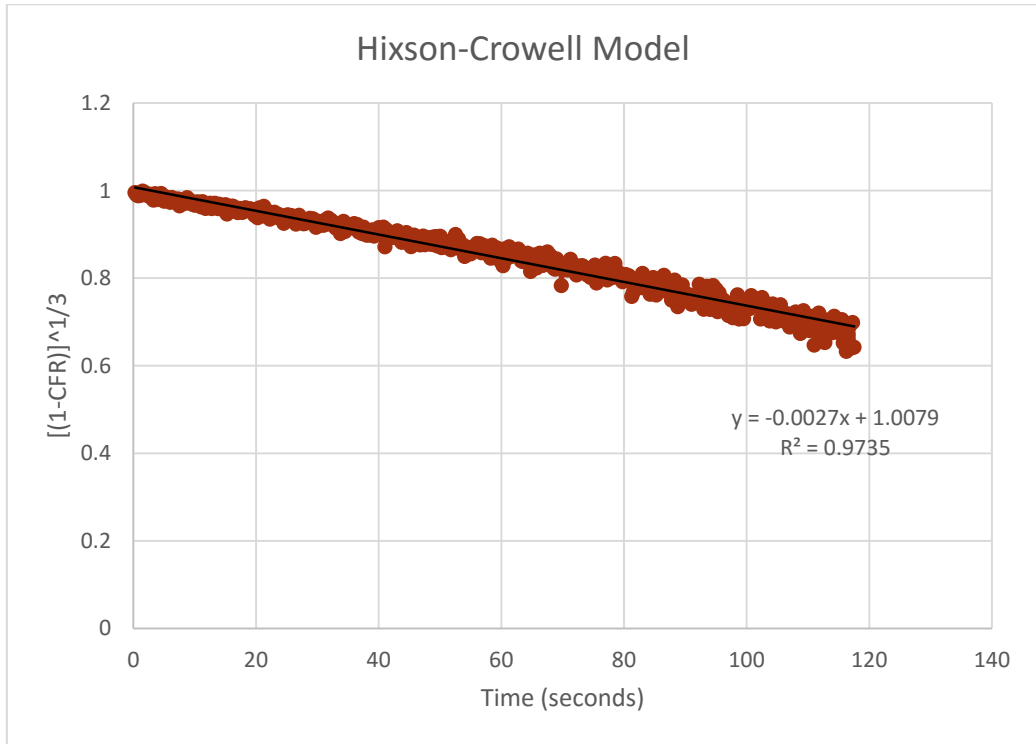


Figure 35: Hixson Crowell model ( $(1-CFR)^{1/3}$  vs time) for immunoliposomes at 7.46 mW/cm<sup>2</sup> (Batch 1)

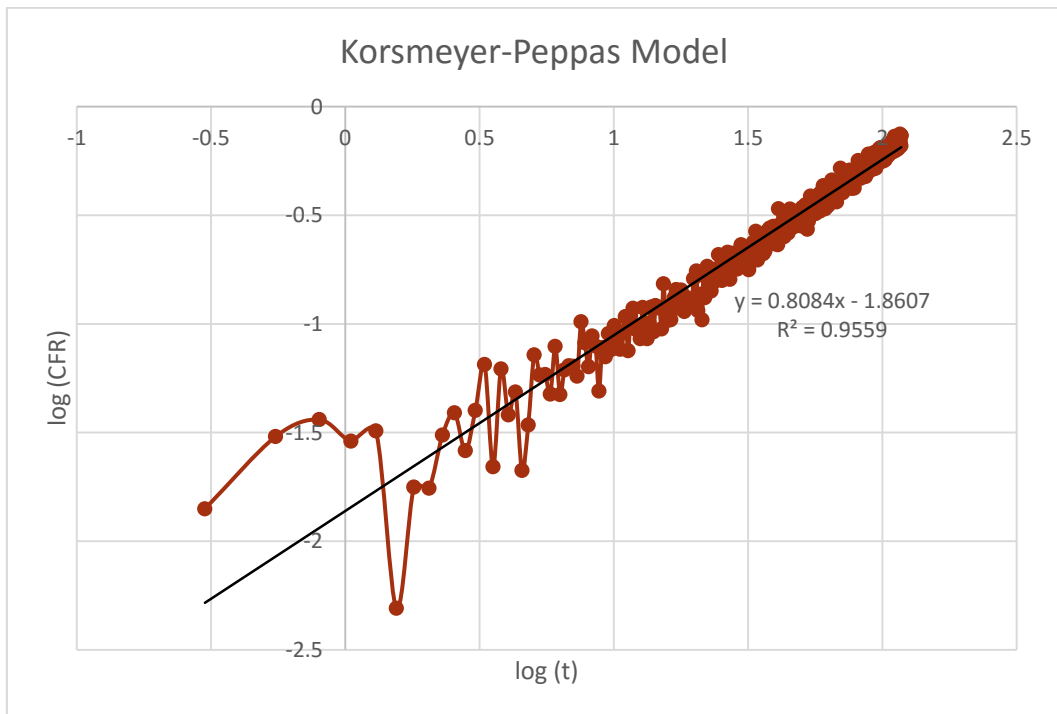


Figure 36: Korsmeyer Peppas (log CFR vs log time) model for immunoliposomes at 7.46 mW/cm<sup>2</sup> (Batch 1)

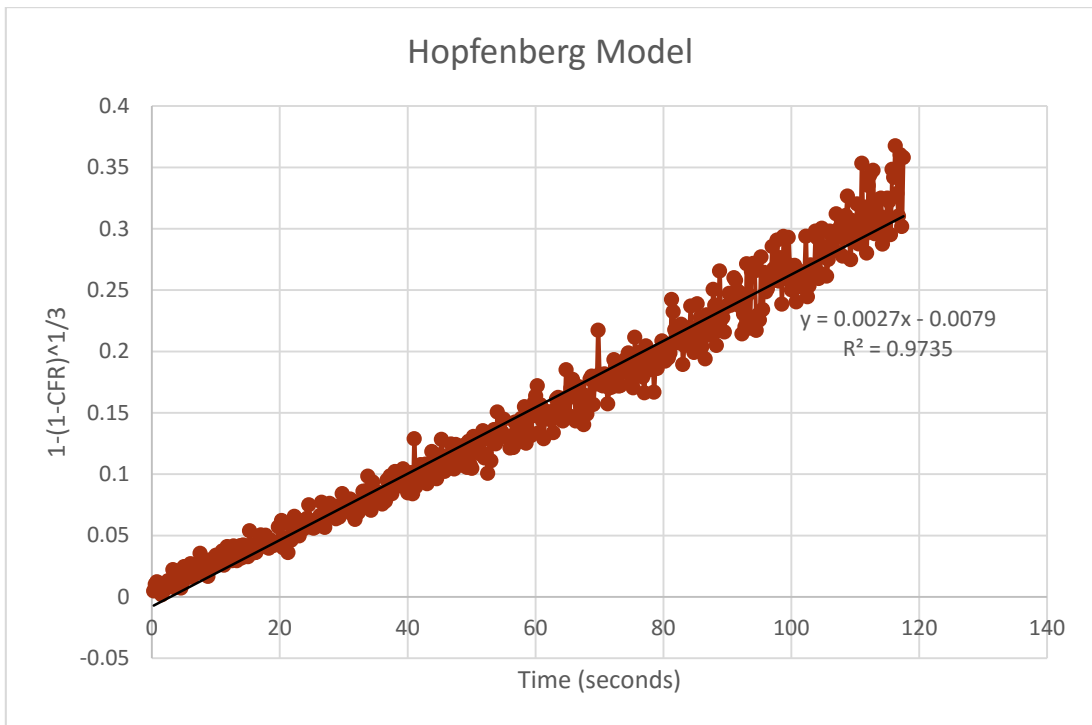


Figure 37: Hopfenberg model ( $1-(1-CFR)^{\frac{1}{3}}$  vs time) for immunoliposomes at 7.46 mW/cm<sup>2</sup> (Batch 1)

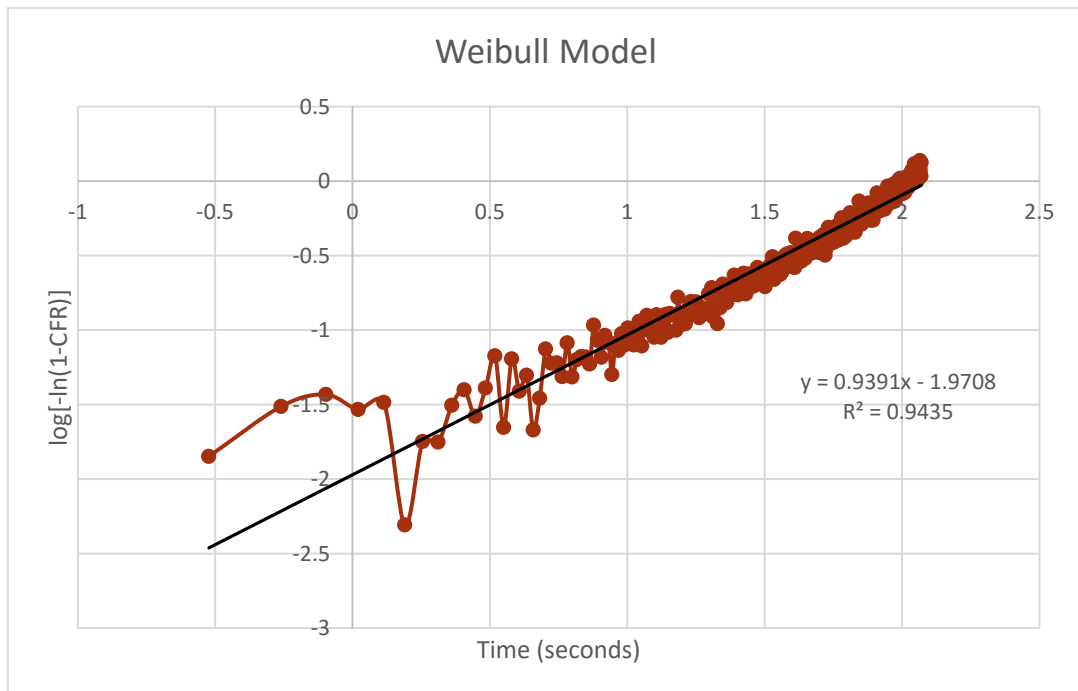


Figure 38: Weibull model ( $\log[-\ln(1-CFR)]$  vs time) for immunoliposomes at 7.46 mW/cm<sup>2</sup> (Batch 1)

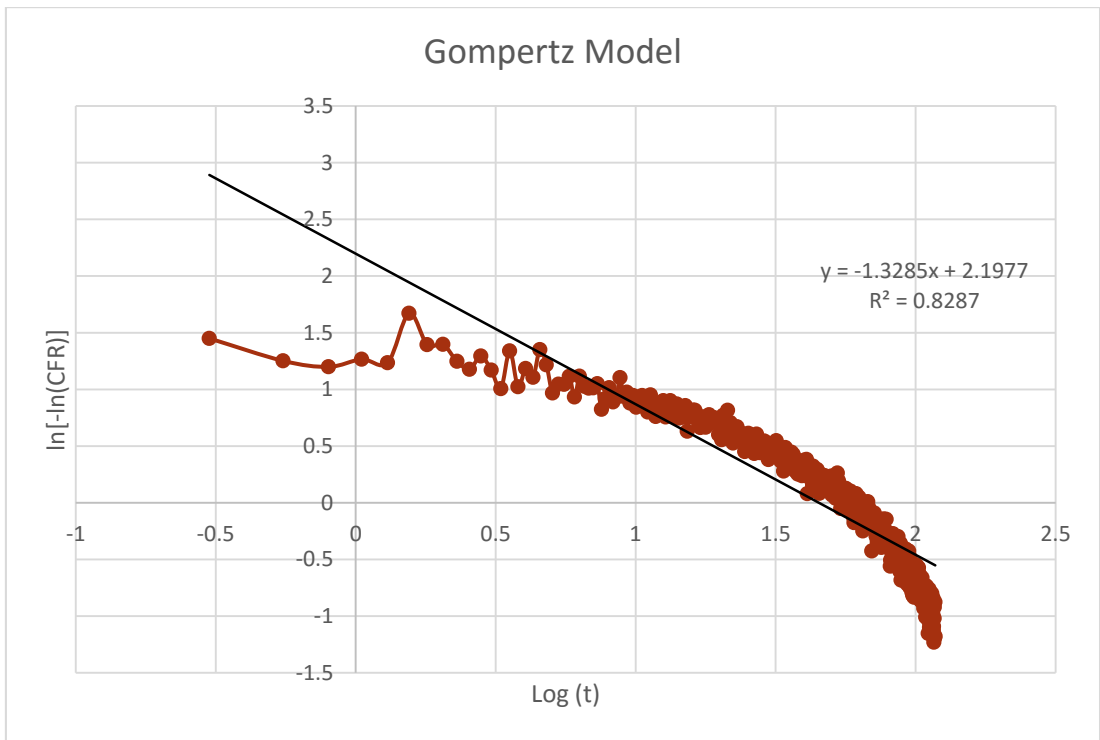


Figure 39: Gompertz model ( $\ln[-\ln(\text{CFR})]$  vs time) for immunoliposomes at 7.46  $\text{mW}/\text{cm}^2$  (Batch 1)

#### 4.8 Statistical Analysis for Best Fit Model – Baker Lonsdale Model

The Baker-Lonsdale model provided the best fit with the  $R^2$  average value being 0.9907667, 0.9668667, and 0.9771667 for each of the increasing power densities for control liposomes; and 0.9819667, 0.9897333, 0.9876667 for the immunoliposomes. The Baker Lonsdale plot is constructed by plotting  $\frac{3}{2}[1 - (1 - \text{CFR})^{2/3}] - \text{CFR}$  vs. time (in seconds) and is commonly used to understand the release from microspheres or microcapsules. The zero-order model comes very close to Baker-Lonsdale's fit model with high values of the coefficients of determination. The zero-order model is the simplest investigated model and hence is preferred over more complicated models. The DOX release profile slopes in Figures 20 and 23 further prove the validity of the zero-order model in this project.

The release constants were determined for the Baker-Lonsdale model for each batch of control liposomes and immunoliposomes at each of the power densities: 7.46, 9.85, and 17.31  $\text{mW}/\text{cm}^2$  and are summarized in Table 14.



Table 14: Release constants for Baker Lonsdale model for control liposomes and immunoliposomes at three different power densities

	Release constants from Baker Lonsdale model		
	Power Densities		
Liposome Batch	7.46 mW/cm <sup>2</sup>	9.85 mW/cm <sup>2</sup>	17.31 mW/cm <sup>2</sup>
Control Batch 1	0.00290	0.00340	0.00360
Control Batch 2	0.00310	0.00410	0.00420
Control Batch 3	0.00370	0.00220	0.00370
Average	<b>0.00323</b>	<b>0.00323</b>	<b>0.00383</b>
Standard Deviation	<b>0.00042</b>	<b>0.00096</b>	<b>0.00032</b>
Immunoliposome Batch 1	0.00290	0.00420	0.00660
Immunoliposome Batch 2	0.00290	0.00300	0.00390
Immunoliposome Batch 3	0.00320	0.00400	0.00400
Average	<b>0.00300</b>	<b>0.00373</b>	<b>0.00483</b>
Standard Deviation	<b>0.00017</b>	<b>0.00064</b>	<b>0.00153</b>

These constants were compared using an ANOVA two way analysis of variance program. ANOVA helps detect a correlation between two independent variables and a dependent variable. In this thesis, the independent variables are the power density of ultrasound and the type of liposome. The dependent variable is the release constant calculated using the Baker Lonsdale model. Three null hypotheses were postulated for this test: First, no difference in release constant exists between control liposomes and immunoliposomes. Second, the US power densities affect the value of the release constants. Lastly, acoustic power density and nanocarrier types are independent of each other. The criteria for the p-value were set to be less than 0.05, which means the confidence level would be 0.95. Table 15 shows the ANOVA test results obtained for the model. For the first hypothesis, the F value (1.207) is smaller than F critical (4.745), while the p-value (0.293) is greater than 0.05. This means that the null hypothesis cannot be rejected, and the type of liposome does not affect the release constant. The

same case applies to the second null hypothesis, where the F value (3.517) is smaller than F critical (3.885), and the p-value (0.062) is greater than 0.05. This means that k values are not affected by US power density. Lastly, the F value (0.869) is smaller than F critical value (3.885) and p-value (0.444) is greater than 0.05. This concludes that the acoustic power density and type of liposomes are independent of each other.

Table 15: Two factor ANOVA test for release constants

ANOVA Test for Baker Lonsdale Model						
<i>Source of Variation</i>	<i>SS</i>	<i>df</i>	<i>MS</i>	<i>F</i>	<i>P-value</i>	<i>F crit</i>
Sample	$8.0222 \times 10^{-7}$	1	$8.02222 \times 10^{-7}$	1.207	0.293	4.745
Columns	$4.674 \times 10^{-6}$	2	$2.3372 \times 10^{-6}$	3.517	0.062	3.885
Interaction	$1.1544 \times 10^{-6}$	2	$5.77222 \times 10^{-7}$	0.869	0.444	3.885
Within	$7.9733 \times 10^{-6}$	12	$6.6444 \times 10^{-7}$			
Total	$1.4604 \times 10^{-4}$	17				

## Chapter 5. Conclusion and Future Work

The number of cancer cases is on the rise, and many are dying from this deadly disease on a daily basis. Chemotherapy is the most common form of treatment. However, this treatment modality is plagued by dozens of side effects, including cardiotoxicity, anemia, nausea, fatigue, etc. Scientists are continually working to develop novel drug delivery techniques to safely deliver these chemotherapeutic agents to the disease site preferentially and to help patients combat the side effects of systemic chemotherapy. This thesis is an example of a drug delivery platform used in cancer treatment.

In this research, nanocarriers (i.e., liposomes) composed of lipids were synthesized to deliver the chemotherapeutic drug, Doxorubicin. The liposomes were conjugated with the Trastuzumab moiety to target the overexpressed HER2 receptors on breast cancer cells utilizing receptor-mediated endocytosis. Trastuzumab is a monoclonal antibody and is approved by the FDA for the treatment of cancer under the trademark name, Herceptin. The size of the liposomes, lipid content, and protein content was determined after synthesis using dynamic light scattering analysis (DLS), the Stewart Assay, and the BCA Assay. The drug was then released by exposing the liposomes to low-frequency of ultrasound at three different power densities using a 20-kHz transducer, and the release profiles were studied in depth. The pulse wise release was also studied, and comparisons were drawn between the control liposomes and immunoliposomes. Experimental results showed that the trastuzumab conjugated immunoliposomes successfully released the drug at a desirable rate and can be developed into a novel drug delivery systems. The release data were also used to deduce the kinetics of this system, and the Baker-Lonsdale model appeared to give the best fit to the data. Statistical analysis was then carried out using the release constants to what affects the release kinetics of this acoustic therapeutic technique.

The next step would be to carry out high-frequency ultrasound (HFUS) release to understand the release kinetics and profiles obtained. This is followed by *in vitro* studies where Trastuzumab conjugated liposomes could be delivered to a cancer cell line overexpressing HER receptors. If the *in vitro* results are positive, *in vivo* experiments could follow. This project is just in the first step of developing a new drug

delivery system, and hopefully, one day, this drug delivery platform will be used to safely deliver chemotherapeutic drugs to cancer patients, while at the same time reducing the excruciating side effect of conventional systemic chemotherapy.

## References

- [1] “Breast Cancer Statistics,” *World Cancer Research Fund*, 2018 [Online]. Available: <https://www.wcrf.org/dietandcancer/cancer-trends/breast-cancer-statistics>. [Accessed: 04-Mar-2019].
- [2] A. A. Zain, “Over 4,500 new cancer cases in UAE this year,” *Khaleej Times*, 2018. [Online]. Available: <https://www.khaleejtimes.com/news/uae-health/over-4500-new-cancer-cases-in-uae-this-year>. [Accessed: 04-Mar-2019].
- [3] S. Elmore, “Apoptosis: A Review of Programmed Cell Death,” *Toxicologic Pathology*, vol.35, no. 4, pp. 495-516, 2007.
- [4] “What is cancer?,” *National Breast Cancer Foundation*, 2019. [Online]. Available: <https://www.nationalbreastcancer.org/what-is-cancer/>. [Accessed: 06-Jan-2020].
- [5] “Understanding Cancer,” *National Cancer Institute*, 2015. [Online]. Available: <https://www.cancer.gov/about-cancer/understanding/what-is-cancer>. [Accessed: 06-Jan-2020].
- [6] “Cancer Statistics,” *National Cancer Institute*, 2018. [Online]. Available: <https://www.cancer.gov/about-cancer/understanding/statistics>. [Accessed: 06-Jan-2020].
- [7] A. Ficai and A. M. Grumezescu, “Chapter 1 - Nanotechnology for personalized medicine: cancer research, diagnosis and therapy,” in *Nanostructures for cancer therapy*. Elsevier, 2017, pp. 23 - 35.
- [8] “ATSDR - Cancer policy framework,” *Agency for Toxic substances and Disease Registry*, 2001. [Online]. Available: <https://www.atsdr.cdc.gov/cancer.html>. [Accessed: 06-Jan-2020].
- [9] C. C. Harris, “p53 tumor suppressor gene: From the basic research laboratory to the clinic - An abridged historical perspective,” *Carcinogenesis*, vol. 17, no. 6, pp. 1187-1198, June 1996.
- [10] “Cancer Treatment,” *National Cancer Institute*, 2019. [Online]. Available: <https://www.cancer.gov/about-cancer/treatment>. [Accessed: 06-Jan-2020].
- [11] “The Chemotherapy Source Book,” *Ann. Intern. Med.*, vol. 117, no. 5, pp. 448, 1992.
- [12] S. N. Khleif, O. Rixe, and R. Skeel, *Skeel’s Handbook of Cancer Therapy*, Lippincott Williams & Wilkins, 2016, pp. 206.
- [13] M. A. Dicato and E. Van Cutsem, “Chapter 1 - Drug interactions and pharmacogenetics,” *Side effects of medical cancer therapy: Prevention and treatment: Second edition*, 2018, pp. 1-19.
- [14] “World cancer data,” *World Cancer Research Fund International*, 2007. [Online]. Available: <https://www.wcrf.org/dietandcancer/cancer-trends/worldwide-cancer-data>. [Accessed: 08-Jan-2020].

- [15] E. L. Davies, "Breast Cancer," *Medicine (Baltimore)*, vol. 40, no. 1, pp. 5–9, 2012.
- [16] Y. Gökmen-Polar and S. Badve, "Breast cancer prognostic markers: an overview of a changing menu," *MLO. Med. Lab. Obs.*, vol. 47, no. 10, pp. 8-14, 2015.
- [17] M. Amin *et al.*, "Specific delivery of idarubicin to HER2-positive breast cancerous cell line by trastuzumab-conjugated liposomes," *J. Drug Deliv. Sci. Technol.*, vol. 47, pp. 209-214, 2018.
- [18] M. Uriarte-Pinto, Á. Escolano-Pueyo, V. Gimeno-Ballester, O. Pascual-Martínez, M. R. Abad-Sazatornil, and M. J. Agustín-Ferrández, "Trastuzumab, non-pegylated liposomal-encapsulated doxorubicin and paclitaxel in the neoadjuvant setting of HER-2 positive breast cancer," *Int. J. Clin. Pharm.*, vol. 38, no. 2, pp. 446–453, 2016.
- [19] "Breast Cancer Facts and Figures 2019-2020," *American Cancer Society*, 2019. [Online]. Available: <https://www.cancer.org/content/dam/cancer-org/research/cancer-facts-and-statistics/breast-cancer-facts-and-figures/breast-cancer-facts-and-figures-2019-2020.pdf>. [Accessed: 24-Jan-2020].
- [20] A. M. Holban and A. M. Grumezescu, "Part 1 - Smart Delivery, " *Nanoarchitectonics for Smart Delivery and Drug Targeting*, Elsevier, 2016, pp. 3-34.
- [21] D. Liu, F. Yang, F. Xiong, and N. Gu, "The smart drug delivery system and its clinical potential," *Theranostics*, vol. 6, no. 9, pp. 1306 - 1323, 2016.
- [22] R. I. Nicholson, J. M. W. Gee, and M. E. Harper, "EGFR and cancer prognosis," *Eur. J. Cancer*, vol. 37, no. 4, pp. 9-15, 2001.
- [23] M. K. Riaz *et al.*, "Surface functionalization and targeting strategies of liposomes in solid tumor therapy: A review," *International Journal of Molecular Sciences*, vol. 19, no.195, pp. 1-27, 2018.
- [24] M. Karimi *et al.*, "Smart micro/nanoparticles in stimulus-responsive drug/gene delivery systems," *Chemical Society Reviews*, vol. 45, no.5, pp. 1457 - 1501, 2016.
- [25] X. Guo, Y. Cheng, X. Zhao, Y. Luo, J. Chen, and W. E. Yuan, "Advances in redox-responsive drug delivery systems of tumor microenvironment," *Journal of Nanobiotechnology*, vol. 16, no.74, pp.1-10, 2018.
- [26] Y. L. Liu, D. Chen, P. Shang, and D. C. Yin, "A review of magnet systems for targeted drug delivery," *Journal of Controlled Release*, vol.302, pp. 90-104, 2019.
- [27] R. Keservani and A. Sharma, *Nanoconjugate Nanocarriers for Drug Delivery*. Palm Bay, FL: Apple Academic Press, 2018, pp. 45 - 78.
- [28] M. A. Elkhodiry, G. A. Husseini, and D. Velluto, "Targeting the Folate Receptor: Effects of Conjugating Folic Acid to DOX Loaded Polymeric Micelles," *Anticancer. Agents Med. Chem.*, vol. 16, no.10, pp. 1275-1280, 2016.

- [29] G. A. Hussein, D. Velluto, L. Kherbeck, W. G. Pitt, J. A. Hubbell, and D. A. Christensen, "Investigating the acoustic release of doxorubicin from targeted micelles," *Colloids Surfaces B Biointerfaces*, vol. 101, pp. 153-155, 2013.
- [30] P. Juzenas *et al.*, "Quantum dots and nanoparticles for photodynamic and radiation therapies of cancer," *Advanced Drug Delivery Reviews*, vol. 60, no. 15, pp. 1600-1614, 2008.
- [31] A. Bianco, K. Kostarelos, and M. Prato, "Applications of carbon nanotubes in drug delivery," *Current Opinion in Chemical Biology*, vol. 9, no. 6, pp. 674-679, 2005.
- [32] P. Ghosh, G. Han, M. De, C. K. Kim, and V. M. Rotello, "Gold nanoparticles in delivery applications," *Advanced Drug Delivery Reviews*, vol. 60, no. 11, pp. 1307-1315, 2008.
- [33] R. Bhattacharya and P. Mukherjee, "Biological properties of 'naked' metal nanoparticles," *Advanced Drug Delivery Reviews*, vol. 60, no. 11, pp. 1289-1306, 2008.
- [34] T. Patel, J. Zhou, J. M. Piepmeier, and W. M. Saltzman, "Polymeric nanoparticles for drug delivery to the central nervous system," *Advanced Drug Delivery Reviews*, vol. 64, no. 7, pp. 701-705, 2012.
- [35] N. S. Awad *et al.*, "Effect of Pegylation and Targeting Moieties on the Ultrasound-Mediated Drug Release from Liposomes," *ACS Biomater. Sci. Eng.*, vol. 6, no. 1, pp. 48-57, 2020.
- [36] N. M. Salkho *et al.*, "Ultrasonically controlled estrone-modified liposomes for estrogen-positive breast cancer therapy," *Artif. Cells, Nanomedicine Biotechnol.*, vol. 46, no. 2, pp. 462-472, 2018.
- [37] M. Ibrahim, R. Sabouni, and G. A. Hussein, "Synthesis of Metal-Organic Framework from Iron Nitrate and 2,6-Naphthalenedicarboxylic Acid and Its Application as Drug Carrier," *J. Nanosci. Nanotechnol.*, vol. 18, no. 8, pp. 5266-5273, 2018.
- [38] M. Ibrahim, R. Sabouni, and G. Hussein, "Anti-cancer Drug Delivery Using Metal Organic Frameworks (MOFs)," *Curr. Med. Chem.*, vol. 24, no. 2, pp. 193-214, 2016.
- [39] J. Fang, H. Nakamura, and H. Maeda, "The EPR effect: Unique features of tumor blood vessels for drug delivery, factors involved, and limitations and augmentation of the effect," *Advanced Drug Delivery Reviews*, vol. 63, no. 3, pp. 136-151, 2011.
- [40] E. Cukierman and D. R. Khan, "The benefits and challenges associated with the use of drug delivery systems in cancer therapy," *Biochemical Pharmacology*, vol. 80, no. 5, pp. 762-770, 2010.
- [41] A. K. Iyer, G. Khaled, J. Fang, and H. Maeda, "Exploiting the enhanced permeability and retention effect for tumor targeting," *Drug Discovery Today*, vol. 11, no. 17, pp. 812-818, 2006.

- [42] A. M. Jhaveri and V. P. Torchilin, “Multifunctional polymeric micelles for delivery of drugs and siRNA,” *Frontiers in Pharmacology*, vol. 5, no. 77, 2014.
- [43] E. Ruoslahti, “RGD and other recognition sequences for integrins,” *Annu. Rev. Cell Dev. Biol.*, vol. 12, pp. 697-715, 1996.
- [44] K. Cho, X. Wang, S. Nie, Z. Chen, and D. M. Shin, “Therapeutic nanoparticles for drug delivery in cancer,” *Clinical Cancer Research*, vol. 14, no. 5, pp. 1310-1316, 2008.
- [45] H. S. Yoo and T. G. Park, “Folate receptor targeted biodegradable polymeric doxorubicin micelles,” *J. Control. Release*, vol. 96, no. 2, pp. 273-283, 2004.
- [46] A. M. Fowler and E. T. Alarid, “Amping up estrogen receptors in breast cancer,” *Breast Cancer Res.*, vol. 9, no.4, pp.305, 2007.
- [47] J. O. Eloy, R. Petrilli, L. N. F. Trevizan, and M. Chorilli, “Immunoliposomes: A review on functionalization strategies and targets for drug delivery,” *Colloids and Surfaces B: Biointerfaces*, vol. 159, pp. 454-467, 2017.
- [48] D. J. Slamon *et al.*, “Use of chemotherapy plus a monoclonal antibody against her2 for metastatic breast cancer that overexpresses HER2,” *N. Engl. J. Med.*, \ vol. 344, no. 11, pp. 783-792, 2001.
- [49] “Trastuzumab,” *Chemical Book*, 2017. [Online]. Available: [https://www.chemicalbook.com/ProductChemicalPropertiesCB61074602\\_EN.html](https://www.chemicalbook.com/ProductChemicalPropertiesCB61074602_EN.html). [Accessed: 09-Feb-2020].
- [50] “Herceptin,” *Genentech*, 2020. [Online]. Available: <https://www.herceptin.com/hcp/treating-HER2-cancer.html>. [Accesseed: 09-Feb-2020].
- [51] O. Penate Medina *et al.*, “Liposomal Tumor Targeting in Drug Delivery Utilizing MMP-2- and MMP-9-Binding Ligands,” *J. Drug Deliv.*, vol. 2011, pp. 1-9, 2011.
- [52] H. D. Seema Rohilla, Chanchal Chauhan, Ravi Singh, Ankur Rohilla, Dinesh Kaushik, Satish Sardana, “Liposomes: Preparations and Applications,” *Int. J. Drug Dev. Res.*, vol. 4, pp. 108–115, 2012.
- [53] A. Schroeder, J. Kost, and Y. Barenholz, “Ultrasound, liposomes, and drug delivery: principles for using ultrasound to control the release of drugs from liposomes,” *Chemistry and Physics of Lipids*, vol. 162, no. 1, pp. 1-16, 2009.
- [54] D. Lembo and R. Cavalli, “Nanoparticulate delivery systems for antiviral drugs,” *Antiviral Chemistry and Chemotherapy*, vol. 21, pp. 53-70, 2010.
- [55] N. Monteiro, A. Martins, R. L. Reis, and N. M. Neves, “Liposomes in tissue engineering and regenerative medicine,” *Journal of the Royal Society Interface*, vol. 11, no. 101, pp. 9-24, 2014.
- [56] “What is the Transition Temperature of the Lipid?,” *Avanti Polar Lipids, Inc*, 2019. [Online]. Available: <https://avantilipids.com/tech-support/faqs/transition-temperature>. [Accessed: 18-Feb-2020].



- [57] A. A. Gabizon, H. Shmeeda, and S. Zalipsky, "Pros and cons of the liposome platform in cancer drug targeting," *Journal of Liposome Research*, vol. 16, no. 3, pp. 175-183, 2006.
- [58] U. Bulbake, S. Doppalapudi, N. Kommineni, and W. Khan, "Liposomal formulations in clinical use: An updated review," *Pharmaceutics*, vol. 9, no. 2, pp. 12, 2017.
- [59] G. A. Hussein, W. G. Pitt, and M. Javadi, "Investigating the stability of liposomes at elevated temperatures," *Technol. Cancer Res. Treat.*, vol. 14, no. 4, pp. 379-382, 2015.
- [60] H. Zhang. "Thin film hydration followed by extrusion method for liposome preparation," in *Liposomes*, 2<sup>nd</sup> ed., vol. 1522. G. D'Souza, New York: Humana Press, 2017, pp. 17-22.
- [61] A. Akbarzadeh, R. Rezaei-sadabady, S. Davaran, S. W. Joo, and N. Zarghami, "Liposome : classification , preparation , and applications," *Nanoscale Res. Lett.*, vol. 8. no. 1, pp. 1–10, 2013.
- [62] Z. Huang *et al.*, "Progress involving new techniques for liposome preparation," *Asian Journal of Pharmaceutical Sciences*, vol. 9, no. 4, pp. 176-182, 2014.
- [63] R. Gharib, H. Greige-Gerges, S. Fourmentin, C. Charcosset, and L. Auezova, "Liposomes incorporating cyclodextrin-drug inclusion complexes: Current state of knowledge," *Carbohydrate Polymers*, vol. 129, pp. 175-186, 2015.
- [64] D. Luo *et al.*, "Doxorubicin encapsulated in stealth liposomes conferred with light-triggered drug release," *Biomaterials*, vol. 75, pp. 193-202, 2016.
- [65] G. Pasut *et al.*, "Polyethylene glycol (PEG)-dendron phospholipids as innovative constructs for the preparation of super stealth liposomes for anticancer therapy," *J. Control. Release*, vol. 199, pp. 106-113, 2015.
- [66] K. Kristensen, T. B. Engel, A. Stensballe, J. B. Simonsen, and T. L. Andresen, "The hard protein corona of stealth liposomes is sparse," *J. Control. Release*, vol. 307, pp. 1-15, 2019.
- [67] G. Bendas, "Immunoliposomes: A promising approach to targeting cancer therapy," *BioDrugs*, vol. 15, no. 4, pp. 215-224, 2001.
- [68] P. G.L., "Pegylated liposomal doxorubicin: A review of its use in the treatment of relapsed or refractory multiple myeloma," *Drugs*, vol. 68, no. 17, pp. 2535-2551, 2008.
- [69] Y. Barenholz, "Doxil® - The first FDA-approved nano-drug: Lessons learned," *Journal of Controlled Release*, vol. 3, no. 3, pp. 2508-2517, 2012.
- [70] S. A. Engelberth, N. Hempel, and M. Bergkvist, "Development of nanoscale approaches for ovarian cancer therapeutics and diagnostics," *Crit. Rev. Oncog.*, vol. 19, no. 3-4, pp. 281-316, 2014.
- [71] L. M. Russell, M. Hultz, and P. C. Searson, "Leakage kinetics of the liposomal chemotherapeutic agent Doxil: The role of dissolution, protonation, and passive

- transport, and implications for mechanism of action,” *J. Control. Release*, vol. 269, pp. 171-176, 2018.
- [72] T. Y. Wu, N. Guo, C. Y. Teh, and J. X. W. Hay, “Theory and fundamentals of ultrasound,” in *Advances in Ultrasound Technology for Environmental Remediation*, 1<sup>st</sup> ed., Netherlands: Springer, 2013, pp. 5-12.
- [73] D. Maulik and I. Zalud, “Physical principles of Doppler Ultrasonography,” in *Doppler ultrasound in Obstetrics and Gynecology*, 2<sup>nd</sup> ed., Heidelberg, Berlin: Springer-Verlag, 2005, pp. 9-17.
- [74] R. Chaudhuri, “The Doppler Effect,” in *Waves and Oscillations*, 2<sup>nd</sup> ed., Santiniketan, West Bengal: New Age International Limited Publishers, 2010, pp. 241-257.
- [75] “Ultrasound,” *RadiologyInfo.org*, 2018. [Online]. Available: [www.radiologyinfo.org/en/info.cfm?pg=genus](http://www.radiologyinfo.org/en/info.cfm?pg=genus). [Accessed: 25-Feb-2020]
- [76] P. Fulgham, “Physical principles of ultrasound,” in *Practical Urological Ultrasound*, 1<sup>st</sup> ed., vol. 12. B.Gilbert, New York: Humana Press, 2013, pp. 9-26.
- [77] S. Sen, *Acoustics Waves and Oscillations*. Santiniketan, West Bengal: New Age International Limited Publishers, 1990.
- [78] G. Kossoff, “Basic physics and imaging characteristics of ultrasound,” *World Journal of Surgery*, vol. 24, no. 2, pp. 134-142, 2000.
- [79] “Characteristics of Ultrasound,” *Ultrasound for Regional Anesthesia (USRA)*. [Online]. Available: <http://www.usra.ca/regional-anesthesia/introduction/basic.php>. [Accessed: 21-Feb-2020].
- [80] K. Tachibana S. Tachibana. “Emerging technologies using ultrasound for drug delivery,” in *Emerging therapeutic ultrasound*, 1<sup>st</sup> ed. J. Wu and W. Nyborg, VT, USA: World Scientific, 2006, pp. 131-166.
- [81] J. Connor, M. B. Yatvin, and L. Huang, “pH-sensitive liposomes: Acid-induced liposome fusion,” *Proc. Natl. Acad. Sci. U. S. A.*, vol. 81, no. 6, pp. 1715-1718, 1984.
- [82] G. R. Anyarambhatla and D. Needham, “Enhancement of the phase transition permeability of DPPC liposomes by incorporation of MPPC: A new temperature-sensitive liposome for use with mild hyperthermia,” *J. Liposome Res.*, vol. 9, no. 4, pp. 491-506, 1999.
- [83] O. V. Gerasimov, J. A. Boomer, M. M. Qualls, and D. H. Thompson, “Cytosolic drug delivery using pH- and light-sensitive liposomes,” *Adv. Drug Deliv. Rev.*, vol. 38, no. 3, pp. 317-338, 1999.
- [84] Y. L. Pang, A. Z. Abdullah, and S. Bhatia, “Review on sonochemical methods in the presence of catalysts and chemical additives for treatment of organic pollutants in wastewater,” *Desalination*, vol. 277, no. 1-3, pp. 1-14, 2011.
- [85] D. H. Shin, M. J. Koo, J. S. Kim, and J. S. Kim, “Herceptin-conjugated

- temperature-sensitive immunoliposomes encapsulating gemcitabine for breast cancer,” *Arch. Pharm. Res.*, vol. 39, no. 3, pp. 350-358, 2016.
- [86] G. T. Colbern, A. J. Hiller, R. S. Musterer, P. K. Working, and I. C. Henderson, “Antitumor activity of Herceptin® in combination with Stealth® liposomal cisplatin or nonliposomal cisplatin in a HER2 positive human breast cancer model,” *J. Inorg. Biochem.*, vol. 77, no. 1-2, pp. 117-120, 1999.
- [87] N. Mohammad, “Acoustically activated release of estrone-targeted liposomes used for breast cancer treatment,” M.S. Thesis, College of Engineering, American University of Sharjah, Sharjah, 2016.
- [88] P. Kawak, “Ultrasound triggered release of estrone-targeted liposomes,” M.S. Thesis, College of Engineering, American University of Sharjah, Sharjah, 2017.
- [89] A. Farooq, “Doxorubicin-encapsulated albumin liposomes with acousting triggering for cancer treatment,” M.S. Thesis, College of Engineering, American University of Sharjah, Sharjah, 2019.
- [90] N. AlSawaftah, “The use of transferrin and ultrasound in cancer treatment,” M.S. Thesis, College of Engineering, American University of Sharjah, Sharjah, 2019.
- [91] M. Mahmoud, “The effect of ultrasound on the drug delivery of RGD-targeted liposomes,” M.S. Thesis, College of Engineering, American University of Sharjah, Sharjah, 2018.
- [92] “16:0 PC (DPPC),” *Avanti Polar Lipids, Inc*, 2020. [Online]. Available: <https://avantilipids.com/product/850355>. [Accessed: 13-Feb-2020].
- [93] “DSPE-PEG(2000)Amine,” *Avanti Polar Lipids, Inc*, 2020. [Online]. Available: <https://avantilipids.com/product/880128>. [Accessed: 13-Feb-2020].
- [94] Sigma-Aldrich, “Cholesterol,” 2020. [Online]. Available: <https://www.sigmaaldrich.com/catalog/product/sigma/c8667?lang=en&region=AE>. [Accessed: 13-Feb-2020].
- [95] “Doxorubicin,” *U.S National Library of Medicine*, 2020. [Online]. Available: <https://pubchem.ncbi.nlm.nih.gov/compound/Doxorubicin>. [Accessed: 13-Feb-2020].
- [96] “The principles of dynamic light scattering GmbH,” *Anton Paar*, 2020. [Online]. Available: <https://wiki.anton-paar.com/en/the-principles-of-dynamic-light-scattering/>. [Accessed: 13-Feb-2020].
- [97] “The Stewart Assay,” *Liposome: Encapsula’s Scientific Blog*. [Online]. Available: <http://www.liposomes.org/2009/01/stewart-assay.html>. [Accessed: 17-Feb-2020].
- [98] “Pierce BCA Protein Assay Kit,” *ThermoFisher Scientific*. [Online]. Available: <https://www.thermofisher.com/order/catalog/product/23225#/23225>. [Accessed: 17-Feb-2020].

- [99] X. Dai, Z. Yue, M. E. Eccleston, J. Swartling, N. K. H. Slater, and C. F. Kaminski, "Fluorescence intensity and lifetime imaging of free and micellar-encapsulated doxorubicin in living cells," *Nanomedicine Nanotechnology, Biol. Med.*, vol. 4, no. 1, pp. 49-56, 2008.
- [100] S. Dash, P. N. Murthy, L. Nath, and P. Chowdhury, "Kinetic modeling on drug release from controlled drug delivery systems," *Acta Poloniae Pharmaceutica - Drug Research*, vol. 67, no. 3, pp. 217-223, 2010.
- [101] J. Siepmann and F. Siepmann, "Mathematical modeling of drug delivery," *International Journal of Pharmaceutics*, vol. 64, no. 2, pp. 328-343, 2008.
- [102] P. Costa and J. M. Sousa Lobo, "Modeling and comparison of dissolution profiles," *European Journal of Pharmaceutical Sciences*, vol. 13, no. 2, pp. 123-133, 2001.
- [103] G. Pamunuwa, V. Karunaratne, and D. N. Karunaratne, "Effect of lipid composition on in vitro release and skin deposition of curcumin encapsulated liposomes," *J. Nanomater.*, vol. 2016, no. 9, pp. 1-9, 2016.
- [104] A. Wadi, M. Abdel-Hafez, G. A. Hussein, and V. Paul, "Multi-Model Investigation and Adaptive Estimation of the Acoustic Release of a Model Drug from Liposomes," *IEEE Trans. Nanobioscience*, vol. 19, no. 1, pp. 68-77, 2020.
- [105] A. Wadi, M. Abdel-Hafez, and G. A. Hussein, "Modeling and bias-robust estimation of the acoustic release of chemotherapeutics from liposomes," *J. Biomed. Nanotechnol.*, vol. 15, no. 1, pp. 162-169, 2019.
- [106] M. Abdel-Hafez and G. A. Hussein, "Predicting the release of chemotherapeutics from the core of polymeric micelles using ultrasound," *IEEE Trans. Nanobioscience*, vol. 14, no. 4, pp. 378-384, 2015.
- [107] G. A. Hussein, L. Kherbeck, W. G. Pitt, J. A. Hubbell, D. A. Christensen, and D. Velluto, "Kinetics of ultrasonic drug delivery from targeted micelles," *J. Nanosci. Nanotechnol.*, vol. 15, pp. 2099-2104, 2015.
- [108] M. A. Díaz De La Rosa, G. A. Hussein, and W. G. Pitt, "Mathematical modeling of microbubble cavitation at 70 kHz and the importance of the subharmonic in drug delivery from micelles," *Ultrasonics*, vol. 53, no. 1, pp. 97-110, 2013.
- [109] G. A. Hussein *et al.*, "Kinetics of acoustic release of doxorubicin from stabilized and unstabilized micelles and the effect of temperature," *J. Franklin Inst.*, vol. 348, no. 1, pp. 125-133, 2011.
- [110] H. G. Moussa, G. A. Hussein, N. Abel-Jabbar, and S. E. Ahmad, "Use of Model Predictive Control and Artificial Neural Networks to Optimize the Ultrasonic Release of a Model Drug from Liposomes," *IEEE Trans. Nanobioscience*, vol. 16, no. 3, pp. 149-156, 2017.
- [111] "Acoustic impedance, intensity and power," *University of New South Wales*. [Online]. Available: <https://www.animations.physics.unsw.edu.au/jw/sound-impedance-intensity.htm>. [Accessed: 19-Feb-2020].
- [112] "Guidelines for the safe use of diagnostic ultrasound equipment," *The British*

*Medical Ultrasound Society.*, 2009. [Online]. Available:  
<https://www.bmus.org/static/uploads/resources/BMUS-Safety-Guidelines-2009-revision-FINAL-Nov-2009.pdf>. [Accessed: 19-Feb-2020].

## Appendix

### Appendix A: Release modeling plots for control liposomes (Batch 1) at a power density of 7.46 mW/cm<sup>2</sup>

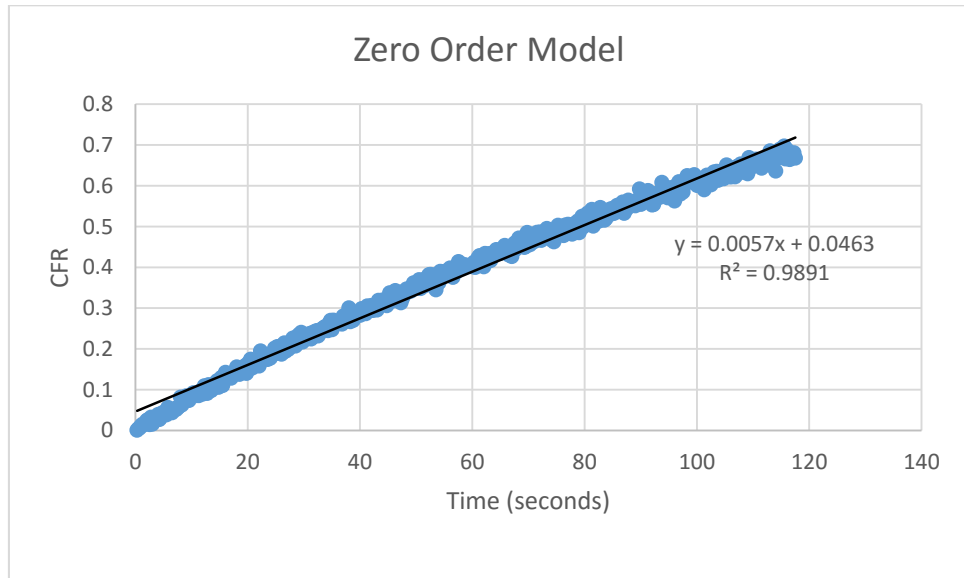


Figure 40: Zero-order model for control liposomes at 7.46 mW/cm<sup>2</sup>

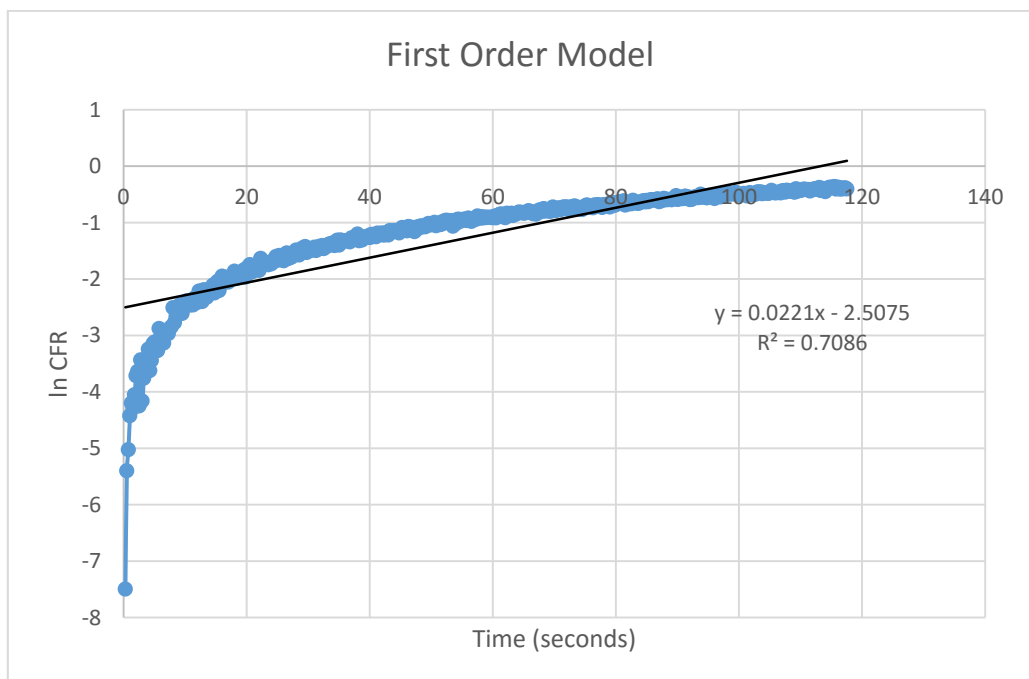


Figure 41: First-order model for control liposomes at 7.46 mW/cm<sup>2</sup>

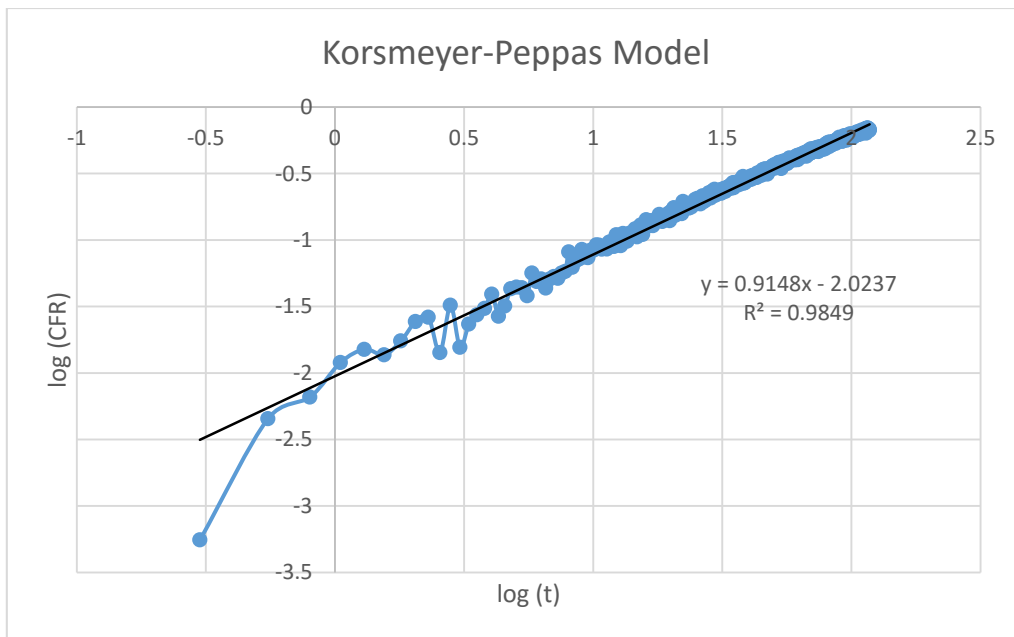


Figure 42: Korsmeyer- Peppas model for control liposomes at 7.46 mW/cm<sup>2</sup>

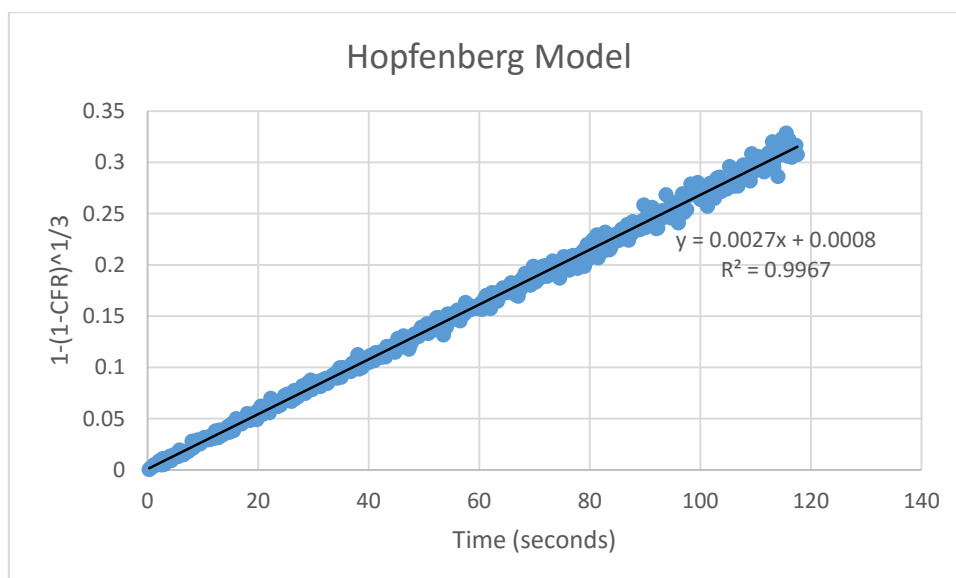


Figure 43: Hopfenberg model for control liposomes at 7.46 mW/cm<sup>2</sup>

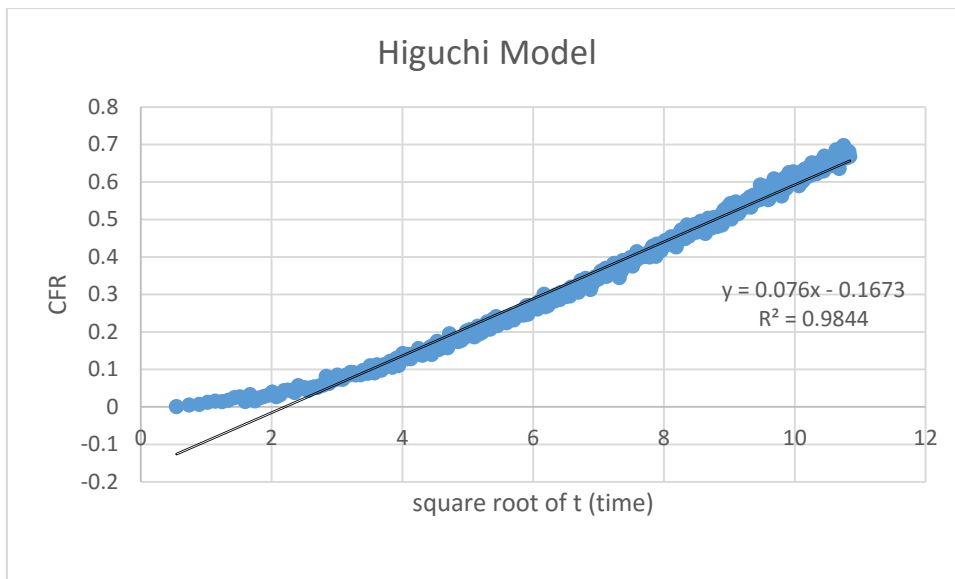


Figure 44: Higuchi model for control liposomes at 7.46 mW/cm<sup>2</sup>

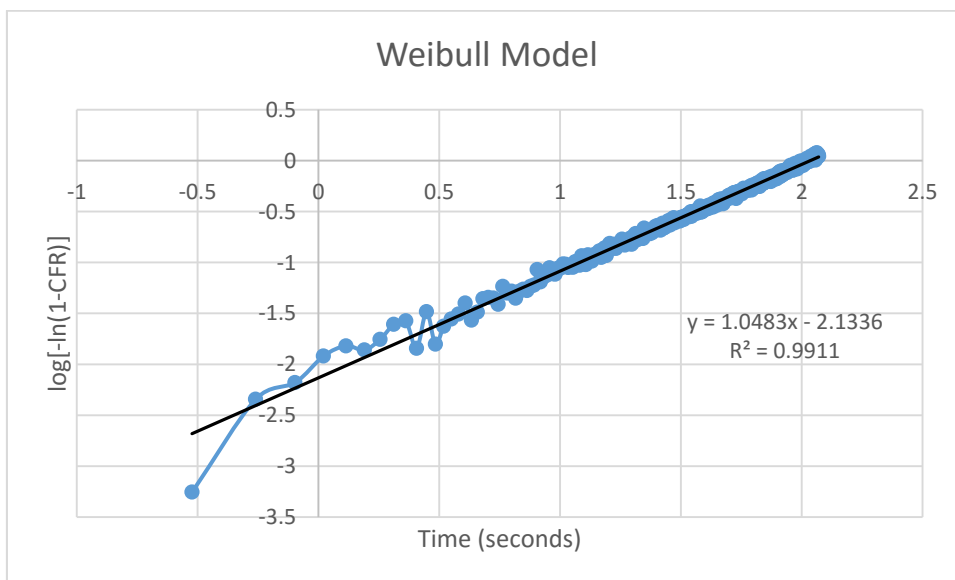


Figure 45: Weibull model for control liposomes at 7.46 mW/cm<sup>2</sup>



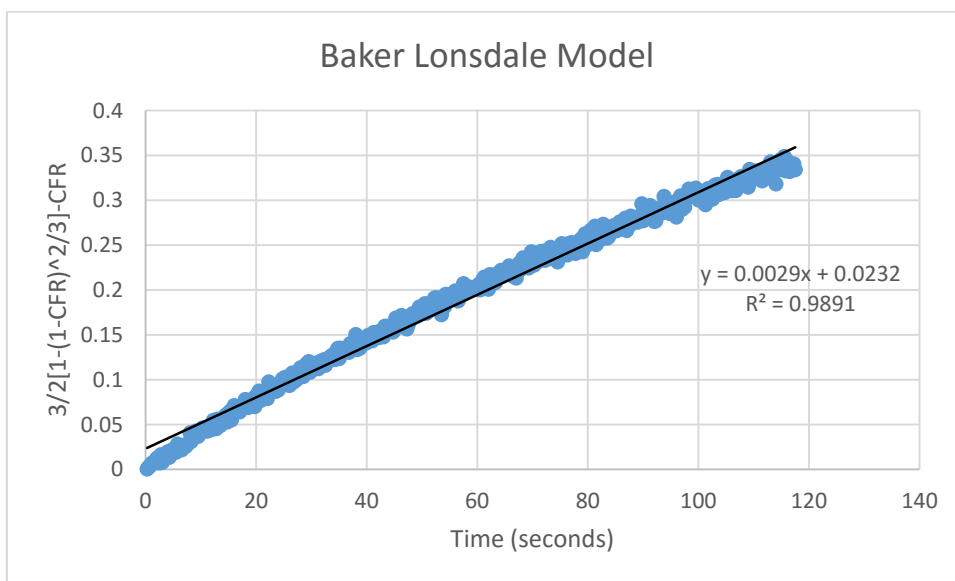


Figure 46: Baker Lonsdale model for control liposomes at 7.46 mW/cm<sup>2</sup>

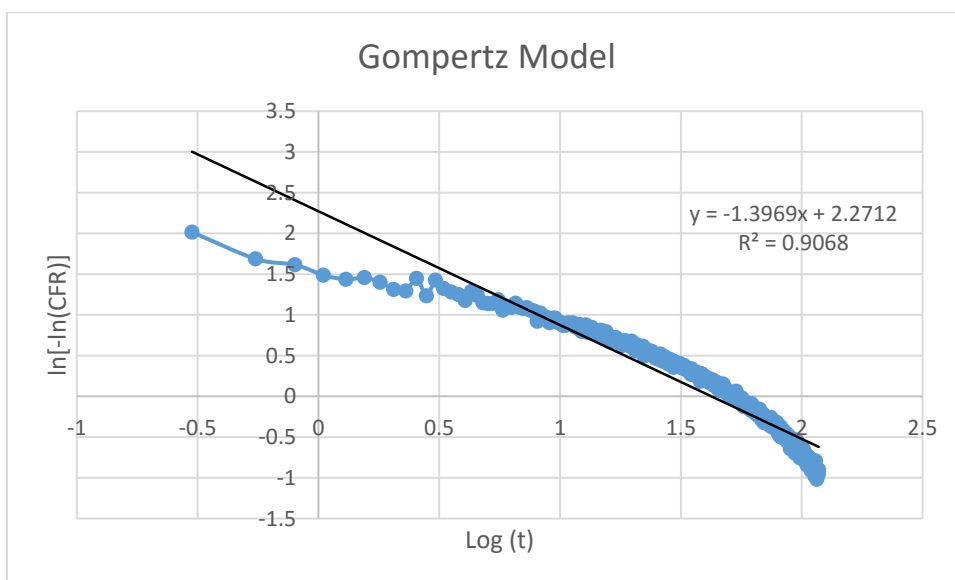


Figure 47: Gompertz model for control liposomes at 7.46 mW/cm<sup>2</sup>

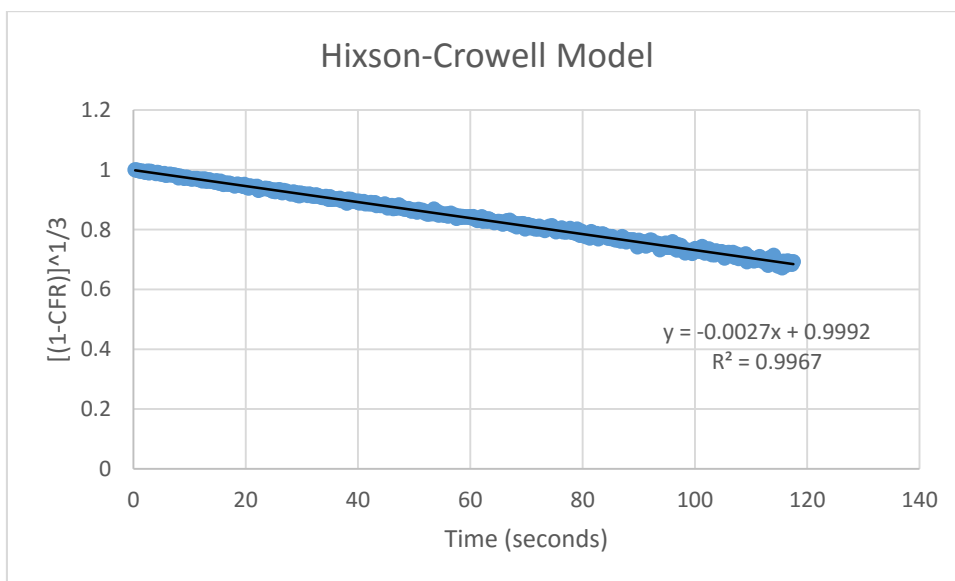


Figure 48: Hixson-Crowell model for control liposomes at  $7.46 \text{ mW/cm}^2$

**Appendix B: Release modeling plots for control liposomes (Batch 1) at a power density of 9.85 mW/cm<sup>2</sup>**



Figure 49: Zero order model for control liposomes at 9.85 mW/cm<sup>2</sup>

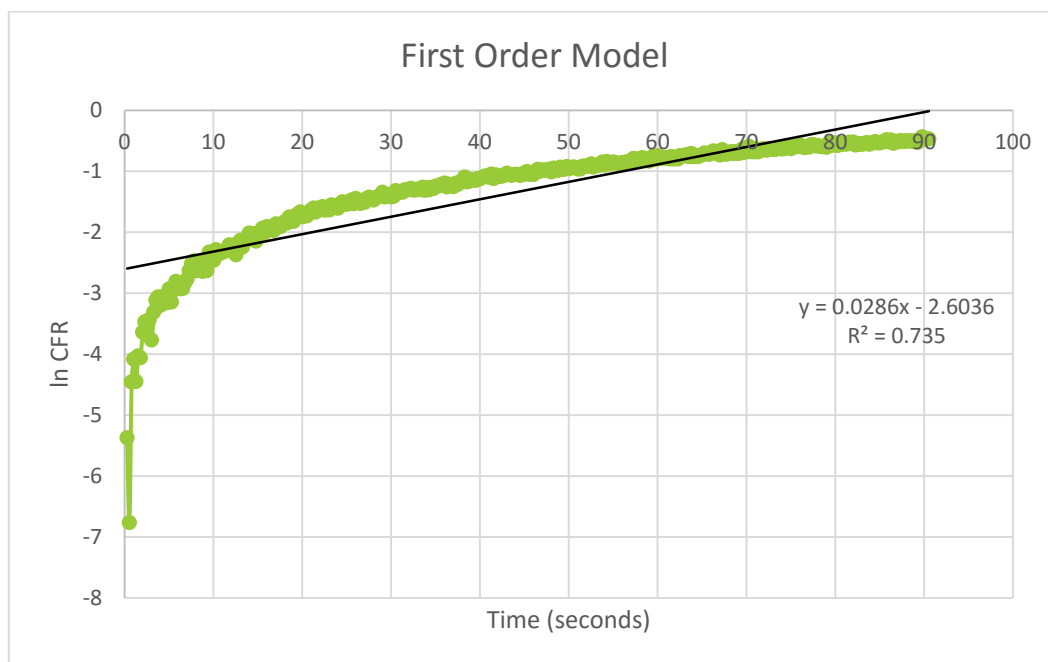


Figure 50: First order model for control liposomes at 9.85 mW/cm<sup>2</sup>

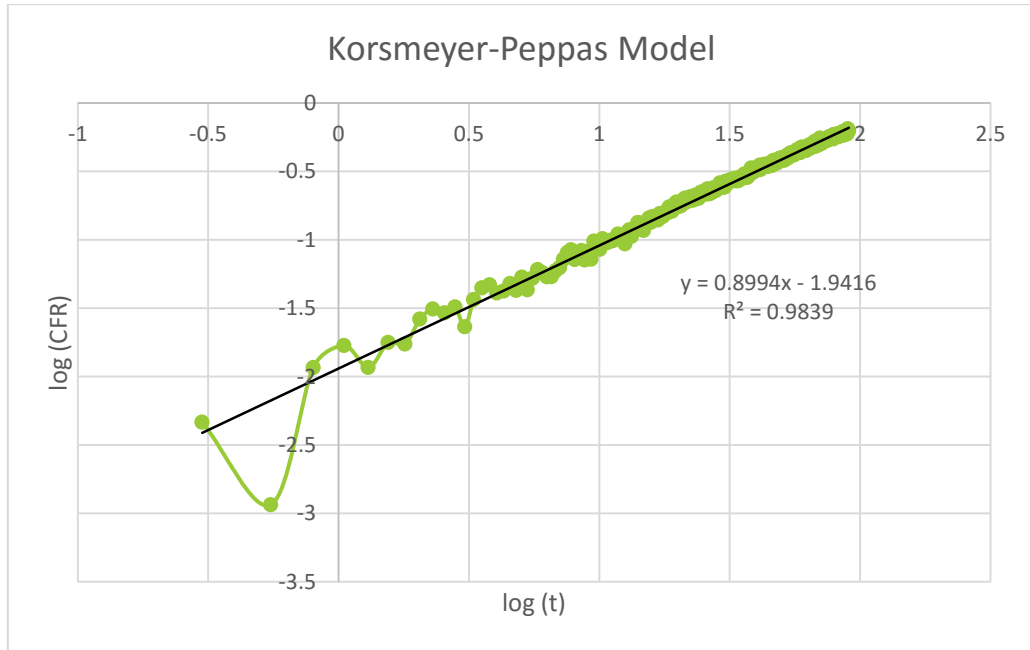


Figure 51: Korsmeyer Peppas model for control liposomes at 9.85 mW/cm<sup>2</sup>

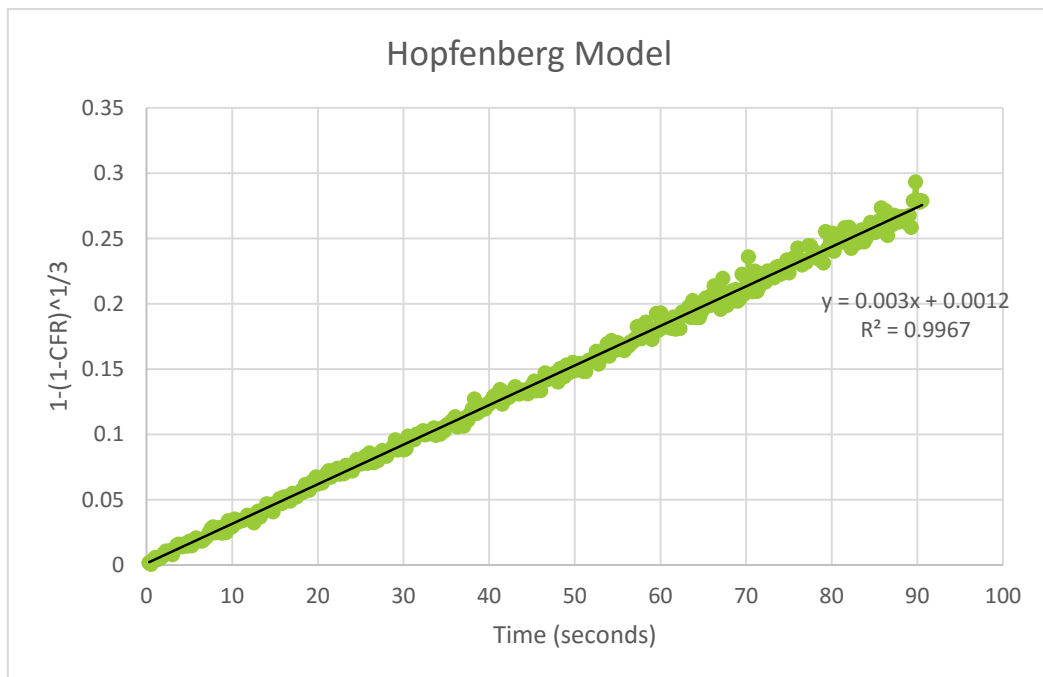


Figure 52: Hopfenberg model for control liposomes at 9.85 mW/cm<sup>2</sup>

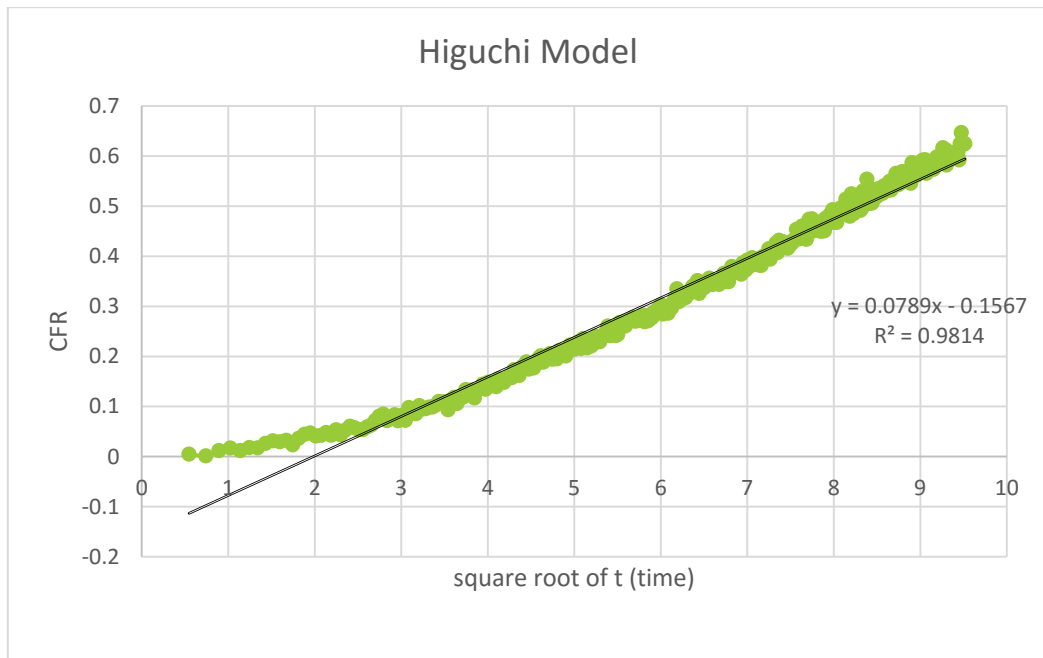


Figure 53: Higuchi model for control liposomes at 9.85 mW/cm<sup>2</sup>

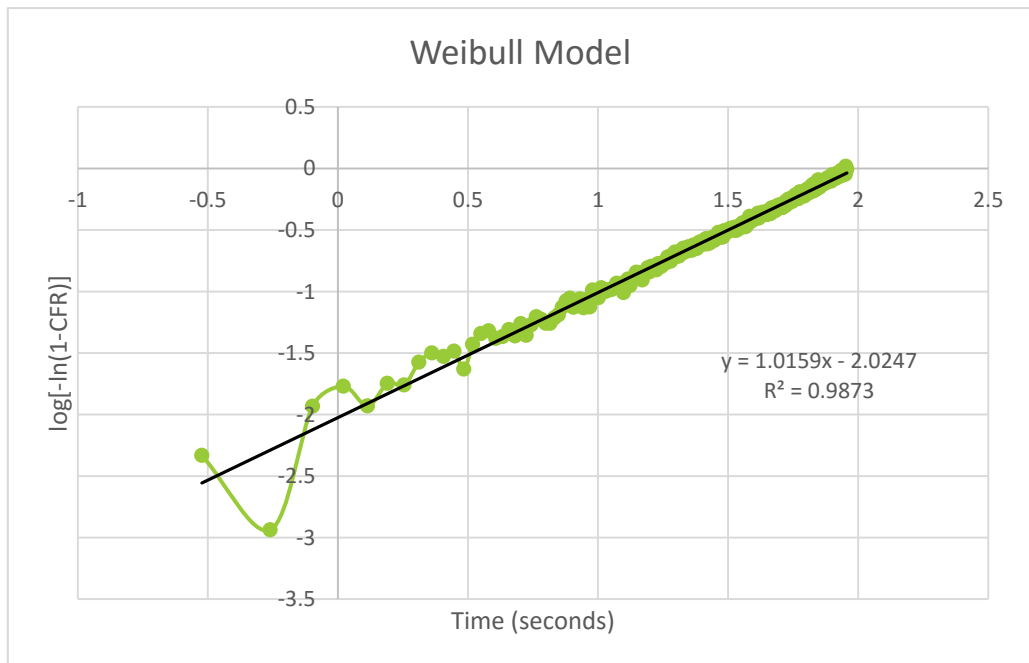


Figure 54: Weinull model for control liposomes at 9.85 mW/cm<sup>2</sup>

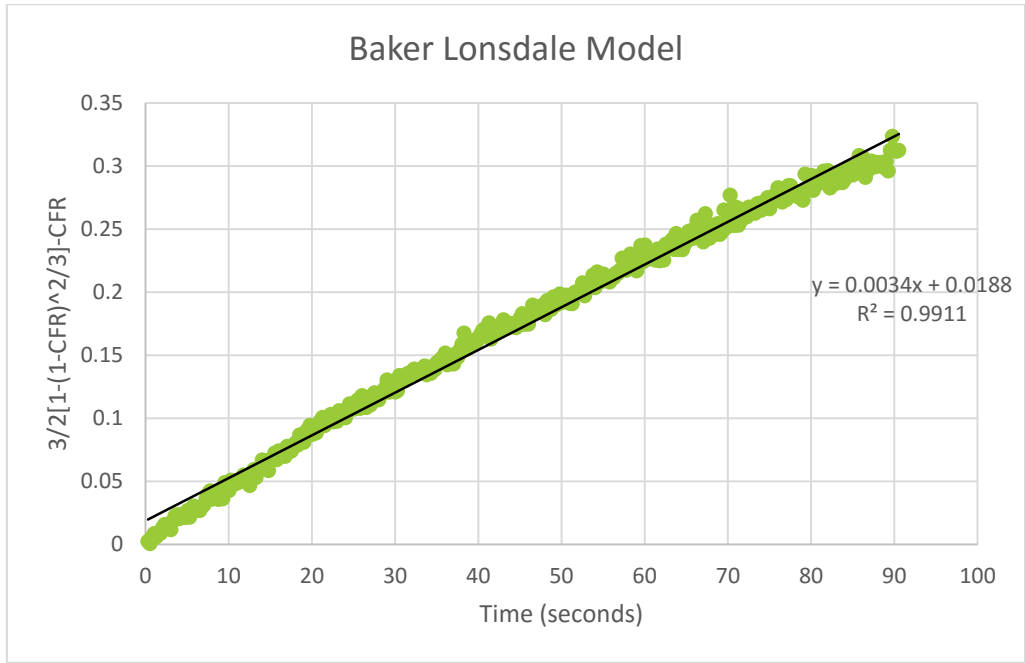


Figure 55: Baker Lonsdale model for control liposomes at 9.85 mW/cm<sup>2</sup>

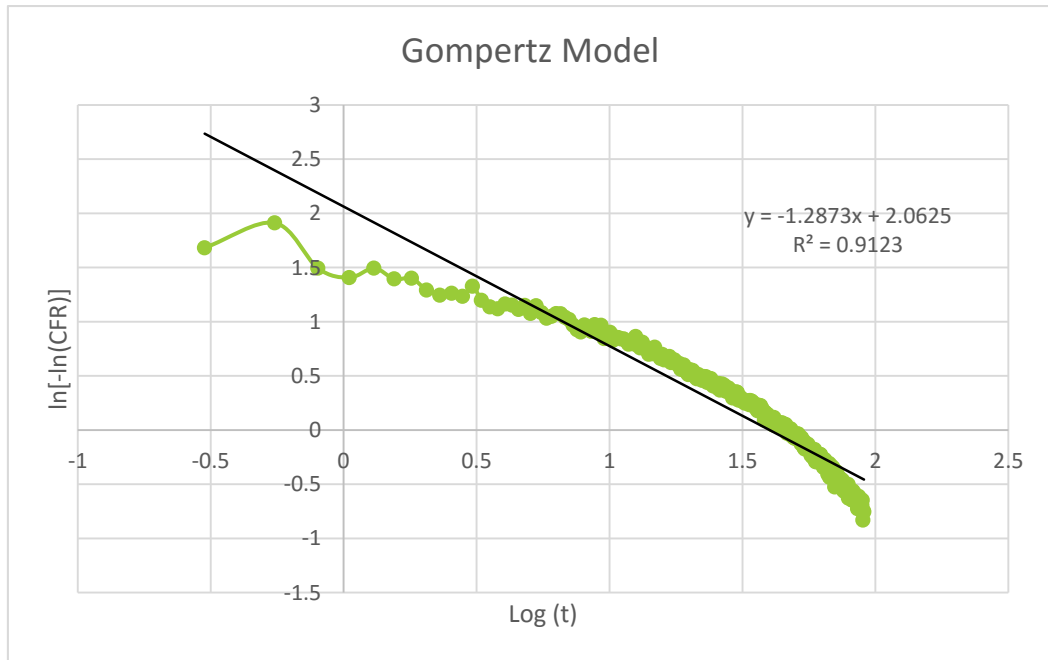


Figure 56: Gompertz model for control liposomes at 9.85 mW/cm<sup>2</sup>



Figure 57: Hixson - Crowell model for control liposomes at 9.85 mW/cm<sup>2</sup>

**Appendix C: Release modeling plots for control liposomes (Batch 1) at a power density of 17.31 mW/cm<sup>2</sup>**

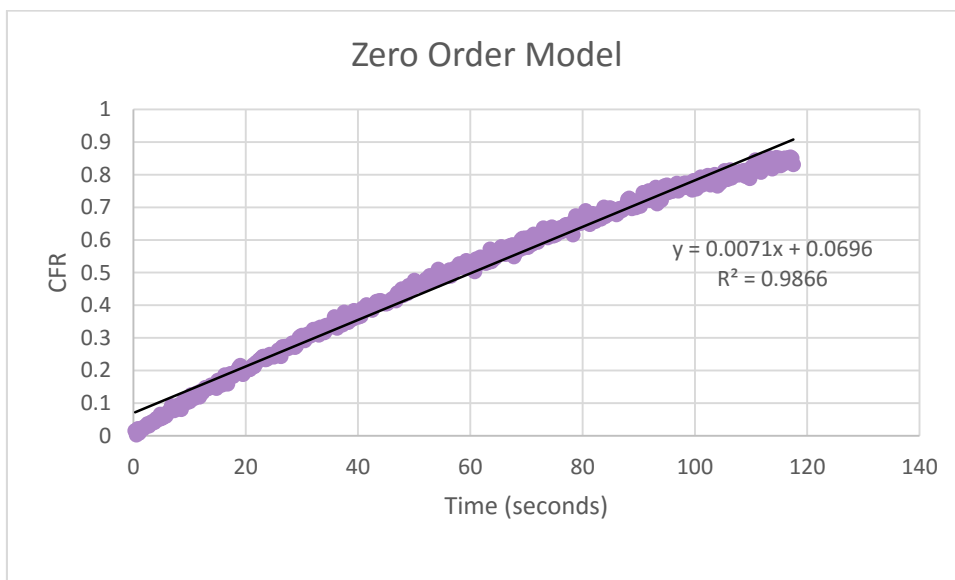


Figure 58: Zero - order model for control liposomes at 17.31 mW/cm<sup>2</sup>

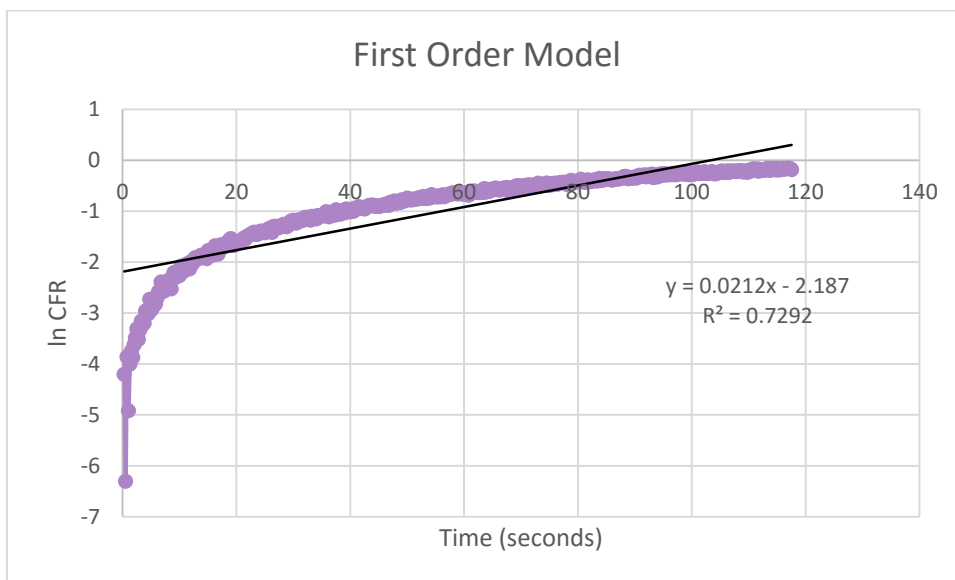


Figure 59: First order model for control liposomes at 17.31 mW/cm<sup>2</sup>



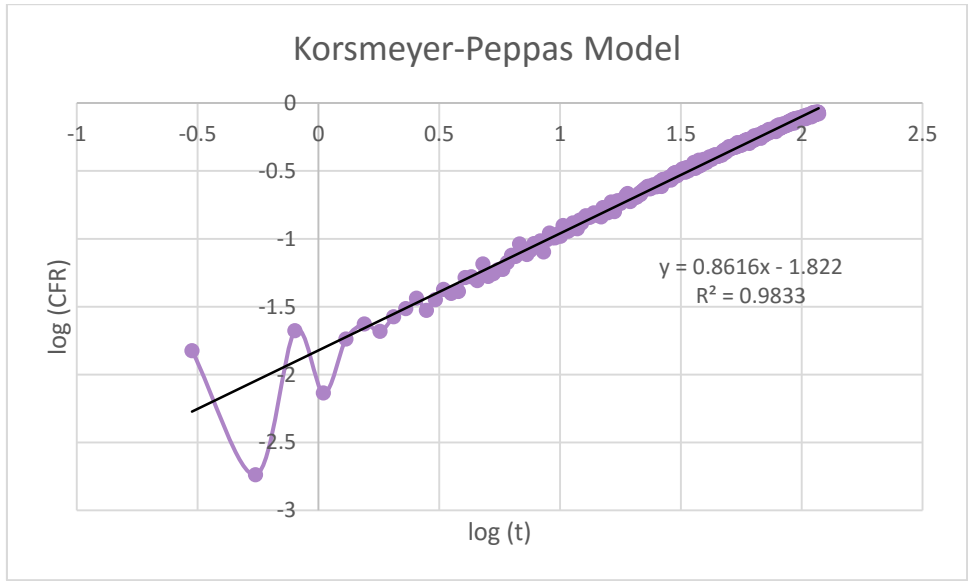


Figure 60: Korsmeyer - Peppas model for control liposomes at 17.31 mW/cm<sup>2</sup>

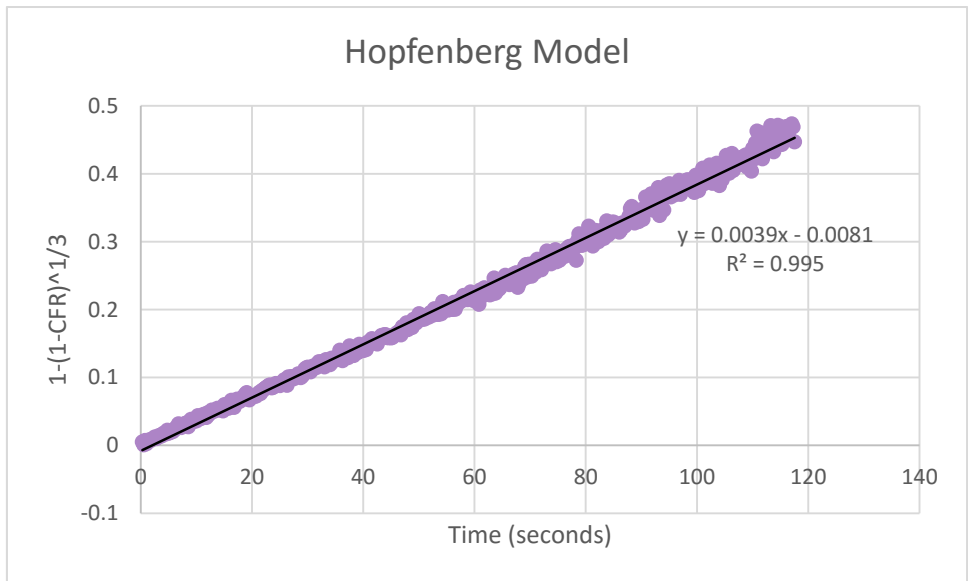


Figure 61: Hopfenberg model for control liposomes at 17.31 mW/cm<sup>2</sup>

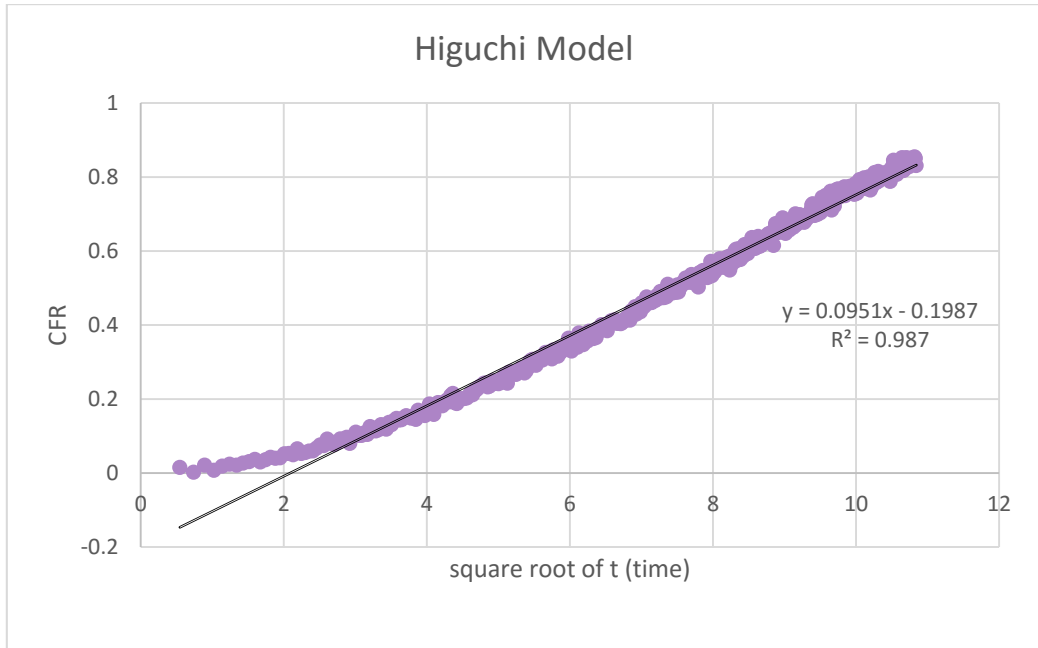


Figure 62: Higuchi model for control liposomes at 17.31 mW/cm<sup>2</sup>

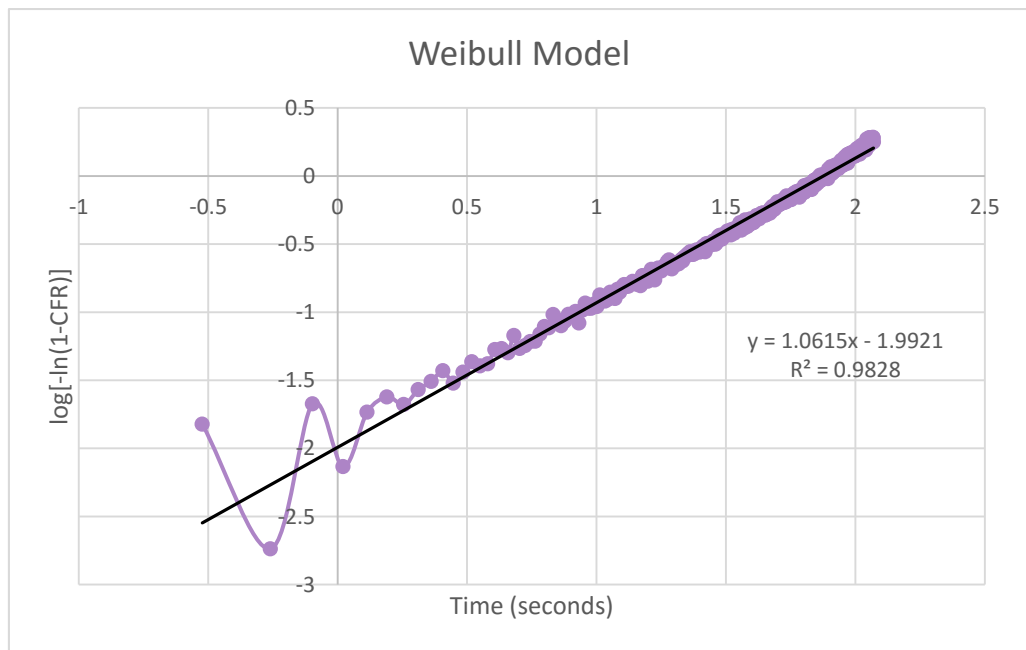


Figure 63: Weibull model for control liposomes at 17.31 mW/cm<sup>2</sup>

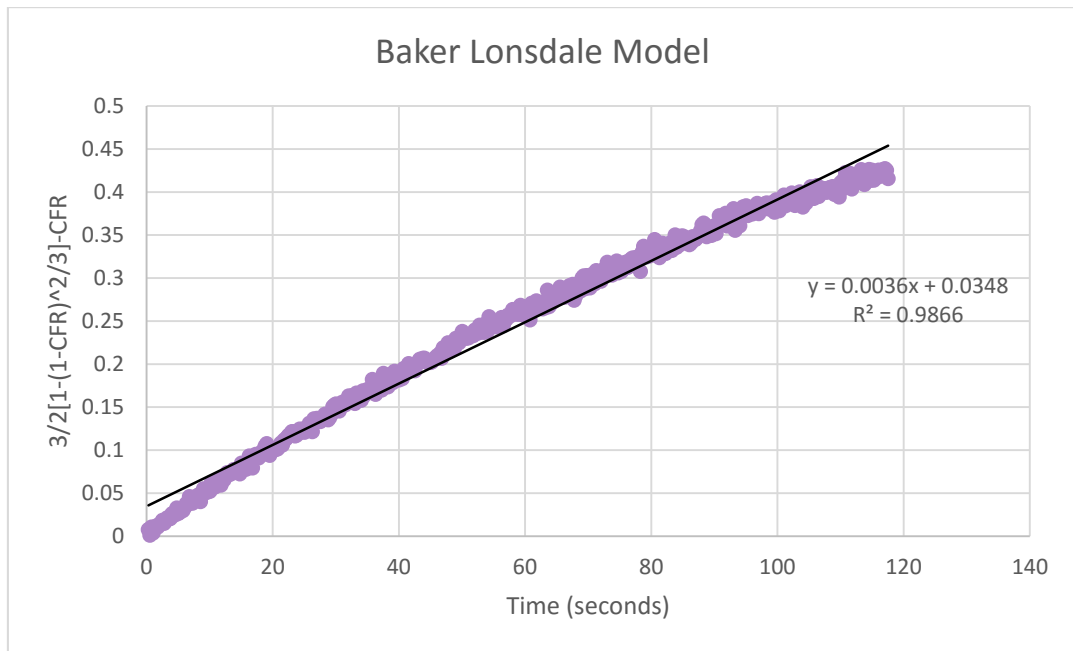


Figure 64: Baker-Lonsdale model for control liposomes at 17.31 mW/cm<sup>2</sup>

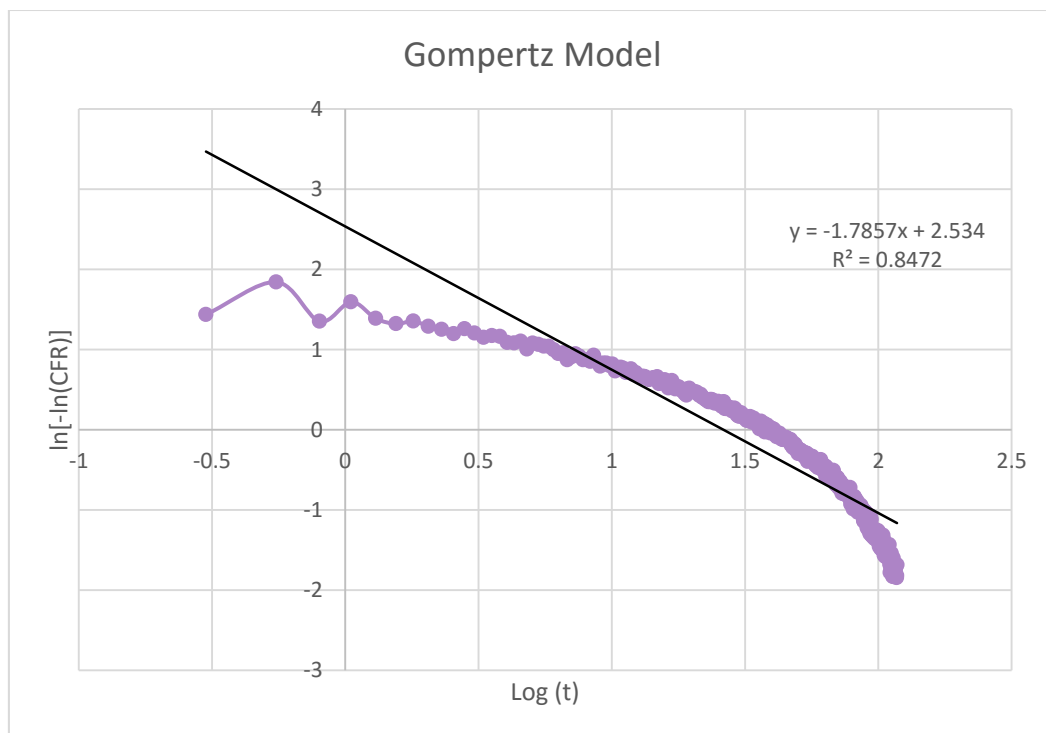


Figure 65: Gompertz model for control liposomes at 17.31 mW/cm<sup>2</sup>

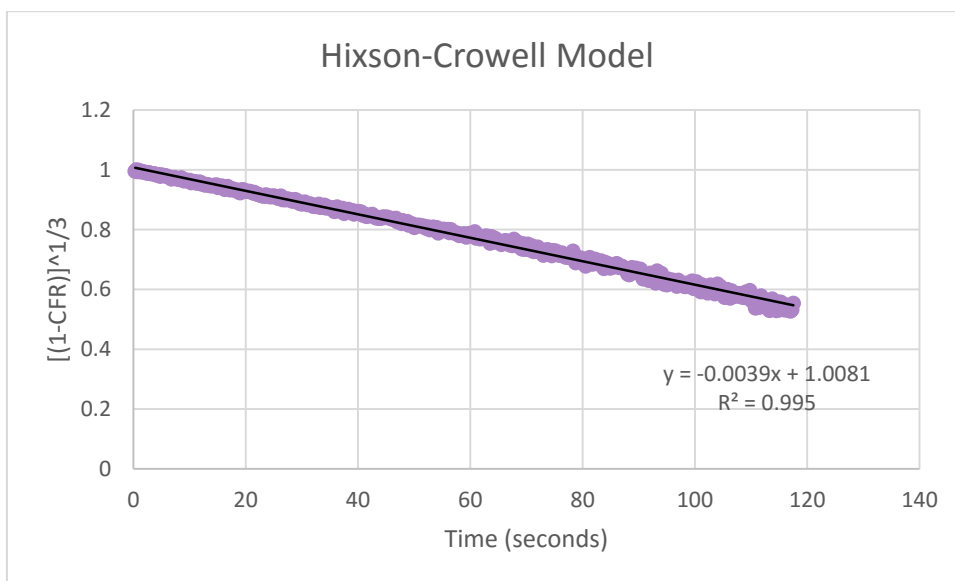


Figure 66: Hixson-Crowell model for control liposomes at 17.31 mW/cm<sup>2</sup>

**Appendix D: Release modeling plots for immunoliposomes (Batch 1) at a power density of 9.85 mW/cm<sup>2</sup>**

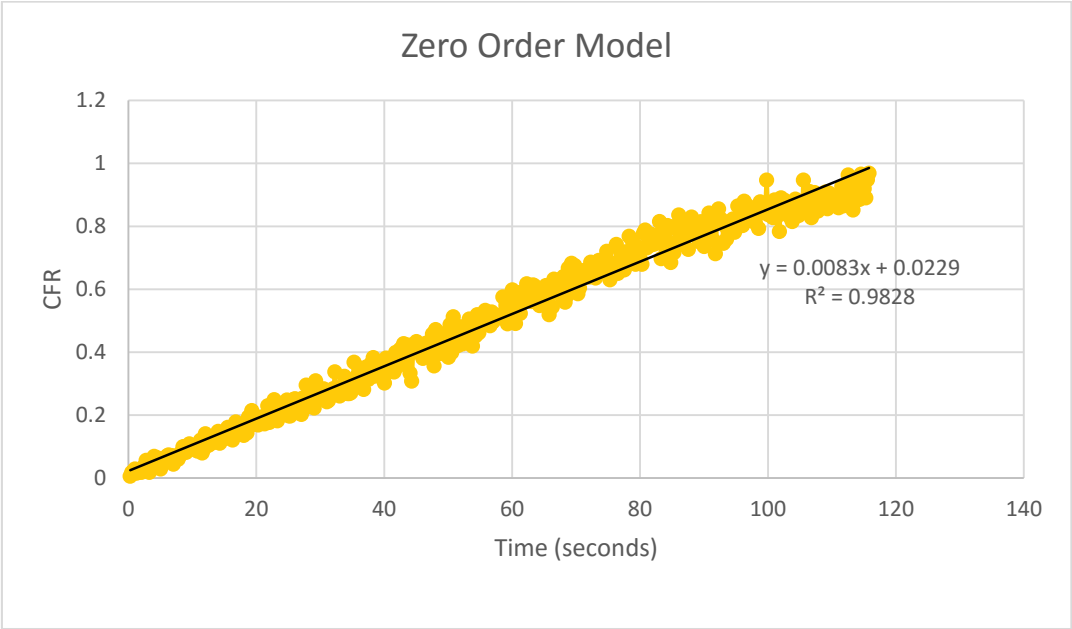


Figure 67: Zero order model for immunoliposomes at 9.85 mW/cm<sup>2</sup>

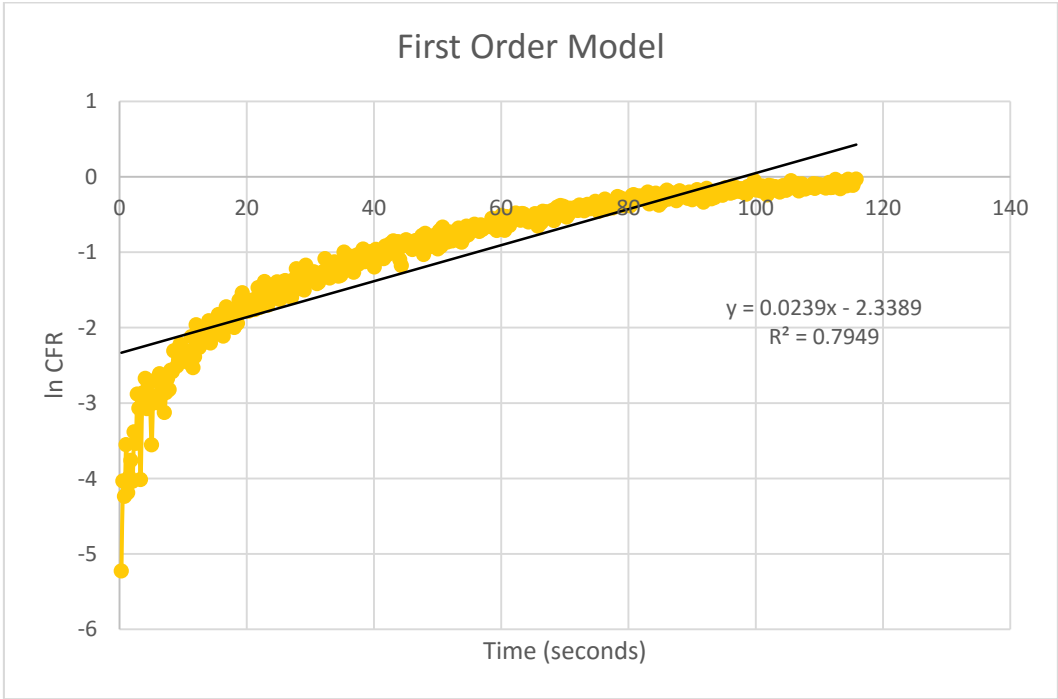


Figure 68: First order model for immunoliposomes at 9.85 mW/cm<sup>2</sup>

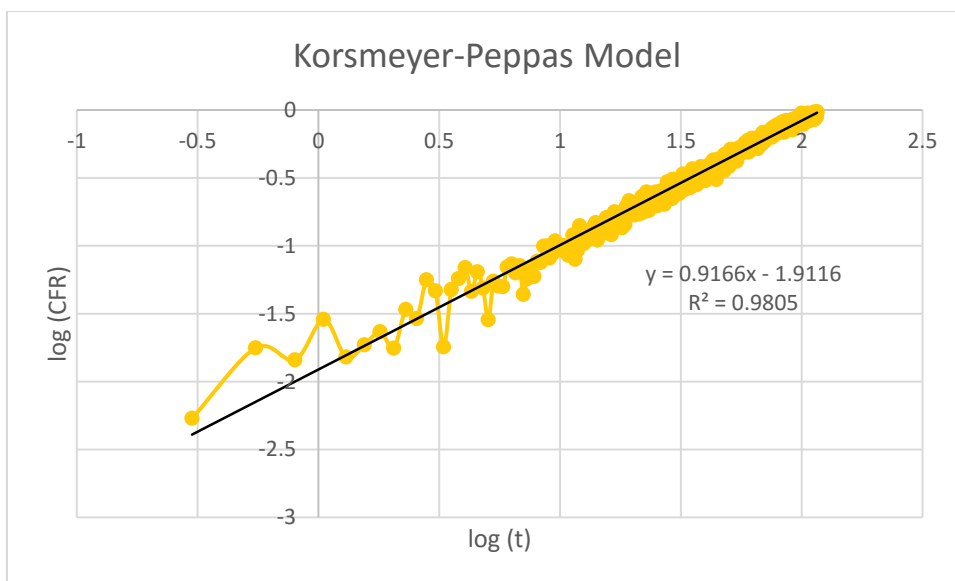


Figure 69: Korsmeyer-Peppas model for immunoliposomes at 9.85 mW/cm<sup>2</sup>

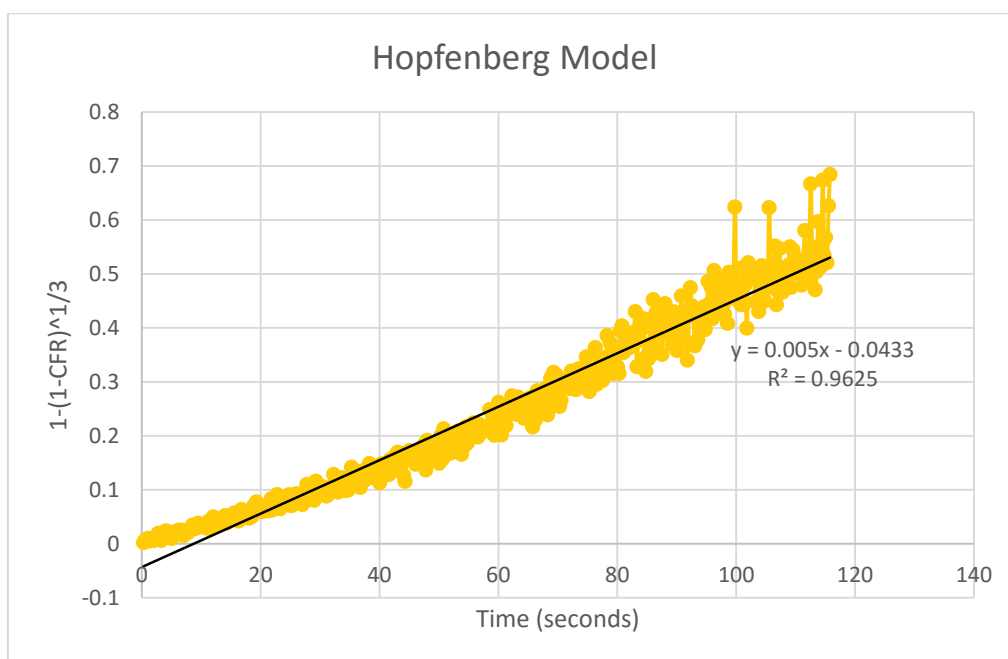


Figure 70: Hopfenberg model for immunoliposomes at 9.85 mW/cm<sup>2</sup>

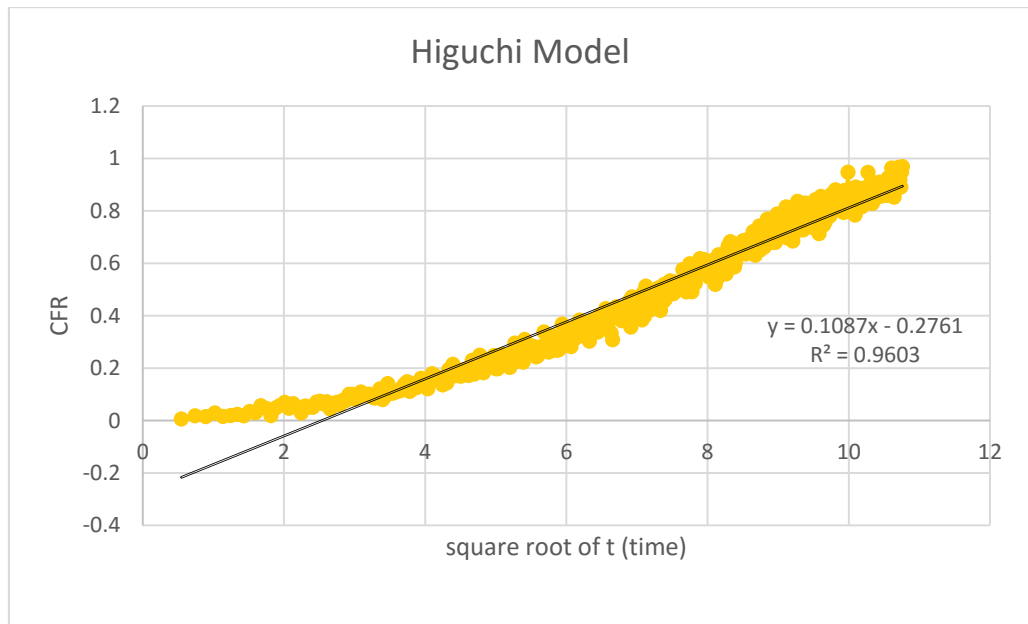


Figure 71: Higuchi model for immunoliposomes at 9.85 mW/cm<sup>2</sup>

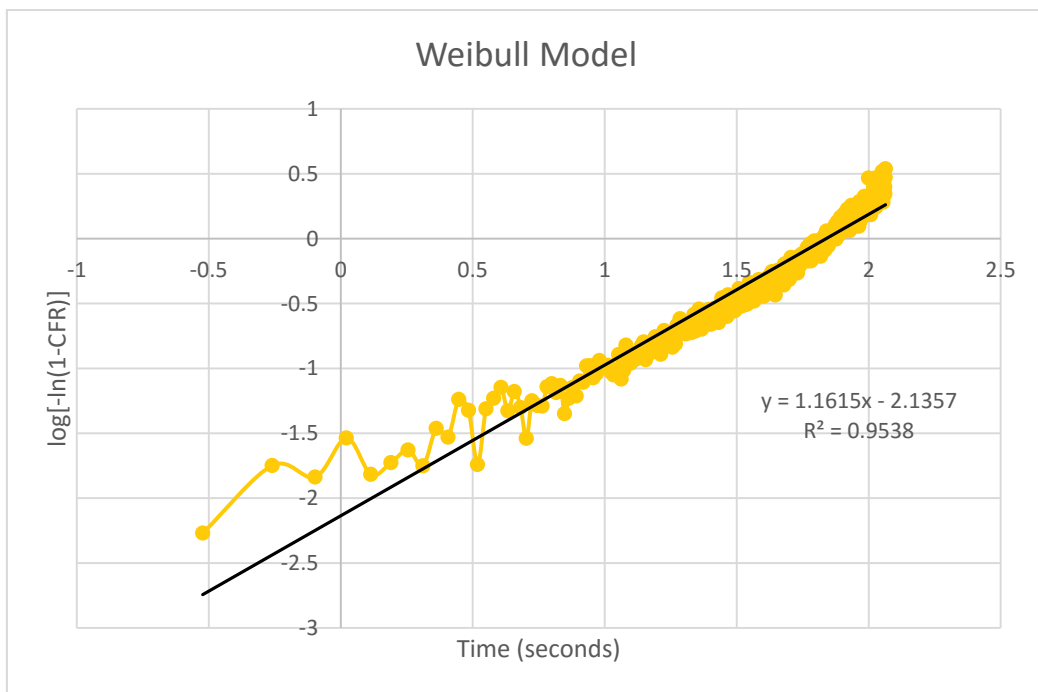


Figure 72: Weibull model for immunoliposomes at 9.85 mW/cm<sup>2</sup>

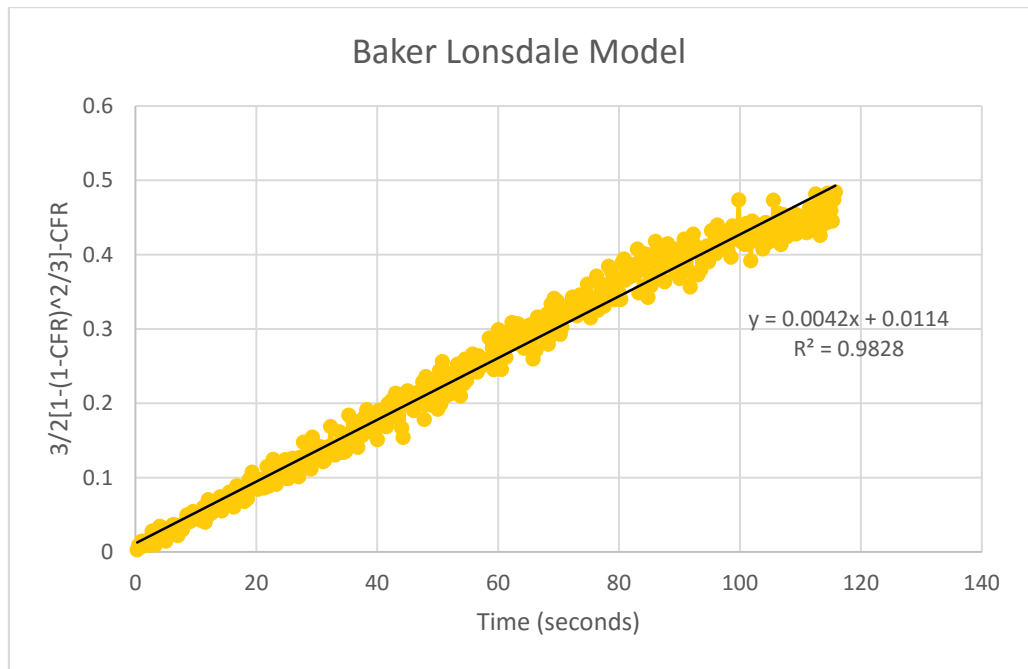


Figure 73: Baker-Lonsdale model for immunoliposomes at 9.85 mW/cm<sup>2</sup>

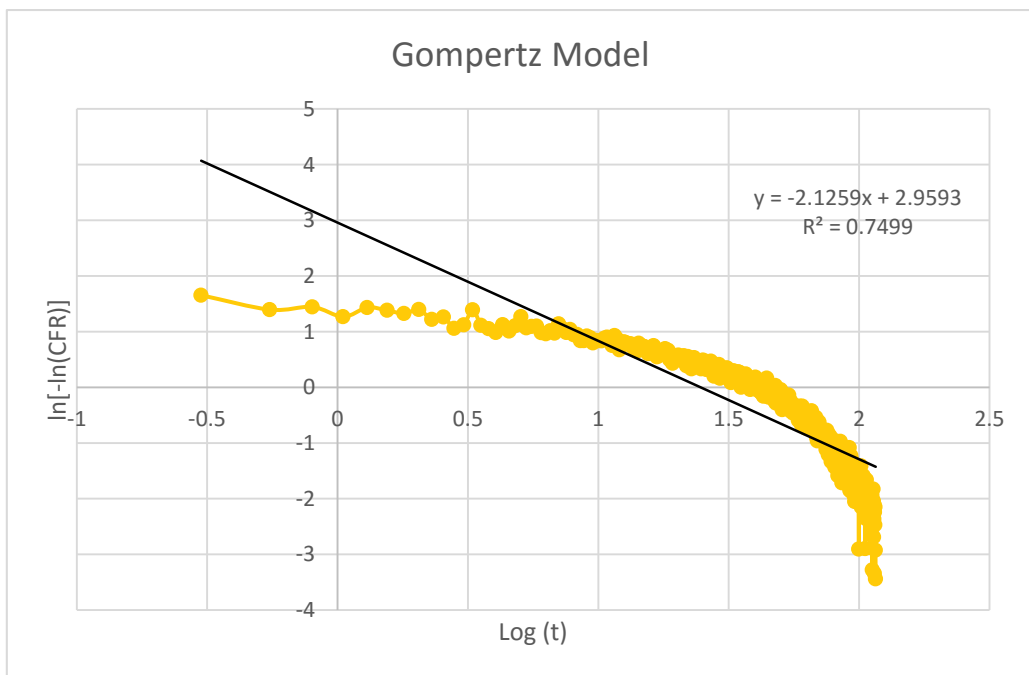


Figure 74: Gompertz model for immunoliposomes at 9.85 mW/cm<sup>2</sup>



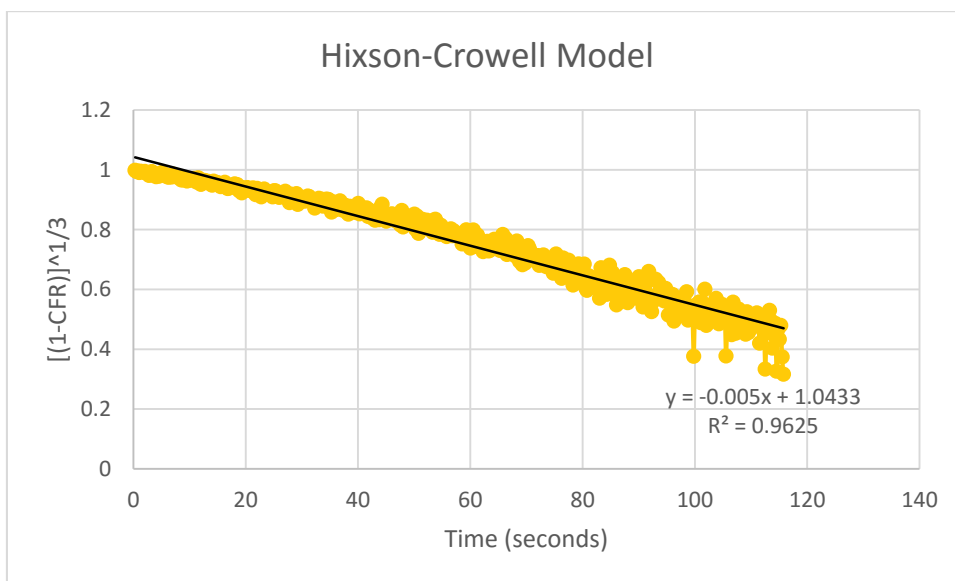


Figure 75: Hixson-Crowell model for immunoliposomes at 9.85 mW/cm<sup>2</sup>

**Appendix E: Release modeling plots for immunoliposomes (Batch 1) at a power density of 17.31 mW/cm<sup>2</sup>**

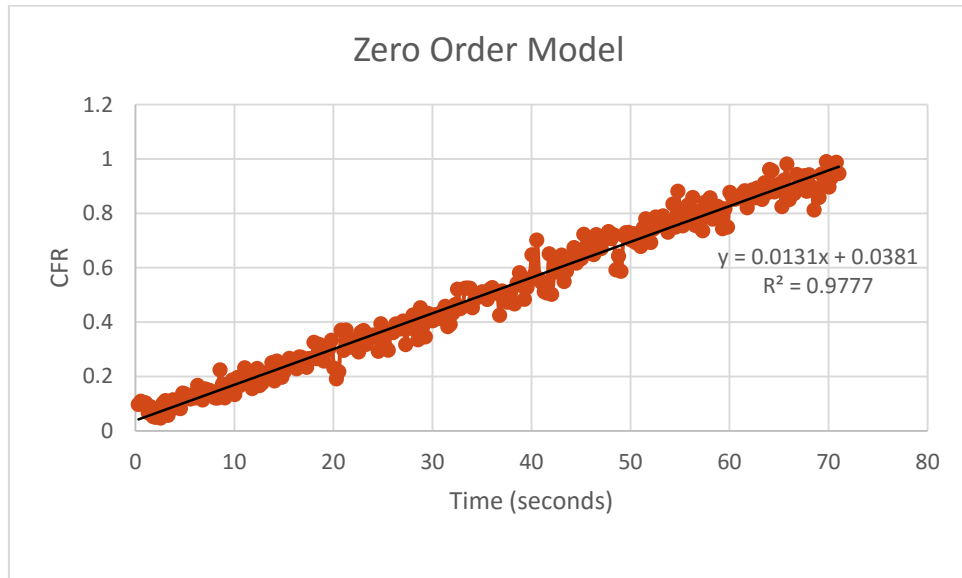


Figure 76: Zero order model for immunoliposomes at 17.31 mW/cm<sup>2</sup>

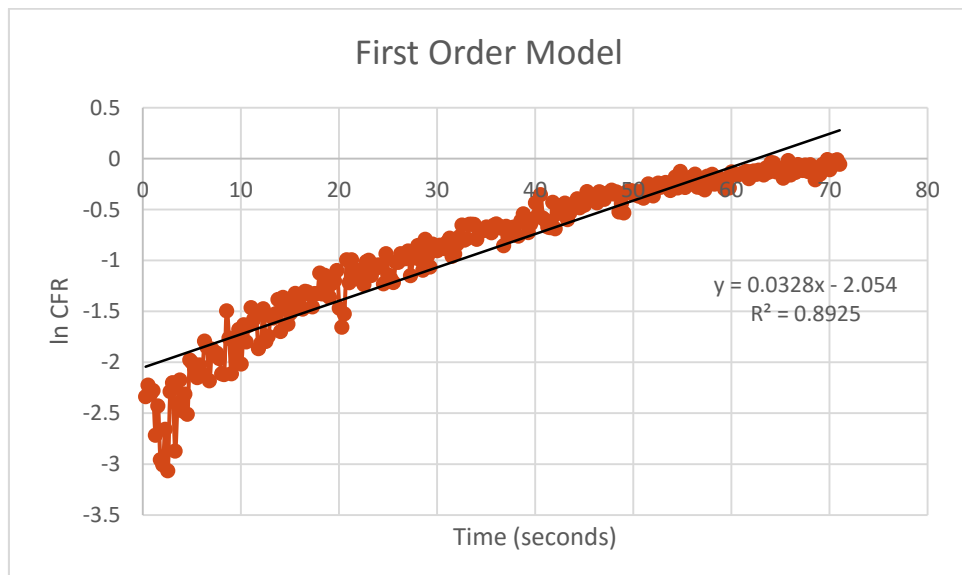


Figure 77: First order model for immunoliposomes at 17.31 mW/cm<sup>2</sup>

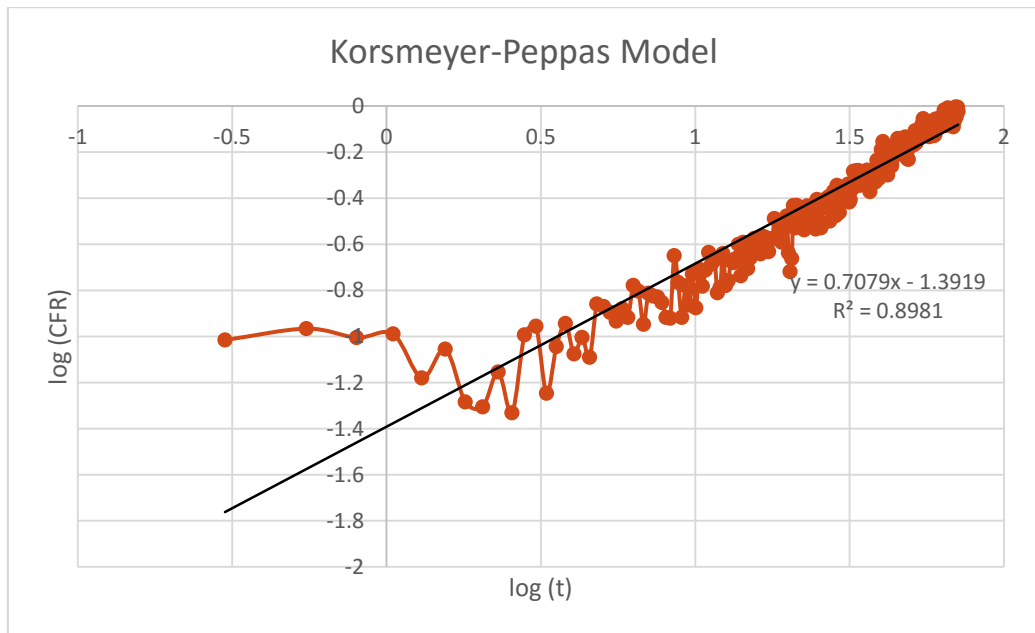


Figure 78: Korsmeyer - Peppas model for immunoliposomes at 17.31 mW/cm<sup>2</sup>

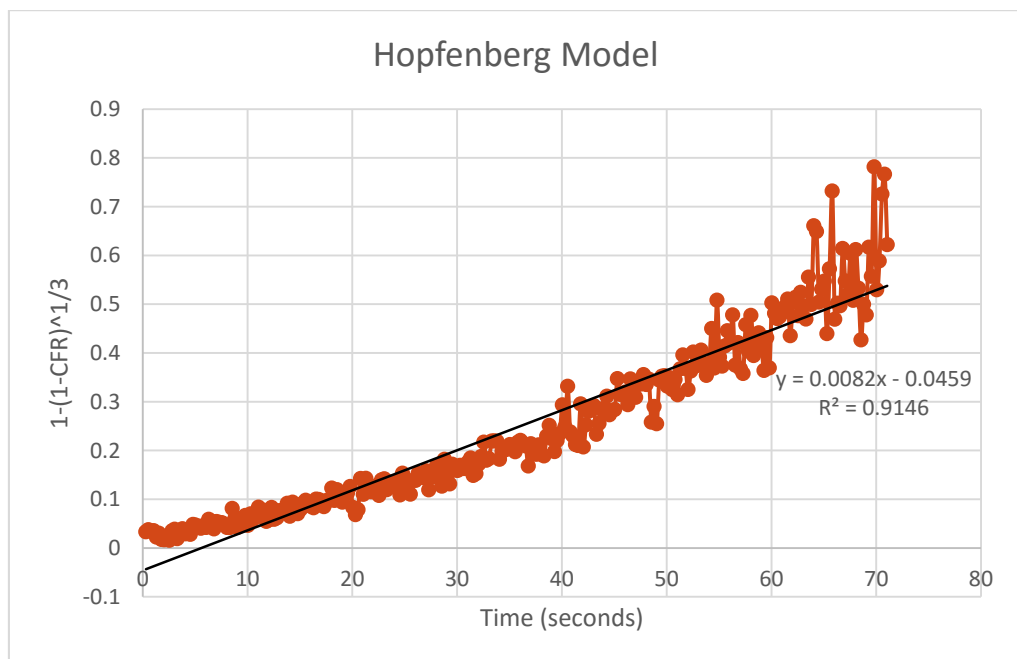


Figure 79: Hopfenberg model for immunoliposomes at 17.31 mW/cm<sup>2</sup>

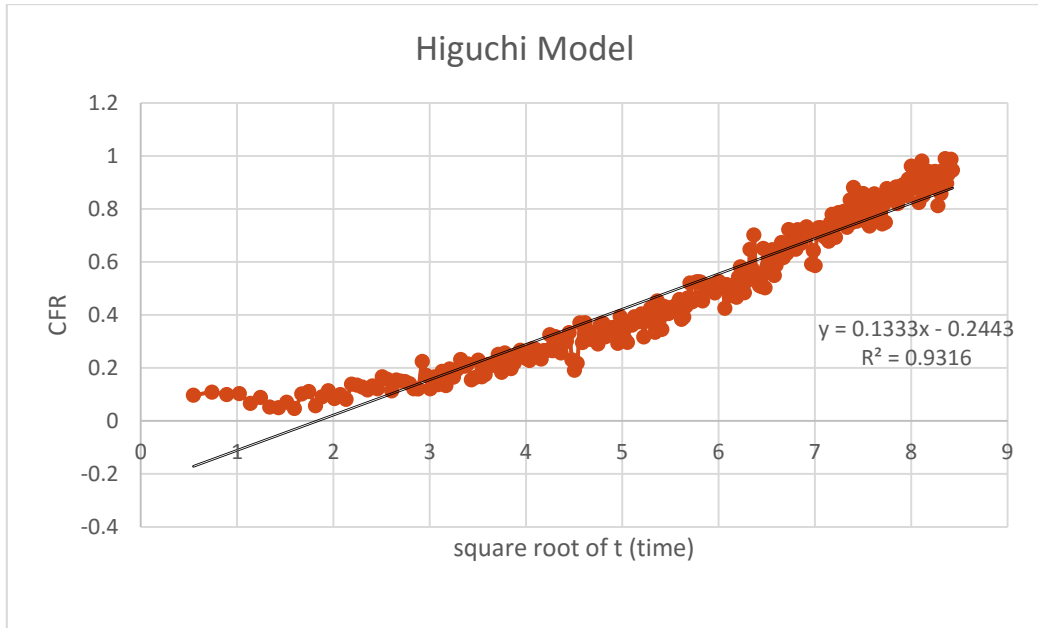


Figure 80: Higuchi model for immunoliposomes at 17.31 mW/cm<sup>2</sup>

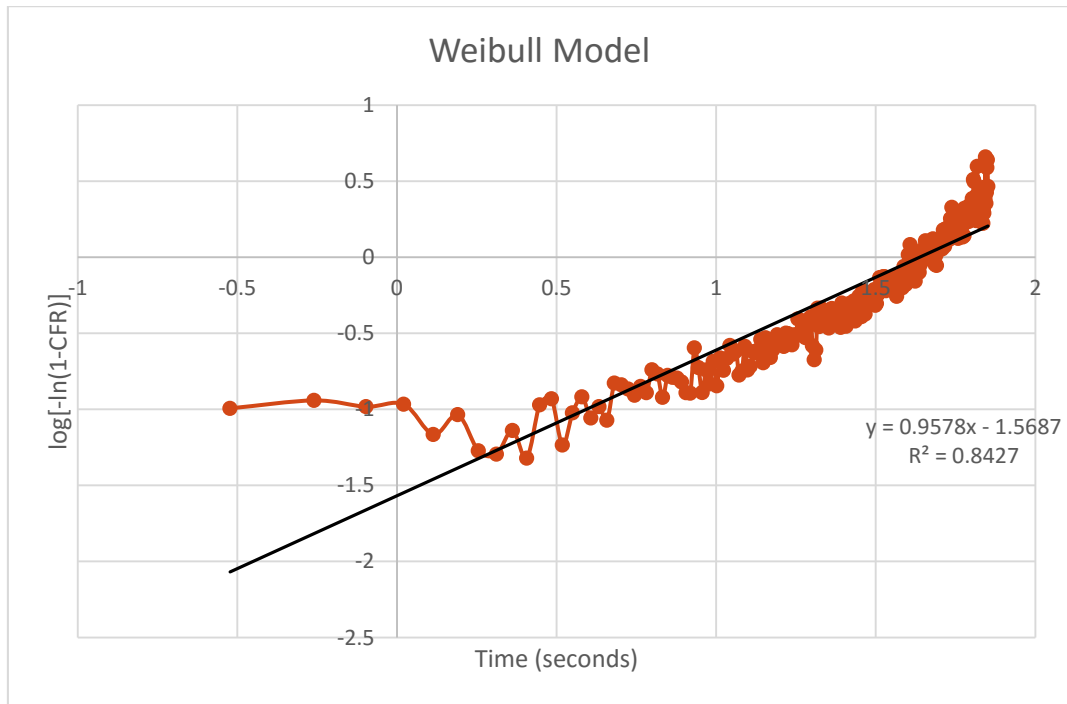


Figure 81: Weibull model for immunoliposomes at 17.31 mW/cm<sup>2</sup>

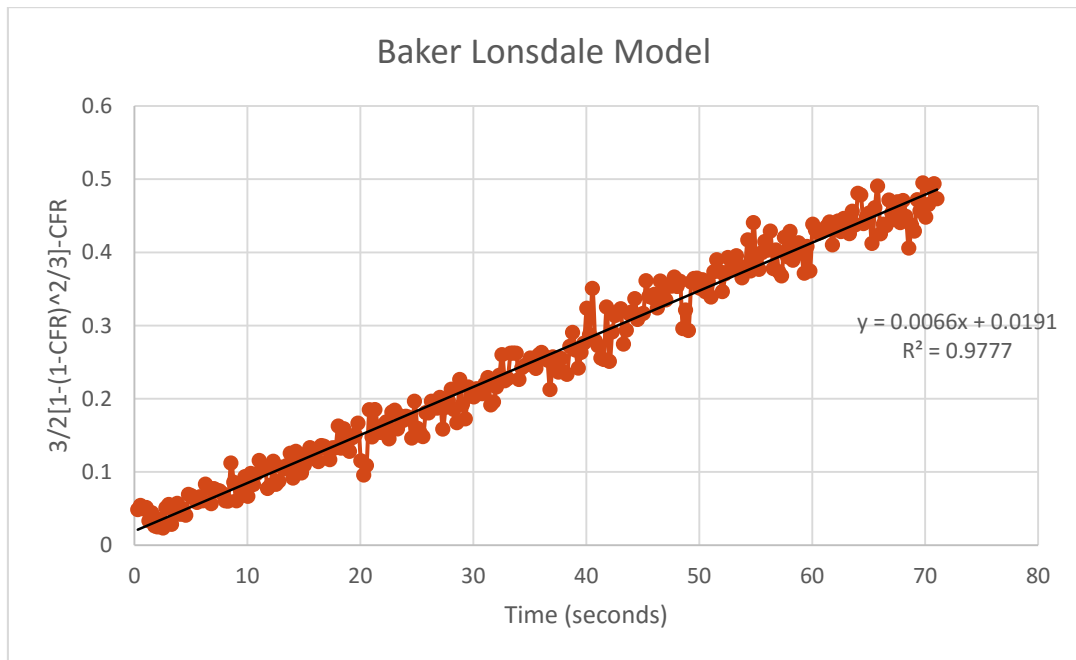


Figure 82: Baker-Lonsdale model for immunoliposomes at 17.31 mW/cm<sup>2</sup>

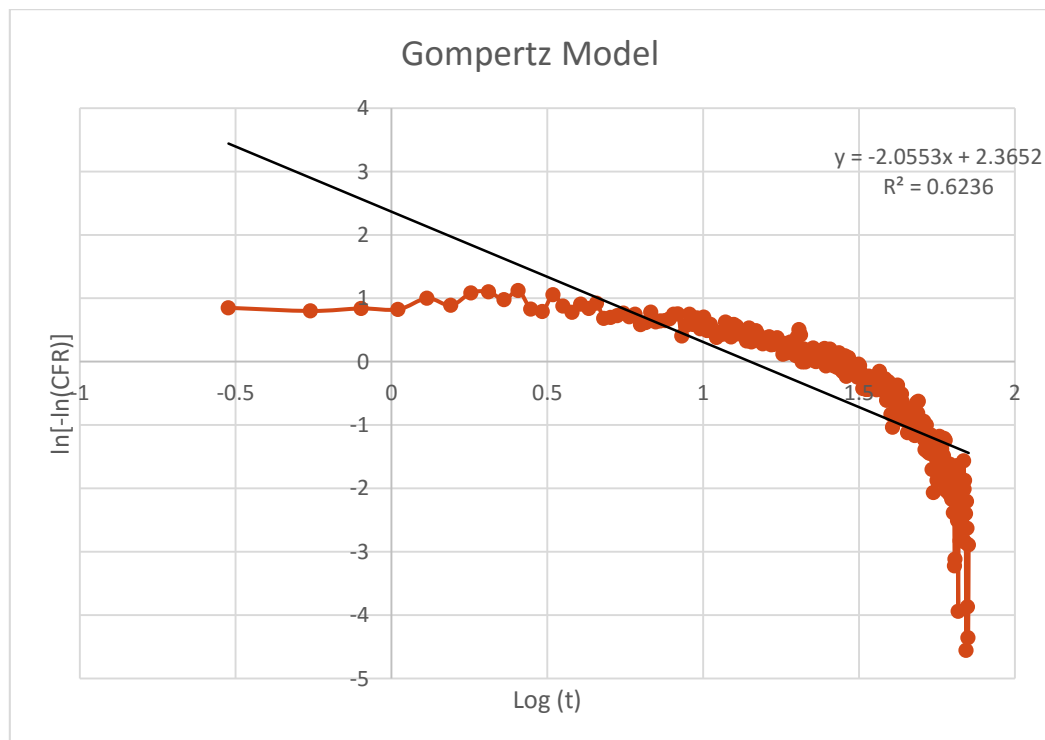


Figure 83: Gompertz model for immunoliposomes at 17.31 mW/cm<sup>2</sup>

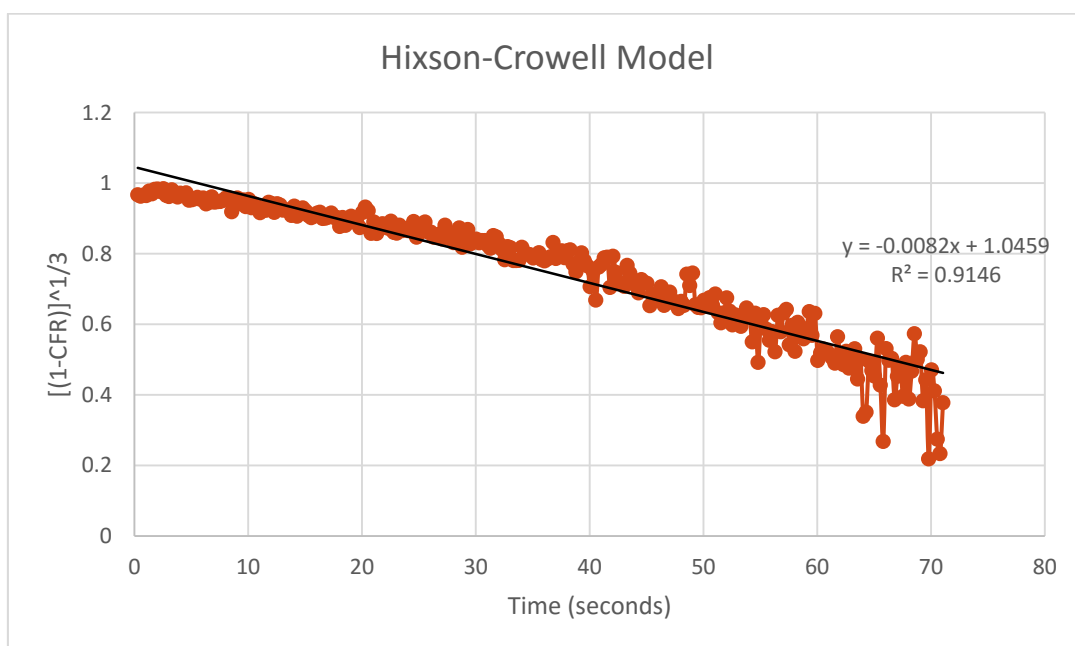


Figure 84: Hixson-Crowell model for immunoliposomes at 17.31 mW/cm<sup>2</sup>

## **Vita**

Saniha Aysha Ajith was born in 1996, in Abu Dhabi, United Arab Emirates. She received her primary and secondary education from St. Joseph's School, Abu Dhabi, UAE and graduated in 2014. She then went on to pursue a Bachelors degree in Chemical Engineering from Abu Dhabi University, UAE, where she graduated with Magna Cum Laude honors in 2018. She worked as a 'Well Services Intern' at Schlumberger, Abu Dhabi, UAE briefly in 2018. Following this, she joined the Masters in Chemical Engineering program at the American University of Sharjah, UAE, in 2018. She received a graduate assistantship which allowed her to work as a Graduate Teaching Assistant in the department from 2018 to 2020. She was also part of the Graduate Students Association committee in 2019. During her masters' education, she was part of the 'Ultrasound in Cancer' research group at the university. Her thesis focuses on targeted drug delivery methods for cancer using ultrasound. Her research interest lies in drug delivery, nanotechnology and biomedical engineering